Quaternary Science Reviews 272 (2021) 107194

Contents lists available at ScienceDirect

Quaternary Science Reviews

journal homepage: www.elsevier.com/locate/quascirev

Geomorphology and ^{10}Be chronology of the Last Glacial Maximum and deglaciation in northeastern Patagonia, 43°S-71°W

Tancrède P.M. Leger [a, *], Andrew S. Hein [a], Robert G. Bingham [a], Ángel Rodés [b], Derek Fabel [b], Rachel K. Smedley [c]

[a] School of GeoSciences, University of Edinburgh, Drummond Street, Edinburgh, EH8 9XP, Scotland, UK
[b] Scottish Universities Environmental Research Centre, Scottish Enterprise Technology Park, East Kilbride, G75 OQF, Glasgow, Scotland, UK
[c] University of Liverpool, Department of Geography and Planning, Chatham Street, Liverpool, L69 7ZT, UK

ARTICLE INFO

Article history:
Received 21 June 2021
Received in revised form
30 August 2021
Accepted 14 September 2021
Available online xxx

Handling Editor: C. O'Cofaigh

Keywords:
South America
Patagonian ice sheet
Quaternary
Last glacial maximum
Marine isotope stage 2
Cosmogenic isotopes
Geomorphology (glacial)
Glaciology
Paleoclimatology
Patagonia

ABSTRACT

In southern South America, well-dated glacial geomorphological records constrain the last glacial cycle across much of the former Patagonian Ice Sheet, but its northeastern sector remains comparatively understudied and unconstrained. This knowledge gap inhibits our understanding of the timing of maximum glacier extent, the duration of the glacial maximum, the onset of deglaciation, and whether asynchronies exist in the behaviour of the former ice sheet with latitude, or with location (east or west) relative to the ice divide. Robust glacial reconstructions from this region are thus required to comprehend the mechanisms driving Quaternary glaciations at the southern mid-latitudes. We here present ^{10}Be surface exposure ages from five moraine sets along with Bayesian age modelling to reconstruct a detailed chronology of Last Glacial Maximum expansions of the Río Corcovado glacier, a major former ice conduit of northern Patagonia. We find that the outlet glacier reached maximum expansion of the last glacial cycle during the global Last Glacial Maximum at ~26.5–26 ka, and that at least four subsequent advances/stillstands occurred over a 2–3 ka period, at ~22.5–22 ka, ~22–21.5 ka, ~21–20.5 ka and 20–19.5 ka. The onset of local ice sheet deglaciation likely occurred between 20 and 19 ka. Contrary to several other Patagonian outlet glaciers, including from similar latitudes on the western side of the Andes, we find no evidence for MIS 3/4 advances. Exposure dating of palaeo-shoreline cobbles reconstructing the timing of proglacial lake formation and drainage shifts in the studied region indicate three glaciolacustrine phases characterised by Atlantic-directed drainage. Phase one occurred from 26.4 ± 1.4 ka, phase two between ~21 and ~19 ka and phase three between ~19 ka and ~16.3 ka. Exposure dating of ice-moulded bedrock in the interior of the cordillera indicates local disintegration of the Patagonian Ice Sheet and the Atlantic-Pacific drainage reversal had occurred by ~16.3 ka. We find that local Last Glacial Maximum glacier expansions were coeval with Antarctic and southern mid-latitude atmospheric and oceanic cooling signals, but out of phase with local summer insolation intensity. Our results indicate that local Patagonian Ice Sheet deglaciation occurred 1–2 ka earlier than northwestern, central eastern and southeastern Patagonian outlet glaciers, which could indicate high regional Patagonian Ice Sheet sensitivity to warming and drying during the Varas interstade (~22.5–19.5 ka).

1. Introduction

Patagonia, the southernmost region of South America, is ideally located to further our understanding of Quaternary cryospheric and climatic change in the southern mid-latitudes (Mercer, 1976). The formerly heavily-glaciated Patagonian Andes are part of the only continental landmass that fully intersects the circum-hemispheric Southern Westerly Winds (SWW) and its coupled Antarctic Circumpolar Current (ACC) (Clapperton, 1993, Fig. 1). The mountains span a large latitudinal range and thereby provide the unique opportunity to better understand former migration patterns of key atmospheric- and oceanic-energy re-distributing mechanisms during palaeoclimate transitional phases (Davies et al., 2020).

The once ~2000 km-long (N–S) Patagonian Ice Sheet (PIS)

* Corresponding author. University of Edinburgh, School of GeoSciences, Institute of Geography, Drummond Street, Edinburgh, EH8 9XP, United Kingdom.
E-mail address: tancrede.leger@ed.ac.uk (T.P.M. Leger).

https://doi.org/10.1016/j.quascirev.2021.107194
0277-3791/

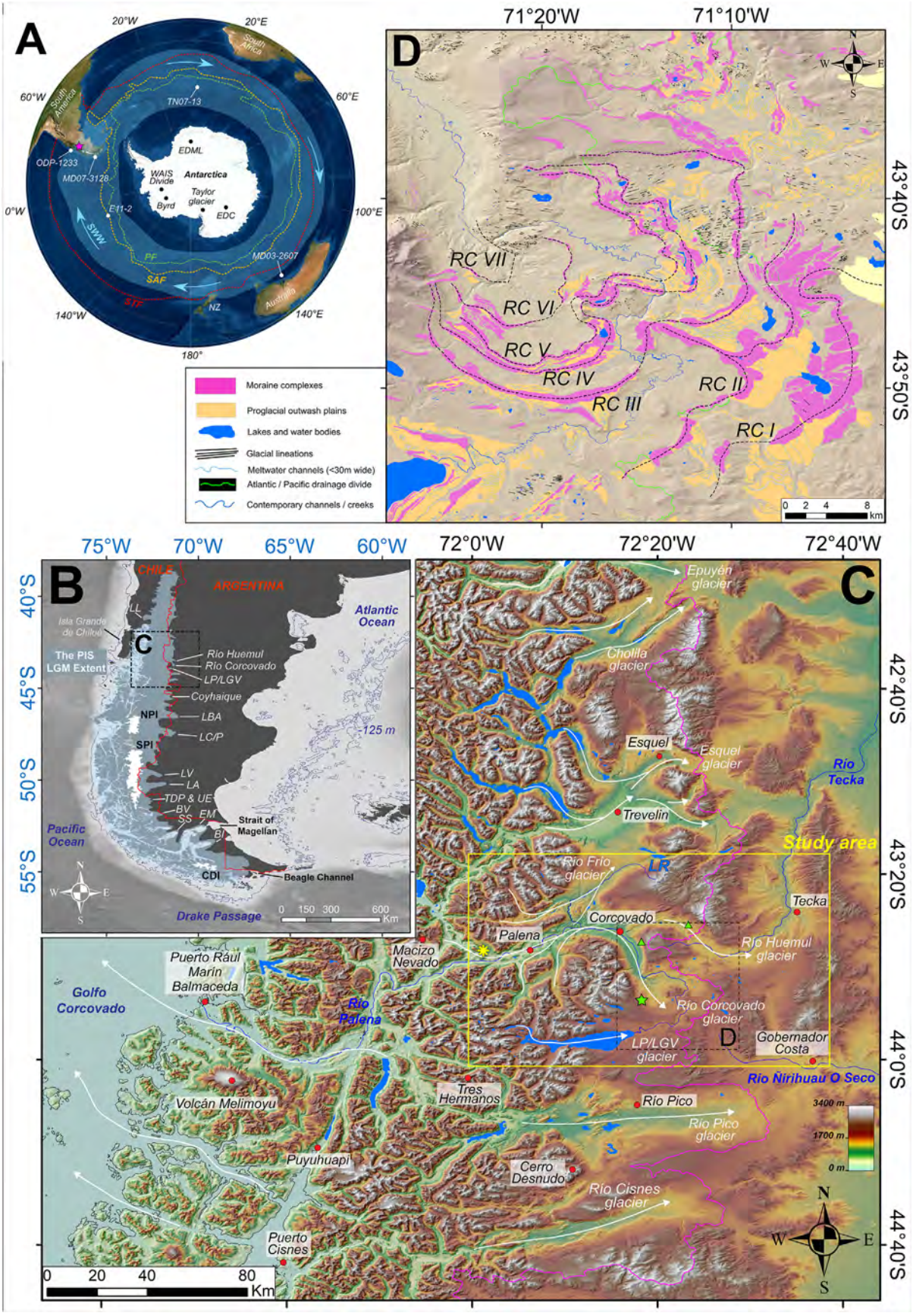

Fig. 1. Location maps of study area. (**A**) Map of Southern Hemisphere highlighting the approximate contemporary positions of the Southern Westerly Winds (SWW: after Sime et al., 2013) belt (light blue), the Polar Front (PF: green), the Sub-Antarctic Front (SAF: orange), and the Sub-Tropical-Front (STF: red), adapted from Darvill et al. (2016) and based on Orsi

largely terminated off-shore on its western margin, but was land-terminating north of ~43° S (Glasser et al., 2008, Fig. 1), enabling geomorphological records to be preserved and accessible (Fig. 1b). Detailed geochronological reconstructions utilising radiocarbon dating have been produced for this land-terminating northwestern sector of the former ice sheet (e.g. Denton et al., 1999; Moreno et al., 2015). Over the past decades, several investigations have moreover produced palaeo-glacier chronologies focusing on the central eastern and southeastern regions of Patagonia (Davies et al., 2020), using mainly terrestrial cosmogenic nuclide (TCN) exposure dating of glacial deposits. However, to date, the ~800 km-extensive (N–S) northeastern sector of the former ice sheet remains less studied (García et al., 2019), although it offers a unique opportunity to compare palaeo-glacier behaviour on both sides of the former ice sheet. This region is currently diagnosed by a lack of knowledge on the characteristics of local PIS development during the last glacial cycle, such as the timing, number and extent of outlet glacier expansion events and their associated meltwater drainage patterns. In this sector, thereby, the precise timing of the local Last Glacial Maximum (LGM) and the last glacial termination are not well constrained.

Numerous investigations from central eastern, southeastern and northwestern Patagonia have reported pre-global LGM maximum outlet glacier expansions occurring for instance during Marine Isotope Stage (MIS) 3 (e.g. Darvill et al., 2015), MIS 4 (e.g. Peltier et al., 2021) and even MIS 5 (Mendelová et al., 2020), but with variable relative magnitude compared to their global LGM (MIS 2) extent. Hence, a latitudinal asynchrony in the magnitude of pre-global LGM advances, with more extensive ice in southeastern Patagonia, has been proposed. Such asynchrony is also thought to characterise the timing of the onset of local deglaciation (García et al., 2019). Therefore, as well as addressing a geographical knowledge gap, establishing robust glacial chronologies from the understudied northeastern region of the former PIS is required to resolve uncertainties concerning latitudinal asynchronies in the precise timing of the local LGM and onset of deglaciation across Patagonia (Darvill et al., 2016). Such information can help to determine the drivers of Quaternary glaciations in the southern mid-latitudes (Kaplan et al., 2008; Kaplan et al., 2005; Kelley et al., 2014; Darvill et al., 2016). Additionally, detailed reconstructions of glaciolacustrine histories during local deglaciation have implications for understanding PIS retreat rates (Bendle et al., 2017a) and events of continental-scale drainage reversal, which can abruptly introduce significant freshwater volumes to coastal environments and force local changes in marine ecosystems and circulation (Glasser et al., 2016; Thorndycraft et al., 2019).

The primary objective of this investigation is to produce a robust chronology of local LGM and deglacial events in a valley system of northeastern Patagonia formerly host to a major PIS outlet glacier; the Río Corcovado (RC) valley system, 43°S, Argentina (Fig. 1). To establish such geochronological reconstruction, we here focus on the remarkably well-preserved record of terminal moraine complexes and associated glaciogenic deposits left by this land-terminating eastern outlet glacier of the PIS, which spans several Quaternary glacial cycles (Caldenius, 1932). While local semi-arid conditions make radiocarbon dating challenging, these moraine records are highly suitable for TCN dating, a method successfully employed in several Patagonian valleys to produce LGM glacial chronologies hitherto (e.g., McCulloch et al., 2005; Kaplan et al., 2004, 2007, 2008; Douglass et al., 2006; Hein et al., 2010; Hein et al., 2011; Hein et al., 2009; Murray et al., 2012; García et al., 2018; Mendelová et al., 2020). Here, by combining interpretations of detailed glacial geomorphological mapping (Leger et al., 2020) and a novel ^{10}Be TCN chronology further constrained with Bayesian age modelling, we provide the first reconstruction of the extent and timing of PIS outlet glacier advances in the RC and neighbouring valleys during the LGM (Fig. 1). In so doing, we also provide insights into the location, elevation and timing of former proglacial lake formation and drainage events associated with retreat patterns of the studied outlet glaciers following the last glacial termination. In addition, our geomorphological and geochronological reconstruction provides an empirical benchmarking framework for tracking the former regional ice-flow direction, palaeolake dynamics, subglacial thermal conditions, and the timing of ice-free environments, all of which are important for improved calibration of numerical ice-sheet models (e.g., Hulton et al., 2002; Hubbard et al., 2005).

1.1. Study location and physical setting

1.1.1. Geographical setting

Our study focuses on a major palaeo-outlet glacier of the northern PIS (Fig. 1), the Palena outlet glacier, which flowed east-northeast from the centre of the former ice sheet, near Macizo Nevado, along the Río Palena (RP) valley. Upon reaching the eastern mountain front, the Palena outlet glacier diverged (43.3°S, 71.3°W) into three branches occupying the Río Frío (RF) valley to the north, the Río Huemul (RH) valley to the east, and the RC valley to the south, where we focus our moraine chronology. The RH and RC outlet glaciers extended up to 60 km to the east/southeast of the Argentinian town of Corcovado (43°54′S; 71°46′W) (Caldenius, 1932; Haller et al., 2003; Martínez et al., 2011). The semi-arid southeastern sectors of the RH and RC valleys (570 mm a^{-1} of precipitation: Fick and Hijmans, 2017), which belong to the Patagonian steppe climate zone, host a series of well-preserved lateral and frontal moraine complexes, along with associated glaciofluvial and glaciolacustrine sediment-landform assemblages (Haller et al., 2003; Martínez et al., 2011; Leger et al., 2020). The RC valley exhibits preservation of at least seven distinct moraine complexes, here termed RC I-VII moraines, from oldest to youngest (Fig. 1d).

The Palena outlet glacier and its RC, RH and RF branches advanced up reverse-graded slopes from a valley floor elevation of ~150 m a.s.l. Near the former ice divide, to the elevation of the major terminal moraine ridges nested between 800 and 1100 m a.s.l. east of the mountain front. Therefore, the modern

et al. (1995) and Carter et al. (2008). The map also highlights the location of our northern Patagonia study site (purple star). The locations of key marine and ice core palaeoclimate records mentioned in the text are illustrated with white dots. Background imagery is from DigitalGlobe (GeoEye, IKONOS, 2000–2011). (**B**) Adapted from Leger et al. (2020). Approximate former extent of the Patagonian Ice Sheet (PIS) during the Last Glacial Maximum (LGM), modified from Glasser et al. (2008) and Glasser and Jansson (2008). Modern extents of the North Patagonian (NPI), South Patagonian (SPI), and Cordillera Darwin (CDI) Icefields are displayed in white. Major former outlet glaciers of the PIS are designated: BI: Bahía Inútil, EM: Estrecho de Magallanes, SS: Seno Skyring, BV: Bella Vista, TDP & UE: Torres del Paine & Última Esperanza, LA: Lago Argentino, LV: Lago Videma, LC/P: Lago Cochrane/Pueyrredón, LBA: Lago Buenos Aires, LL: Lago Llanquihue. Bathymetric data were acquired from the General Bathymetric Chart of the Oceans (GEBCO) and are here shown in greyscale. A −125 m contour roughly simulating former coastline locations at the LGM is displayed (Lambeck et al., 2014). The Chile/Argentina border is shown in red. (**C**) Adapted from Leger et al. (2020). Digital Elevation Model (DEM) of northern Patagonian Andes extrapolated from the ALOS WORLD 3D missions (version 2.2; JAXA; https://www.Eorc.jaxa.jp/ALOS/en/aw3d30/) with a shaded relief background (light azimuth: 315°, incline: 45°) and a sea-level contour (black line) indicating modern coastlines. White arrows designate ice-flow direction of major former PIS outlet glaciers. The pink line delineates the contemporary Atlantic (East)/Pacific (West) drainage divide. Main lake bodies and river channels were manually digitised and are displayed in blue, and labelled when mentioned in the text. Locations of sampling for TCN dating are symbolised by the green star (moraine boulders), the green triangle (shoreline cobbles) and the yellow asterisk (bedrock samples). (**D**) Glacial geomorphological map adapted from Leger et al. (2020) focused on the RC valley moraine and outwash record. Black dashed lines represent our interpretation of the different moraine limits preserved (RCI – RCVII) and their connectivity throughout the field site.

hydrographic drainage of the Río Palena catchment is reversed relative to the flow direction of the former glaciers, with the modern drainage divide located ~70–80 km east of the central spine of the Andes (Davies et al., 2020). Geomorphological mapping of glacial lineations and ice-moulded bedrock outcrops (Leger et al., 2020) indicates that the westward dipping RP, RC and RH valleys were subglacially eroded by warm-based ice. This suggests in turn that the valleys were former conduits for fast-flowing, topographically-controlled outlet glaciers capable of generating significant valley over-deepening during Quaternary glaciations. Such valley over-deepening, greater toward the western margins of the former PIS relative to its eastern margins, is characteristic of the topography for much of Patagonia (e.g. Clapperton, 1993; Singer et al., 2004; Kaplan et al., 2009). The topographic setting helps to explain the preservation of multiple moraine sequences over the Argentinian foreland (Clapperton, 1993; Kaplan et al., 2009), as well as the formation of proglacial lakes during episodes of deglaciation.

1.2. Geologic setting

The field site is located 300 km to the northeast of the Chile triple junction (Hervé et al., 2017), where the Nazca and Antarctic plates subduct in a north-easterly direction beneath the South American plate (~66 mm a^{-1}; Rosenau et al., 2006). The site lies directly east of the Liquiñe-Ofqui Fault Zone (LOFZ), a dextral intra-arc transform fault formed during the late Miocene (10-5 Ma) which extends ~1200 km in a NNE-SSW orientation (from 43°S to 38°S) and has experienced periods of substantial pluton emplacement (Thomson and Hervé, 2002; Lange et al., 2008). The geology of the Palena outlet glacier catchment is dominated by the North Patagonian batholith, formed during the Mesozoic due to local subduction beneath the continental margin and exposed more recently during late-Miocene uplift (Hervé et al., 2017). The batholith in this region is characterised by quartz-bearing pink leucomonzonite, giving way to darker diorite/tonalite and white granodiorite toward the west (Pankhurst et al., 1992). East of Palena and along the RC and RH valleys, the batholith gives way to four main formations of volcanic and sedimentary assemblages (Pankhurst et al., 1992; Haller et al., 2003). These are characterised by: 1) The prevailing Jurassic *Lago La Plata* formation, composed of Andesites, andesitic tuffs, dacites and rhyolites, 2) the lower-cretaceous *Divisadero* formation of lavas, basic to andesitic breccia and andesitic to rhyolitic pyroclastic deposits, interspersed with sedimentary units, 3) the upper cretaceous *Morro Serrano* formation of basic-stock intrusives, veins and dykes, and 4) the rarer mid-cretaceous Río Hielo formation of granites with vein and dyke intrusions (Haller et al., 2003). Consequently, glaciogenic deposits in the field site are characterised by a wide variety of lithologies.

1.3. Climatic setting

The climate of Patagonia is strongly influenced by the Southern Westerly Winds (SWW). The SWW deliver precipitation to the Patagonian Andes, which act as a potent orographic barrier, resulting in a strong west-east rain-shadow effect (Garreaud et al., 2013). At the core of the modern wind-belt, located around central Patagonia (between ~45°S and ~50°S), precipitation on the Pacific coast ranges between 5000 and 10,000 mm a^{-1}, while it diminishes to less than 300 mm a^{-1} east of the mountain front (Garreaud et al., 2013; Lenaerts et al., 2014). In north Patagonia, the SWW are thought to migrate northward and weaken during austral winters, thus causing lower precipitation levels relative to austral summers (Aravena and Luckman, 2009). Annual precipitation near Macizo Nevado, the approximate former ice divide, averages ~1850 mm a^{-1} according to *WorldClim* 2 data (Fick and Hijmans, 2017). Near the terminal margins of the former RC and RH glaciers, which are in the Patagonian steppe climate zone, annual precipitation decreases by 70% to ~570 mm a^{-1}, while modelled mean annual temperature at 1000 m a.s.l. is around 7 °C (*ibid*). The SWW are also an important driver of the Antarctic Circumpolar current (ACC), which after separating into two branches near the Chilean Pacific coast at 45°S, generates the northward-directed Peru-Chile current, bringing cold Subantarctic waters to the Pacific coast of northern Patagonia (Kaiser et al., 2007).

1.4. Previous work in study area

The glacial geomorphology in the study site was first examined and mapped by Caldenius (1932), and later by Lapido (1990), Martínez (2002) and Martínez et al. (2011). Three main glacial sequences were also included in ice-sheet-wide geomorphological investigations by Glasser and Jansson (2008) and Davies et al. (2020) as well as a regional geological map by Haller et al. (2003). While no direct chronology exists, the innermost and youngest preserved moraine sequences were assumed to relate to the local LGM based on morpho-stratigraphic observations and comparisons with other dated moraine records in Patagonia. The first detailed, large-scale geomorphological mapping of ice-contact glaciogenic, glaciofluvial and glaciolacustrine deposits was published recently by Leger et al. (2020).

2. Methods

2.1. Geomorphological mapping

Initial identification of major landforms and topographic features was carried out using the freely available ALOS WORLD 3D - 30 m resolution (AW3D30: Japan Aerospace Exploration Agency) Digital Elevation Model (DEM). All mapped landforms were digitised manually in the WGS84 geographic reference coordinate system using the ESRI™ World Imagery layer, characterised by 1.0 m resolution images from DigitalGlobe (GeoEye, IKONOS, 2000–2011) at the study site (after Bendle et al., 2017 B; Soteres et al., 2020). In areas with high vegetation and/or cloud cover, different colour-rendering comparisons were made using 10 m resolution Sentinel 2A true colour (TCI) and false colour (bands 8,4,3) products (available from https://scihub.copernicus.eu/).

Ground-truthing and/or corrections of preliminary landform interpretations were conducted during two separate field seasons (8 weeks in total) during the 2019 and 2020 austral summers. Geomorphological mapping criteria along with the complete geomorphological map of the area are presented by Leger et al. (2020).

2.2. Moraine morphology/sedimentology analyses

In order to obtain empirical information on glaciogenic sediment deposition history, moraine ridge preservation and its variability across the studied sequence, characteristics of moraine morphology and surface sediments were analysed in the field. We produced topographic profiles for each of the moraine ridges that were sampled for TCN dating using handheld GPS (spatial accuracy: 3–5 m). Where possible, between two and four transects were measured per moraine at >200 m intervals to assess variability along individual ridges. For each transect, we calculated the mean ice-proximal and ice-distal slopes and width-to-height ratios. RC IV-VII moraine clast sediments were investigated on ridge-crest surfaces using a 16 m^2 quadrangle over an area deemed undisturbed and representative of surface sediments. For each quadrangle, surface clast-shape and roundness data were collected

(n = 30 clasts), and clast lithology was recorded. Clast-shape data were plotted on a ternary diagram scaled using *b:a* and *c:a* ratios (Sneed and Folk, 1958; Benn and Ballantyne, 1993) and displaying C_{40} indices (% of *c:a* ratios ≤0.4). Clast-roundness data were plotted as histograms and statistically assessed using *RWR* and *RA* indices (Evans and Benn, 2004; Martin et al., 2019).

2.3. Dating approach and sampling

The wider, highly subdued and less sharp-crested geomorphology of the RC I-II moraines along with a set of twenty-five preliminary (yet unpublished) exposure ages is suggestive of a pre-last glacial cycle age for these outer margins (Leger et al., 2020). The chronology presented here thus focuses exclusively on the younger RC III-VII moraines. To establish a detailed TCN chronology of glacial advances/stillstands and deglacial events in the field area, we measured ^{10}Be concentrations in thirty moraine boulders, six palaeo-shoreline cobbles, and two ice-moulded bedrock surfaces across the study site (Figs. 1c and 2). All sample sites were assessed for topographic shielding using a compass and clinometer.

To establish the timing of the RC III-VII advances/stillstands, we sampled moraine boulders for surface exposure dating (e.g. Gosse and Phillips, 2001; Hein et al., 2010; Heyman et al., 2011). Due to road-access conditions and moraine preservation, we chose the western lateral-frontal environment of the RC basin for sampling of the five most prominent ridges, each belonging to a separate moraine complex (Fig. 2). We targeted large granodiorite boulders (50–190 cm tall) resting directly on the moraine crest that exhibited glacial polish and, in some cases, preserved striations, indicating minimal surface erosion. We collected 1–2 kg samples by hammer, chisel and angle grinder from the top 2–5 cm of the centre of the boulders (Fig. 3). For each target moraine, we sampled six boulders along a single continuous ridge (Fig. 2). This sampling strategy aims to reduce potential uncertainties resulting from geological scatter due to post-depositional processes (Putkonen and Swanson, 2003; Applegate et al., 2010; Heyman et al., 2011; Heyman et al., 2016). We interpret the exposure ages as dating moraine stabilisation following ice-front retreat, hence providing a minimum age for the glacier advance/stillstand.

Two preserved palaeo-shorelines in the RC and RH valleys represent proglacial lake phases during deglaciation. To date the palaeo-shorelines, we sampled three rounded to subrounded,

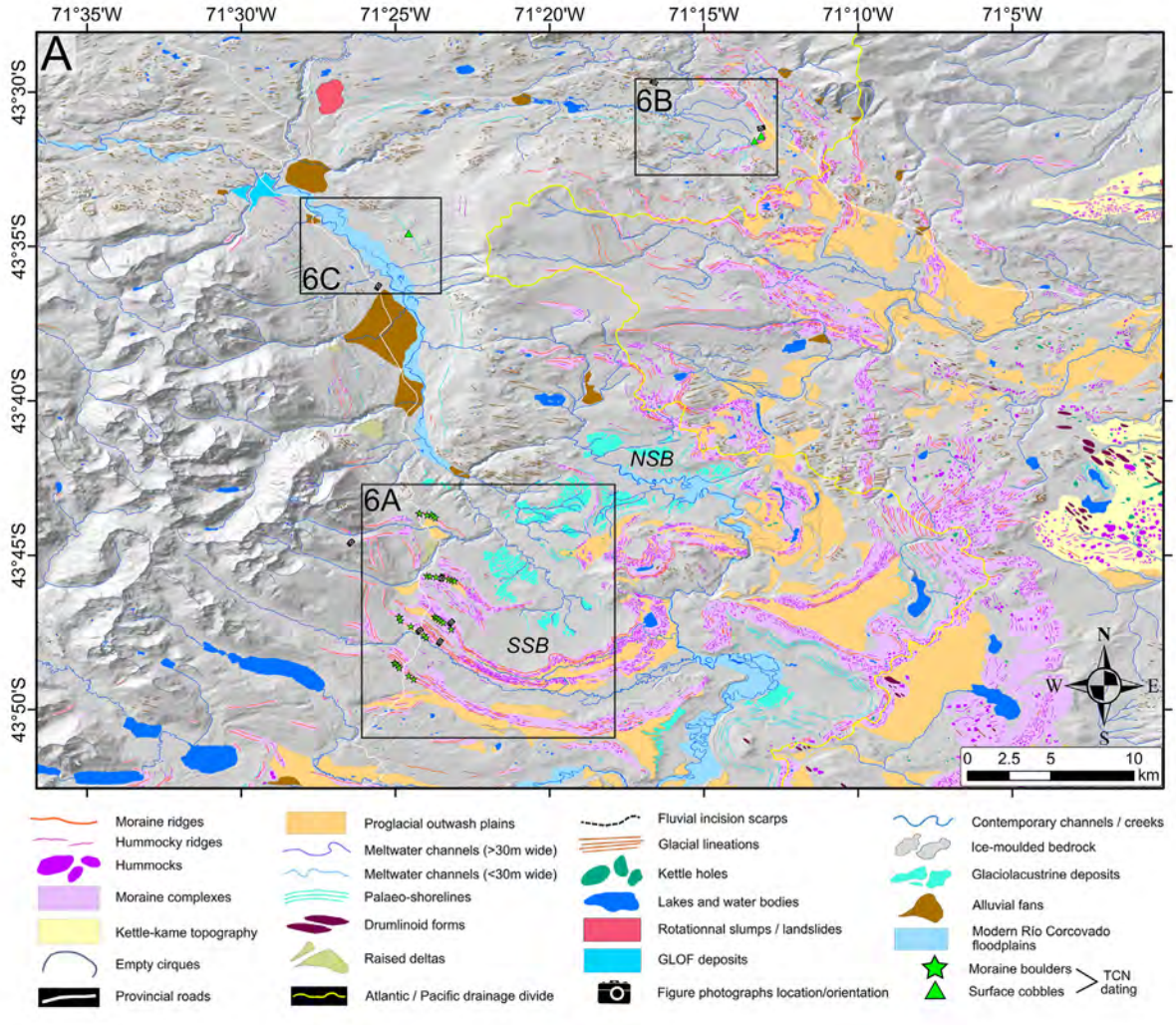

Fig. 2. Geomorphological map (**A**) DEM hillshade (AW3D30 DEM, light azimuth: 315°, incline: 45°) and glacial geomorphological map (adapted from Leger et al., 2020) of the RC and RH valleys and their glaciogenic, glaciofluvial and glaciolacustrine landform-sediment assemblages. The location of moraine boulders and former proglacial lake shoreline surface cobbles sampled for TCN dating are indicated by green star and green triangle symbols, respectively. Camera symbols highlight the location of photographs taken on the field and shown in Figs. 3–5. *SSB*: RC southern sub-basin, *NSB*: RC northern sub-basin.

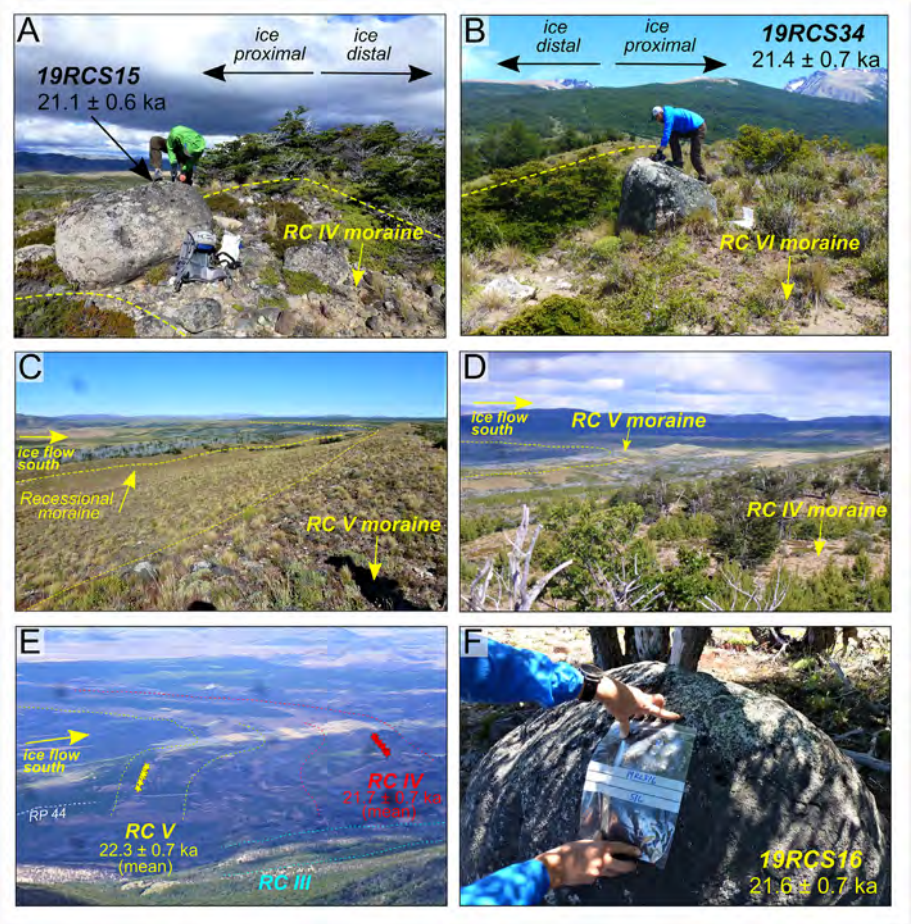

Fig. 3. Field photographs of moraines and sampled boulders. (**A**) Southeast-facing photograph of an erratic granite boulder (sample 19RCS15) deposited on the crest of a RC IV moraine ridge and sampled for TCN dating with hammer and chisel. (**B**) Northwest-facing photograph of a RC VI moraine ridge crest and a granite boulder (19RCS34) sampled for TCN dating. (**C**) Eastward view of the RC V moraine complex, with the most prominent moraine ridge (targeted for sampling) in the foreground, and preserved, smaller recessional ridges in the background (camera location: 43°47′3.67″S). (**D**) Southeastward view from the RC IV moraine complex depicting the terminal environment of the RC V moraine complex, which demonstrate a curved lobate shape (camera location: 43°48′0.14″S, 71°23′28.52″W). (**E**) Photograph captured from the southern mountain ridge of the El Loro valley (camera location: 43°44′38.01″S, 71°27′21.58″W) and looking southeastwards towards the RC V and RC IV moraine complexes in the RC southern sub-basin, which are crossed by the visible RP 44 road. (**F**) Close-up photograph of a granite moraine boulder (19RCS16) sampled for TCN dating from a RC IV moraine ridge, indicating the rounded and preserved nature of its surface.

smooth (i.e., unweathered) surface cobbles from wave-cut platforms etched into sediments draping the valley sides. The cobbles were collected from the flattest sections of the palaeo-shoreline platform, and care was taken to sample away from the backing slope to reduce the risk of post-depositional surface disturbance and contamination from debris-fall. The formation of lake shorelines in sediment deposits is an erosive process mostly conducted by wave action and sediment liquefaction (Sissons, 1978). Our sampling approach thus considers a shoreline wave-cut platform as continuously disturbed by wave action throughout the time of lake residence at its elevation. Such an interpretation is supported by the general presence of more prominent and discernible palaeo-shorelines on the downwind, more wave-exposed eastern valley slopes of the field area (Leger et al., 2020, Figs. 2 and 4). We targeted surface cobbles rather than boulders because they are more easily disturbed by wave action, and are thus less likely to start accumulating cosmogenic radionuclides during lake residence. We therefore suggest the granitic palaeo-shoreline surface cobbles sampled started accumulating ^{10}Be only following shoreline abandonment/stabilisation, and thus interpret their exposure ages as minimum ages for the timing of lake lowering (Fabel et al., 2010; Lifton et al., 2001, 2015; Mendelová et al., 2020b).

To date the final drainage of the proglacial lake, and reconstruct the approximate timing of PIS disintegration in the region, we sampled two ice-moulded (striated/polished) granite bedrock surfaces within the mountain interior and near to the RP valley floor (Figs. 1 and 5). The sample sites are separated by 4.8 km along the valley and differ in elevation by 90 m. We do not expect the bedrock surfaces to have been shielded following the palaeolake drainage and suggest the two bedrock samples date the final lake-level drop below their respective elevations of 254 and 343 m a.s.l.

To provide further chronological constraints on the palaeolake history of the RC valley, we attempted to date the deposition of laminated glaciolacustrine sediments in three different locations using single-grain optically-stimulated luminescence (OSL) dating. The samples were collected using opaque tubes following the methodology described by Smedley et al. (2016) (detailed methodology in supplementary materials).

2.4. Sample preparation and wet chemistry

Samples were prepared at two cosmogenic nuclide laboratories: the University of Edinburgh's Cosmogenic Nuclide Laboratory for sample crushing/sieving and the Natural Environment Research

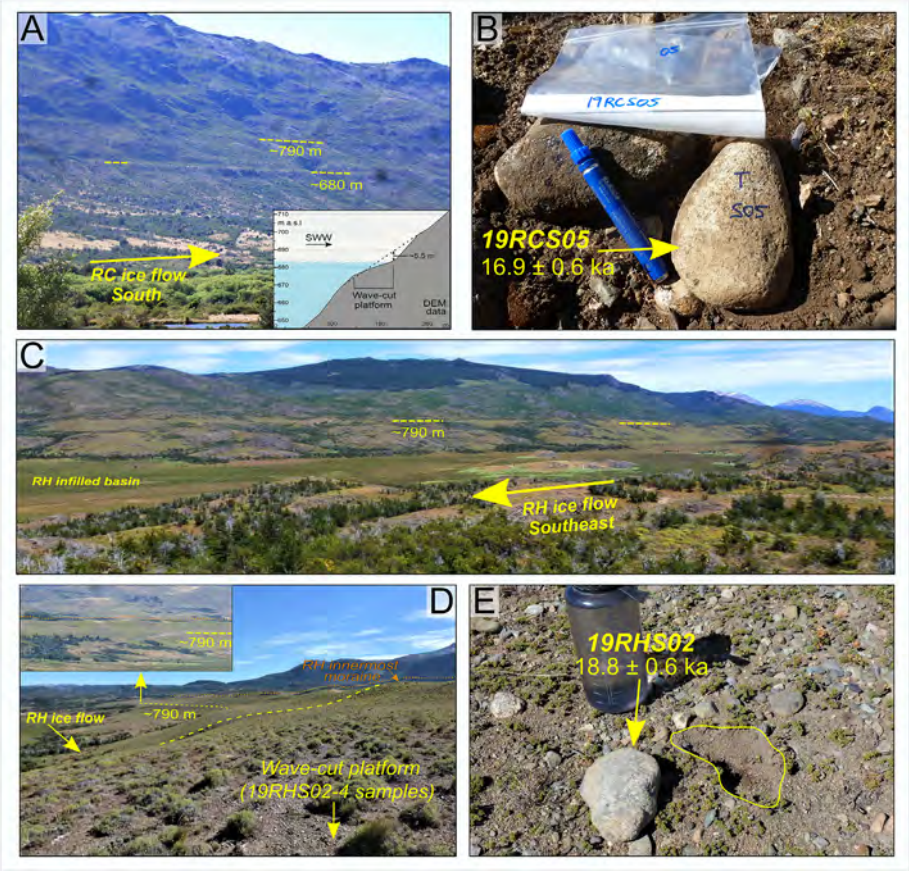

Fig. 4. Field photographs of palaeo-shorelines and surface cobbles sampled (**A**) Southeast-facing photograph of the RC valley trough's eastern mountain slopes showing two well-preserved former proglacial lake shorelines, nested at elevations of ~680 and ~790 m (camera location: 43°36′15.23″S, 71°25′33.20″W). Inset diagram displays a topographic elevation profile from DEM of the lower 680 m palaeo-shoreline photographed, at location of sampling for TCN dating. (**B**) Example of a ~1 kg, well-rounded cobble sampled whole from the RC_{680} former proglacial lake shoreline for TCN dating (19RCS05). This granite cobble was selected for its stable, well-grounded position and because it displayed surface polishing and little evidence of erosion. (**C**) Southeast-facing view of the RH valley's southern/western mountain slope, characterised by numerous outcrops of ice-moulded bedrock and, in some locations, by the preservation of a clear former proglacial lake shoreline (RH_{790}), notched at the elevation of ~790 m a.s.l. (camera location: 43°29′43.45″S, 71°16′31.65″W). (**D**) Northwest-facing photograph captured from the wave-cut platform associated with the RH_{790} former proglacial lake shoreline (highlighted in yellow), and which is notched on the ice-proximal slope of the RH valley's innermost preserved moraine complex (highlighted in orange). The 19RHS02-04 samples were taken from near this location (camera location: 43°31′6.09″S, 71°13′8.59″W). The panel inset is a zoomed-in photograph of this same notched platform, along with the moraine ridge, as seen from the RP 17 road, 3.5 km to the north. (**E**) Photograph of a surface cobble, along with its imprint location, sampled from the RH_{790} former proglacial lake shoreline, which one can observe is mostly composed of sands and well-rounded pebbles and cobbles.

Council's Cosmogenic Isotope Analysis Facility (NERC-CIAF) for the wet chemistry. The samples were crushed and sieved to isolate the 250–500 μm and 125–250 μm grain fractions. To avoid the impact of ^{10}Be concentration decrease with depth on resulting cobble exposure ages, the exposed top 3–5 cm of cobbles with thicknesses greater than 10 cm (n = 2) were cut, crushed and selected for cosmogenic isotope analysis. Smaller (<10 cm) cobbles (n = 4) were crushed whole, however. All $^{10}Be/^{9}Be$ ratios were measured at the Scottish Universities Environmental Research Centre (SUERC) Accelerator Mass Spectrometry (AMS) facility. Further details of the wet chemistry methodology are described in the supplementary materials.

2.5. Age calculations

To ease the comparison of our data with existing regional data (e.g. Davies et al., 2020), ^{10}Be ages were calculated using the online exposure age calculator formerly known as the CRONUS-Earth online calculator (version 3, Balco et al., 2008), and calibrated using the Patagonia (50°S) production rate (Kaplan et al., 2011) obtained from the ICE-D online database (http://calibration.ice-d.org/). In this study, we report ages (including recalculated ages from other studies) using the LSDn-time-dependent scaling scheme of Lifton et al. (2014). Our exposure ages are up to 5.8% and 1.5% older relative to calculations made using the global ^{10}Be production rate (Borchers et al., 2016) and the New Zealand production rate (Putnam et al., 2010), respectively. The contribution of geological scatter on the spread of exposure ages from individual moraines is assessed based on the mean square weighted deviation (MSWD), also referred to as reduced chi-squared (Wendt and Carl, 1991), and whether it is inferior (low scatter) or superior (increasing scatter) to one (Jones et al., 2019). Moreover, we display the MSWD's inferior/superior relationship to the criterion k indicating whether the MSWD value falls within a 2σ envelope, thus testing how well the data represent a single landform (Spencer et al., 2017; Jones et al., 2019). Topographic shielding is negligible, ranging between 0.99 and 1 (Table 1). Exposure ages presented here are interpreted as minimum ages, as we do not include a correction for rock surface erosion, nor for shielding by snow, vegetation or soil. However, applying the erosion rate of 0.2 mm ka^{-1} estimated for semi-arid central Patagonia (46°S; Douglass et al., 2007; Hein et al., 2017) increases our ages by less than 1%, which is within 1σ analytical uncertainties. The semi-arid steppe vegetation of the Argentinian foreland, diagnostic of our field site, allows for sparse vegetation

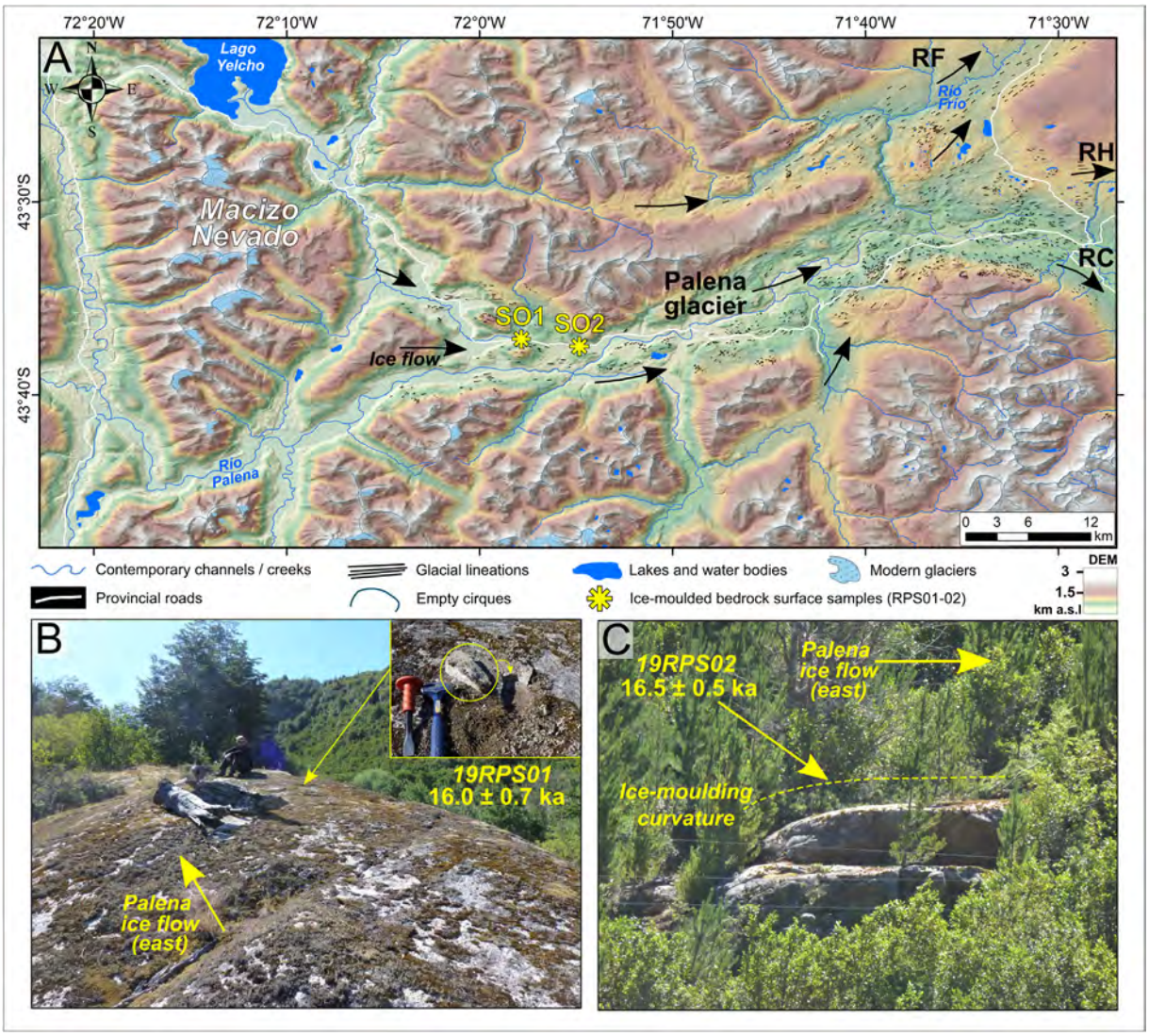

Fig. 5. Ice-moulded bedrock surfaces sampled and geomorphological context. (**A**) DEM and hillshade (AW3D30 DEM, light azimuth: 315°, incline: 45°) of the RP valley, host to the former RP outlet glacier, which fed the former RC, RF and RH outlet glaciers. The map also features the Macizo Nevado mountain massif, which marks the approximate location of the former PIS ice divide during the LGM. The two yellow asterisks demarcate the locations of the two ice-moulded bedrock surfaces sampled for TCN dating (19RPS01-02). Black arrows indicate the approximate former ice-flow direction as suggested by the orientation of mapped lineations. (**B**) Eastward-facing, hence along-former-ice-flow, view of the lower (254 m a.s.l.), rounded and smooth, ice-moulded bedrock surface sampled (19RPS01). (**C**) Photograph captured from the road of the higher (343 m a.s.l.) ice-moulded bedrock surface sampled (19RPS02: camera location: 43°37′30.8″S, 71°54′51.8″W).

and/or soil cover. According to proxy and modelled palaeoclimate data, seasonal precipitation was 40–50% lower than present at the LGM east of the Patagonian Andes (Berman et al., 2016). Moreover, strong and persistent westerly winds (annual mean speed of ~5.3 m s^{-1} at RC moraines location; *WorldClim* 2 data; Fick and Hijmans., 2017) are locally responsible for minimal annual snow cover on protruding landforms, such as moraine crests (Hein et al., 2010; 2009; Mendelová et al., 2020a, 2020b).

We employ a Bayesian age model to facilitate interpretation of the moraine chronology because our chronology presents instances of age reversals relative to the stratigraphic order of events. The Bayesian age model independently integrates sample ages and the relative order of events based on landform stratigraphy to refine probability distributions and produce a stratigraphically consistent chronology. Bayesian models have been widely applied to establish chronologies of lake/marine sediment cores (e.g., Bronk Ramsey, 2008; Bendle et al., 2017a), and is increasingly used for TCN chronologies exhibiting closely spaced landform ages (e.g. Chiverrell et al., 2013; Small et al., 2019). Our Bayesian age model uses the same statistical framework as *OxCal* v4.3 (Bronk Ramsey, 2017) to produce a probability distribution (also termed a posterior density estimate) for each landform, by employing a Markov Chain Monte Carlo sampling approach (model code provided in supplementary materials). The age model was tested with and without prior stratigraphic outlier removal. Such tests only modified modelled mean moraine ages by $\leq$ 0.8%, thus remaining lower than 1σ analytical uncertainties. Best Gaussian fit statistics were also calculated for each landform and were found to vary by less than 0.1% relative to arithmetic means.

3. Results

3.1. Geomorphology/sedimentology

3.1.1. The RC III-VII moraines geomorphology

The RC III-VII moraines are located at the southern margin of the

Table 1
Sample details and nuclide concentrations.

Sample ID	Latitude (DD)	Longitude (DD)	Elevation (m a.s.l.)	Boulder height (m)	Thickness (cm)	Shielding correction	Qtz mass dissolved (g)	^{10}Be atoms g^{-1} (SiO_2)	±1σ atoms g^{-1} (SiO_2)	$^{10}Be/^{9}Be$ ratio	±1σ	AMS ID - Laboratory facility
RC III - VII moraine boulders												
19RCS21	−43.80806	−71.41719	1105	0.65	2.0	0.999885	19.9171	2.597E+05	8.684E+03	3.253E-13	9.661E-15	b11801 CIAF
19RCS23	−43.80942	−71.41534	1101	1.20	4.0	0.999866	15.8740	2.626E+05	8.216E+03	2.760E-13	7.523E-15	b11775 CIAF
19RCS24	−43.81067	−71.41458	1101	1.40	3.0	0.999866	13.8700	2.340E+05	6.900E+03	2.124E-13	5.254E-15	b11908 CIAF
19RCS25	−43.81500	−71.40953	1102	1.20	3.5	0.999913	16.2847	2.653E+05	7.907E+03	2.733E-13	6.953E-15	b11803 CIAF
19RCS27	−43.81553	−71.40936	1101	1.20	3.5	0.999913	20.0920	2.538E+05	8.328E+03	3.202E-13	9.290E-15	b11804 CIAF
19RCS28	−43.81683	−71.40681	1101	0.55	2.0	0.999902	18.0367	2.723E+05	8.623E+03	3.098E-13	8.569E-15	b11805 CIAF
19RCS13	−43.79436	−71.40003	1003	1.00	2.5	0.999848	17.6247	2.789E+05	9.360E+03	3.087E-13	9.189E-15	b11797 CIAF
19RCS15	−43.79294	−71.40147	1014	0.60	2.5	0.999823	20.1200	1.902E+05	5.476E+03	2.504E-13	6.102E-15	b11774 CIAF
19RCS16	−43.78314	−71.41467	1040	1.00	1.5	0.999628	20.0033	2.011E+05	5.826E+03	2.541E-13	6.216E-15	b11798 CIAF
19RCS17	−43.78328	−71.41444	1037	0.95	1.0	0.999628	19.9809	2.009E+05	6.749E+03	2.531E-13	7.497E-15	b11799 CIAF
19RCS51	−43.79319	−71.40125	1017	0.70	2.0	0.999823	18.3354	2.097E+05	6.529E+03	2.444E-13	6.551E-15	b11800 CIAF
19RCS52	−43.78831	−71.40828	1038	0.80	1.5	0.999708	19.4590	1.975E+05	5.785E+03	2.531E-13	6.314E-15	b11786 CIAF
19RCS38	−43.78992	−71.38647	944	0.80	1.0	0.999810	18.9125	1.964E+05	8.458E+03	2.355E-13	9.337E-15	b11811 CIAF
19RCS40	−43.78544	−71.39206	950	0.40	1.5	0.999744	19.6800	1.898E+05	5.516E+03	2.455E-13	6.053E-15	b11780 CIAF
19RCS41	−43.78453	−71.39325	955	0.65	4.0	0.999744	20.0916	1.850E+05	6.295E+03	2.360E-13	7.084E-15	b11812 CIAF
19RCS42	−43.78364	−71.39456	953	0.45	1.5	0.999708	19.0720	1.700E+05	4.799E+03	2.146E-13	5.055E-15	b11781 CIAF
19RCS43	−43.78317	−71.39550	959	1.30	1.0	0.999708	13.1830	1.902E+05	5.916E+03	1.669E-13	4.413E-15	b11784 CIAF
19RCS44	−43.78278	−71.39633	954	1.00	1.5	0.999708	10.0460	2.030E+05	6.900E+03	1.364E-13	3.985E-15	b11785 CIAF
19RCS30	−43.76381	−71.38469	884	0.60	2.0	0.999657	14.3670	1.706E+05	5.672E+03	1.621E-13	4.664E-15	b11777 CIAF
19RCS31	−43.76414	−71.38417	892	0.65	0.8	0.999662	20.7070	1.561E+05	5.040E+03	2.118E-13	5.951E-15	b11778 CIAF
19RCS33	−43.76167	−71.39467	902	0.65	2.0	0.999720	20.4102	1.651E+05	5.434E+03	2.129E-13	6.105E-15	b11806 CIAF
19RCS34	−43.76119	−71.39819	903	1.35	1.5	0.999330	20.0644	1.776E+05	5.945E+03	2.260E-13	6.633E-15	b11807 CIAF
19RCS32	−43.76281	−71.38789	896	0.50	2.0	0.999678	19.9450	1.438E+05	4.744E+03	1.907E-13	5.477E-15	b11779 CIAF
19RCS36	−43.76125	−71.39806	902	0.35	2.0	0.999330	20.0644	1.768E+05	5.965E+03	2.251E-13	6.668E-15	b11810 CIAF
19RCS07	−43.72744	−71.40378	832	1.90	1.5	0.987187	19.1640	1.325E+05	4.112E+03	1.689E-13	4.458E-15	b11772 CIAF
19RCS08	−43.72981	−71.39514	824	1.15	0.4	0.998614	19.5762	1.585E+05	5.614E+03	1.979E-13	6.186E-15	b11792 CIAF
19RCS09	−43.72889	−71.39619	824	0.70	0.8	0.998605	20.2413	2.185E+05	5.834E+03	2.771E-13	6.073E-15	b11793 CIAF
19RCS11	−43.72803	−71.39725	829	0.70	3.5	0.998826	20.0857	1.435E+05	4.678E+03	1.821E-13	5.106E-15	b11794 CIAF
19RCS12	−43.72733	−71.40350	835	1.12	3.5	0.987187	20.5940	1.771E+05	5.074E+03	2.397E-13	5.790E-15	b11773 CIAF
RC20-29	−43.72755	−71.40289	832	0.86	1.0	0.997521	11.7200	1.850E+05	5.500E+03	1.443E-13	3.493E-15	b11909 CIAF
RC and RH palaeo-shoreline surface cobbles												
19RHS02	−43.52400	−71.21931	792	n/a	3.5	0.999062	14.9340	1.365E+05	4.729E+03	1.362E-13	4.078E-15	b11787 CIAF
19RHS03	−43.52631	−71.22264	788	n/a	4.0*	0.999010	20.3670	1.399E+05	4.480E+03	1.881E-13	5.202E-15	b11788 CIAF
19RHS04	−43.52631	−71.22264	788	n/a	4.8*	0.999010	20.0991	1.427E+05	4.815E+03	1.836E-13	5.377E-15	b11814 CIAF
19RCS05	−43.57639	−71.40939	673	n/a	3.0	0.996840	20.7050	1.102E+05	4.215E+03	1.493E-13	5.079E-15	b11771 CIAF
19RCS04	−43.57617	−71.40958	671	n/a	2.9	0.996840	14.2900	1.082E+05	3.300E+03	1.033E-13	2.445E-15	b11907 CIAF
19RCS03	−43.57617	−71.40958	671	n/a	2.8	0.996840	14.7000	9.980E+04	3.200E+03	9.636E-14	2.385E-15	b11905 CIAF
Río Palena valley surface bedrock samples												
19RPS01	−43.61828	−71.96400	343	n/a	3.5	0.985559	19.9158	7.616E+04	3.554E+03	9.789E-14	4.026E-15	b11813 CIAF
19RPS02	−43.62458	−71.91403	254	n/a	1.5	0.979415	23.5850	7.310E+04	2.400E+03	1.160E-13	3.262E-15	b11790 CIAF

Rock density is assumed to be 2.65 g cm^{-3}. *Samples that were cut prior to crushing, reported thickness relates to top, exposed surfaces selected for analysis after cutting. Concentrations were corrected for process blanks; blank corrections ranged between ~1.4 and 4.6% of the sample $^{10}Be/^{9}Be$ ratios. The uncertainty of the blank correction is included in the stated one-sigma uncertainties. Measurements were normalised to NIST SRM4325 with nominal $^{10}Be/^{9}Be$ ratios of 2.79 x 10^{-11}, corresponding to a ^{10}Be half-life of 1.36 Ma (Nishiizumi et al., 2007). CIAF: Cosmogenic Isotope Analysis Facility, all measurements were made at the AMS facility at the Scottish Universities Environmental Research Centre (SUERC), East Kilbride, Scotland.

former RC outlet glacier (Fig. 6a; 43°46′S, 71°23′W). Geomorphological mapping highlighted five distinct moraine complexes composed of over 40 individual ridges reflecting numerous still-stands of the RC glacier front. The moraines range from m-scale, hardly perceptible ridges, to prominent, high relief (10–40 m), arcuate and sharp-crested ridges with steep slopes (9–19°), thus indicating a more prolonged period of ice-front stability. The most pronounced ridges appear unbroken and can be traced as continuous ridges over tens of km. They exhibit a double-lobate outline indicative of two former piedmont lobes across the width of the RC valley; caused by a valley-central 300 m-high bedrock step acting as an obstacle to ice flow (Fig. 2). In certain ice-front configurations (RC III – RC V), geomorphological mapping therefore suggests a RC glacier terminus branching off into two piedmont outlets occupying two respective sub-basins of the RC valley (Fig. 2). The northern sub-basin exhibits a low slope gradient, and the moraine complexes are more widely separated than in the steeper southern sub-basin.

The innermost (RC VII) and outermost (RC III) moraines lie 10.2 km from each other and range in elevation (at the location of sampling) from ~820 m a.s.l. to ~1100 m a.s.l., respectively (Fig. 6a). The five sampled moraines exhibit mean height-to-width ratios of between 6.6 and 11.4, and range in ice-proximal and ice-distal slope gradients from 9° to 19° (Fig. 7). Clast-shape analyses from the RC IV-VII moraine surfaces (n = 30 per moraine) indicate a clear dominance of blocky clasts, with a uniform C_{40} percentage of 13.3%. All RC IV-VII moraines have a greater percentage of rounded to sub-rounded surface clasts (Fig. 7). However, the RC VII moraine surface presents a comparatively higher percentage of angular clasts (30%) relative to the RC IV-VI average (12%). Although analogous to other RC moraines in orientation, size, slope gradients and surface clast-shape-and-size, the RC VII moraine is not as sharp-crested, and has

a flatter, wider and more subdued crest surface with little variation in crest-line elevation. Contrary to the RC III-VI moraines, the RC VII moraine is not part of a complex including numerous superimposed recessional ridges, instead comprising a single, prominent ridge.

Along with other igneous extrusive lithologies (andesites, andesitic tuffs, dacites and rhyolites), the RC III-VII moraines contain an abundance of quartz-bearing granodiorite boulders (Fig. 3). Moraine boulder erosion is variable and not correlated with the relative age of the moraine. For example, on each sampled moraine we found some boulders with polished, striated, and well-rounded surfaces, while others displayed minor erosion by granular disintegration (depth < 2 cm), and still others displayed significant (depth 2–4 cm) surface weathering pits. All surfaces sampled for TCN dating, however, demonstrated evidence of smooth polish, in some cases emerging from more weathered adjacent surfaces, and indicative of limited surface erosion where sampled.

3.1.2. The RH and RC former glaciolacustrine phases

Our geomorphological mapping revealed an abundance of glaciolacustrine sediment-landform assemblages in the RC and RH valleys, such as palaeo-shorelines, laminated clay-to-sand-sized sediment accumulations, raised deltas and spillway openings (Leger et al., 2020, Fig. 4). We interpret these assemblages as associated with proglacial lakes and as indicative of ice damming the westward, Pacific-directed drainage of the Corcovado, Huemul and Frío rivers following initial ice retreat from local LGM margins. We reconstructed former palaeolake elevations by matching the elevations of palaeo-shorelines, raised deltas, glaciolacustrine sediment deposits and major spillways indicative of the lowest drainage route through terminal glaciogenic deposits (Clapperton et al., 1993; Turner et al., 2005). Indeed, such geomorphological markers can procure evidence for lake-level falls following ice-front retreat and spillway shifts (Turner et al., 2005; Bell, 2008; Hein et al., 2010; Glasser et al., 2016; Thorndycraft et al., 2019). All geomorphological observations interpreted as markers of former proglacial lake levels are compiled in supplementary table 1, while our interpretation of the strongest sources of lake-level evidence are described in the discussion section of this manuscript. Our mapping and field interpretations suggest at least three main glaciolacustrine phases in the study region during and following local LGM glacial expansions. Phase one describes a proglacial lake formed at the elevation of 990 ± 5 m when the RC glacier ice-front was positioned at the RC III moraine while phase two is associated with a proglacial lake initially formed in the RC northern sub-basin, at the elevation of ~790 m, and following RC ice-front retreat from its RC V margin. OSL samples from exposures of rippled sands and varves elevated at 709 m and 686 m, thought to be deposits associated with proglacial lake phase two, yielded burial ages of 34.9 ± 2.9 ka and 52.1 ± 4.4 ka, respectively (Supplementary materials). The third phase is characterised by the formation of a larger lake system elevated at ~680 m and connecting all valleys of the field site during local deglaciation of outlet glaciers. Our geomorphological interpretations based on field investigations of former proglacial lake geographic extent, timing, drainage directions, spillway locations and residence time for each

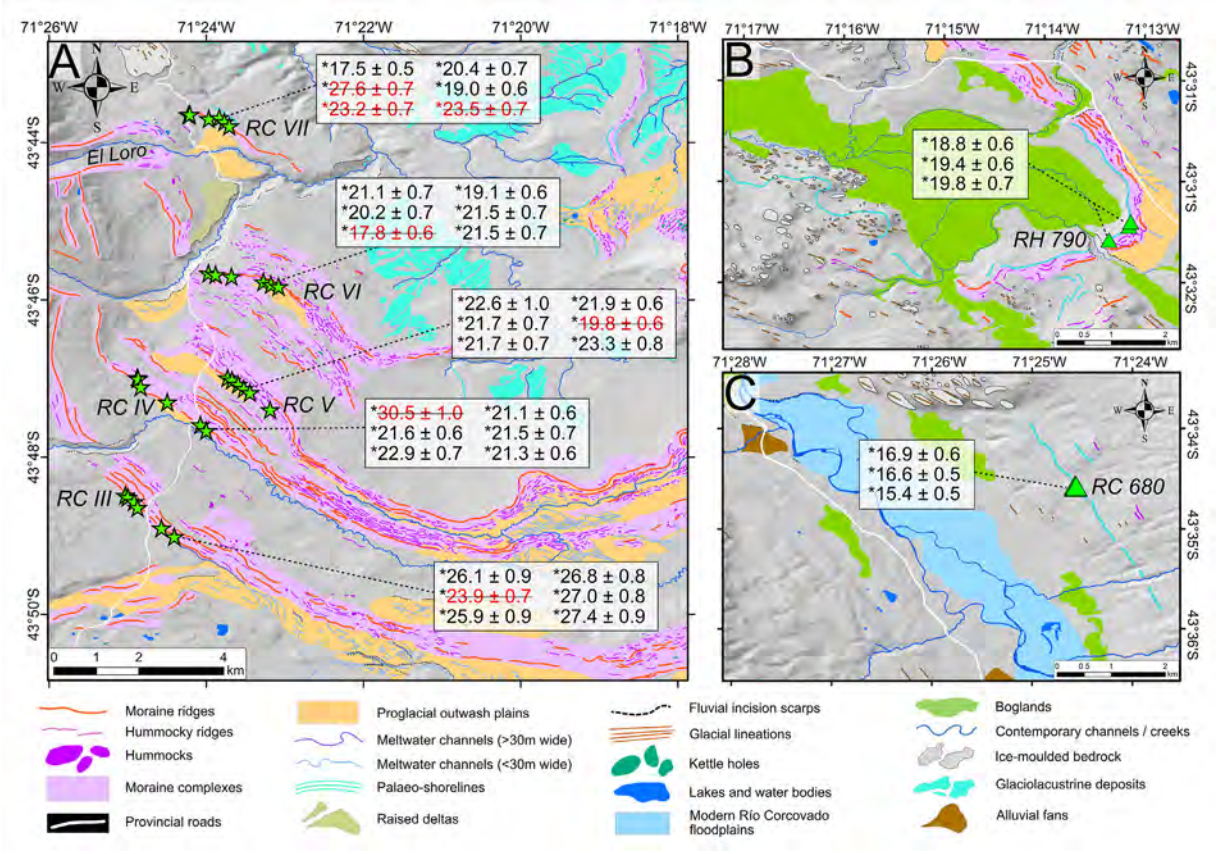

Fig. 6. TCN dating chronology and geomorphological context of moraine boulder and palaeo-shoreline surface cobble samples (**A**) DEM hillshade (AW3D30 DEM, light azimuth: 315°, incline: 45°) and glacial geomorphological map (adapted from Leger et al., 2020) enhanced on the RC LGM moraine sequence sampled. Individual ^{10}Be exposure ages (prior to Bayesian age model correction) and analytical internal uncertainties (n = 6 per moraine) are indicated, along with identified outliers (in red). (**C**) and (**D**) maps focusing on the location and exposure ages of surface cobbles sampled from the RH_{790} and RC_{680} former proglacial lake shorelines, respectively.

reconstructed phase is described further in the discussion section of this paper as well as in the supplementary materials.

3.2. Dating results

3.2.1. Cosmogenic ^{10}Be exposure ages

The ^{10}Be data (n = 38) are summarised in Tables 1 and 2 while kernel density estimates (1σ ranges) per individual sample and landform along with Bayesian age modelling probability distributions are presented in Fig. 8.

The outermost RC III moraine yielded ages ranging from 23.9 ± 0.7 ka to 27.4 ± 0.9 ka (n = 6). The youngest age was interpreted as an outlier as it lies outside the remaining population's 95% confidence (2σ) envelope and was statistically rejected on the basis of a χ^2 test at 95% confidence (Ward and Wilson., 1978). The remaining exposure ages range from 25.9 ± 0.8 ka to 27.4 ± 0.9 ka, display a well-clustered age distribution, with a low MSWD value of 0.53, and yield an arithmetic mean of 26.6 ± 0.6 ka.

The six boulders from the RC IV moraine range in age from 21.1 ± 0.6 ka to 30.4 ± 1.0 ka. The oldest age, being significantly older than the older RC III moraine, is discarded as a stratigraphic outlier. The remaining dataset (n = 5) ranges from 21.1 ± 0.6 ka to 22.9 ± 0.7 ka, yielding a mean exposure age of 21.7 ± 0.7 ka, and representing a clustered dataset (MSWD = 1.08).

The six boulders from the RC V moraine range in age from 19.8 ± 0.6 ka to 23.3 ± 0.8 ka. We consider the youngest age an outlier because it lies outside the remaining population's 95% confidence (2σ) envelope, is younger than the mean age of the adjacent younger RC VI moraine (see below), and was taken from a comparatively short boulder (45 cm in height). Moreover, this younger age was statistically rejected on the basis of a χ^2 test at 95% confidence. We therefore consider it likely that this boulder was exhumed post-deposition and underestimates the age of the moraine. The remaining population (n = 5) ranges from 21.7 ± 0.7 ka to 23.3 ± 0.8 ka, yields a mean exposure age of 22.3 ± 0.7 ka, and demonstrates a well-clustered dataset (MSWD = 0.76) (Table 2, Fig. 8).

The six boulders from the RC VI moraine range in age from 17.8 ± 0.6 ka to 21.5 ± 0.7 ka. We consider the youngest age an outlier because it is 1 ka younger than the mean age of the younger adjacent RC VII moraine (see below). Moreover, it was statistically rejected on the basis of a χ^2 test at 95% confidence and was also sampled from a comparatively short (50 cm in height) boulder that may have been exhumed post moraine deposition. The remaining

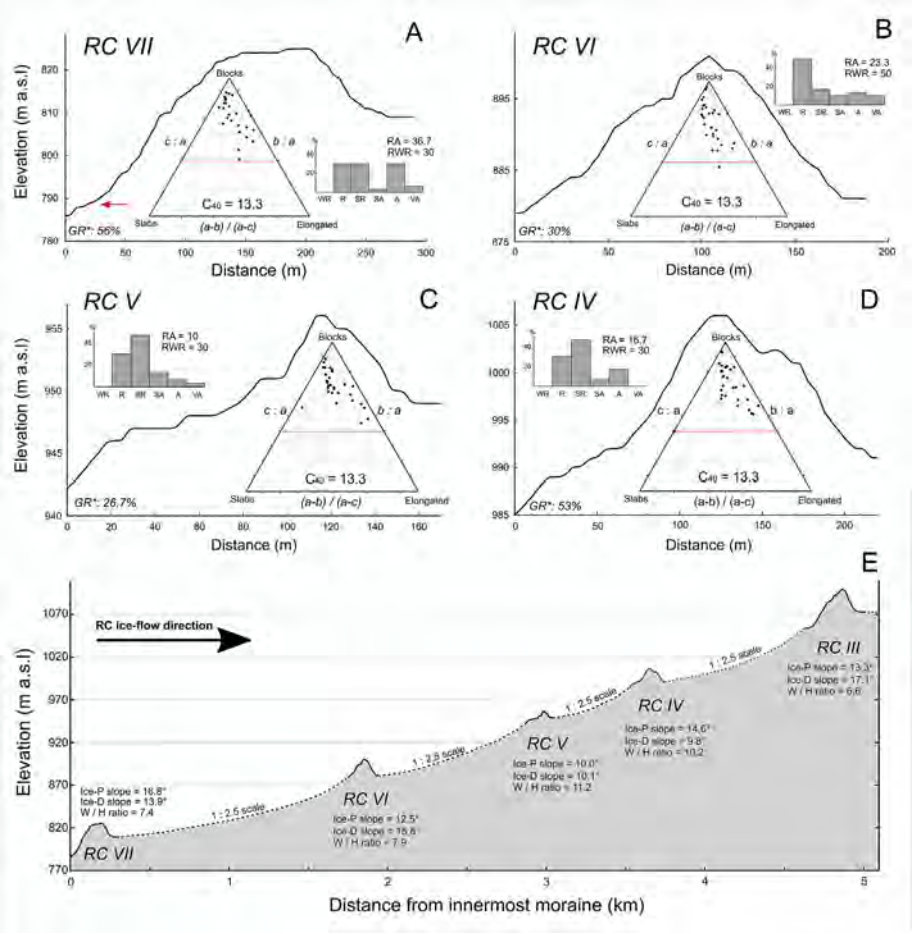

Fig. 7. Geomorphological and sedimentological data for the RC III – RC VII moraines near the TCN dating locations. (**A-D**) Two-dimensional cross elevation profiles of the RC IV – RC VII moraines, measured from hand-held GPS transects (3–5 m vertical/spatial accuracy), along with ternary diagrams (scaled using *b:a* and *c:a* ratios) depicting moraine clast shape data from surface 16 m^2 quadrangles (n = 30 clasts per quadrangle). Clast-roundness histograms are also displayed for each of these moraines (WR = Well-rounded; VA = Very angular). *RWR* and *RA* indices indicate, respectively, the percentages of rounded and well-rounded clasts and the percentages of angular and very angular clasts for each sampled population (Evans and Benn, 2004; Martin et al., 2019). (GR*) in each panel notes the percentage of granitic clasts sampled per population. (**E**) Elevation profile of the entire RC LGM moraine sequence, with GPS transects displayed for each moraine. The GPS transects, along with moraine absolute and relative elevations, are displayed to scale. The horizontal distance separating moraines, however, is displayed at a 1: 2.5 scale (dotted black lines). Also annotated against each moraine are ice-proximal (Ice-P) and ice-distal (Ice-D) slope gradients, and width-to-height (W/H) ratios.

sample ages (n = 5) range from 19.1 ± 0.6 ka to 21.5 ± 0.7 ka, yield a mean exposure age of 20.6 ± 1.0 ka, and demonstrate a high and >1 MSWD value of 2.33, thus suggestive of greater age scatter than predicted solely by analytical uncertainties.

The six boulders from the RC VII moraine range in age from 17.5 ± 0.5 ka to 27.6 ± 0.7 ka. Based on stratigraphy, we interpret the three oldest exposure ages of 23.2 ± 0.7 ka, 23.5 ± 0.7 ka and 27.6 ± 0.7 ka as outliers yielding inheritance as their ages are greater than the older, adjacent RC VI-IV moraines and lie outside of the 2σ envelope. The remaining population (n = 3) ranges from 17.5 ± 0.5 ka to 20.4 ± 0.7 ka, yields a mean exposure age of 19.00 ± 1.5 ka, and exhibits a high and >1 MSWD value of 5.34, indicating greater age scatter than can be predicted by analytical uncertainties only.

The three cobbles sampled from the RH_{790} palaeo-shoreline range in age from 18.7 ± 0.6 ka to 19.8 ± 0.7 ka. The distribution of ages is well-clustered, with a MSWD value of 0.62. The population's mean exposure age is 19.3 ± 0.5 ka.

The three cobbles sampled from the RC_{680} palaeo-shoreline range in age from 15.4 ± 0.5 ka to 16.9 ± 0.6 ka, and exhibit a reasonably clustered dataset, with a MSWD value of 2.24, which is inferior to *k* (3.0). The MSWD value is greater than 1, however, and is diagnostic of some geologic scatter in the age distribution. The three samples yield a mean exposure age of 16.3 ± 0.8 ka.

The two RP ice-moulded bedrock surfaces provide ages of 16.0 ± 0.7 ka and 16.5 ± 0.5 ka. The ages are well-clustered, with a MSWD value of 0.24 The mean exposure age for the two samples is 16.3 ± 0.3 ka.

3.2.2. Bayesian age modelling results

Bayesian age model probability distributions were produced for the RC III-RC VII moraine and the RH_{790} palaeo-shoreline age populations to resolve age-inconsistencies when compared to the relative order of events based on our geomorphological interpretations. For instance, the RC IV moraine is ~1.1 km further from the ice source than the RC V moraine and thus is morphostratigraphically older (Figs. 2 and 6a), yet the exposure ages from both moraines exhibit overlapping age distributions and reversed mean ages (i.e., RC V is older than RC IV). This suggests the two moraine ages are indistinguishable within analytical dating uncertainties. Moreover, our morphostratigraphic interpretation suggests the RC VII advance/stillstand should be older than the proglacial lake abandonment of the RH_{790} palaeo-shoreline (proglacial lake phase 2/3 transition). Mean exposure ages indicate the opposite (RH_{790} ~0.3 ka older than RC VII); a mismatch that we attribute to analytical surface exposure dating uncertainties and the significant scatter in RC VII moraine boulder ages. Consequently, Bayesian age modelling was employed to produce more realistic age probability distributions that follow the relative order of events based on our geomorphological reconstruction. Discussions regarding the age of the RC_{680} palaeo-shoreline and the ice-moulded bedrock samples (19RPS01-02), however, are based on the arithmetic mean and 1σ analytical uncertainty associated with the original exposure ages, as they did not display any age-inconsistencies in the relative order of events, and because including them in the Bayesian age model would add a mathematical bias resulting in slightly older, less-realistic mean ages relative to original exposure ages. Therefore, exposure ages from these two landforms were not included in the Bayesian age model.

The Bayesian age model probability distributions resulted in mean output ages of 26.4 ± 1.4 ka (−0.7% correction), 22.4 ± 1.15 ka (+3.5% correction), 21.7 ± 0.9 ka. (−2.7% correction), 20.7 ± 1.0 ka (+0.5% correction), 19.9 ± 1.1 ka (+4.6% correction) and 19.0 ± 0.9 ka (−1.8% correction) for the RC III, IV, V, VI, VII and RH_{790} landforms, respectively (Table 2, Fig. 8).

4. Discussion

4.1. Style of glaciation

Our geomorphological and sedimentological analyses of the sampled LGM RC moraines highlight relatively steep moraine slopes, sharp ridges, and exceptional ridge continuity throughout the field site (Figs. 2 and 7). The continuity of moraine ridges suggests progressive ice recession without re-advances that could partially dismantle or over-print older moraines, in part due to the westward-dipping nature of bed topography, which might play a role in preventing moraine over-printing and glaciofluvial erosion of older moraines. The sampled ridges (~10–15 m in mean height) are part of relatively wide moraine complexes composed of numerous smaller ridges, interspersed by narrow, confined glaciofluvial deposits (Leger et al., 2020, Figs. 2 and 7). Such characteristics are indicative of significant sediment volume delivery to the ablation zone during LGM advances/stillstands of the RC glacier. Along with widespread geomorphological evidence of efficient subglacial erosion through mapping of lineations and ice-moulded bedrock surfaces (*ibid*), the evidence indicates the RC outlet glacier was highly erosive and warm-based in nature.

4.2. Chronological and geomorphological results interpretation

Our results indicate at least five (RC III-VII) distinct advances/stillstands of the RC glacier during the LGM. Bayesian age modelling of boulder exposure ages suggests that the RC III-VII moraines were deposited over a 6–7 ka period, with major advances/stillstands occurring at 26.4 ± 1.4 ka, 22.4 ± 1.15 ka, 21.7 ± 0.9 ka, 20.7 ± 1.0 ka and 19.9 ± 1.1 ka (Fig. 8). Our ^{10}Be chronology therefore suggests that all dated RC moraines were formed during the global LGM (*ca.* 26.5–19 ka; Clark et al., 2009), and that maximum local LGM ice-extent was reached at ~26.5 ka. We argue that the RC glacier remained close (within 15 km) to its outermost LGM extent until 19.5–20 ka. The timing of these advances/stillstands is in good agreement with LGM records from other Patagonian regions (e.g. Denton et al., 1999; Kaplan et al., 2004; Hein et al., 2010; Boex et al., 2013; Moreno et al., 2015; Stern et al., 2015; Smedley et al., 2016; Garcia et al., 2019). Our analysis also revealed three phases of proglacial lake formation. Exposure ages from the RH_{790} palaeo-shoreline surface cobbles, interpreted as representing the timing of shoreline abandonment and phase two proglacial lake-level drop (19.0 ± 0.9 ka; Table 2, Fig. 8), enable us to constrain the onset of local deglaciation and understand former glaciolacustrine drainage shifts. Finally, exposure ages from the RP valley ice-moulded bedrock surfaces (16.3 ± 0.3 ka) provide geochronological insights into the timing of local PIS disintegration and Atlantic/Pacific drainage reversal, coeval with the age of glaciolacustrine phase three shoreline-abandonment (16.3 ± 0.8 ka). In this section, and with reference to the schematic Fig. 9, we present our interpretation of local LGM and deglacial events supported by the geomorphological and geochronological evidence.

4.2.1. The local LGM (RC III) and proglacial lake phase one (Fig. 9a)

We interpret the RC III moraine, dated to 26.4 ± 1.4 ka, as representing the maximum extent of the local LGM for the RC outlet glacier. Our geomorphological reconstruction suggests this advance coincided with the formation of the first proglacial lake, located in the RC southern sub-basin (Fig. 9a). The geomorphology suggests the lake was dammed in the northwest by the RC glacier ice-front when positioned at the RC III moraine, in the south and east by the older RC II moraine complex, and in the southwest by the Lago Palena/General Vintter ice-front. This relatively small proglacial lake (Fig. 9a), was fed by meltwater from both the RC and Lago

Table 2
Exposure ages and summary statistics.

Kaplan et al. (2011) production rate										
Sample ID	LSDn: Lifton et al. (2014)			St: Lal (1991) and Stone (2000)			Lm: Lal (1991) and Stone (2000)			Outlier?
	Age	Internal	External	Age	Internal	External	Age	Internal	External	
	Cal Yr BP			Cal Yr BP			Cal Yr BP			
RC III moraine boulders										
19RCS21	26075	877	2310	27149	914	2419	26157	880	2329	
19RCS23	26845	846	2357	27992	882	2473	26943	849	2378	
19RCS24	23907	709	2082	24721	733	2166	23932	710	2096	Yes
19RCS25	26981	810	2355	28138	845	2471	27081	813	2376	
19RCS27	25887	855	2287	26933	890	2393	25961	857	2305	
19RCS28	27365	873	2407	28553	911	2526	27468	876	2429	
Mean (n = 6): 26.18 ka; 1σ std: 1.24 ka										
Mean (n = 5): 26.63 ka; 1σ std: 0.63 ka; 1σ internal: 1.91 ka; 1σ internal + PR%: 2.90 ka										
Bayesian age model (n = 5): **26.43** ka; 1σ std: **1.39** ka; model correction: -0.7%										
Uncertainty weighted mean (n = 5): 26.63 ka; 1σ std: 0.56 ka										
MSWD: 0.53 < *k*: 2.41 (n = 5); Peak age (n = 5): 26.70 ka										
RC IV moraine boulders										
19RCS13	30447	1029	2701	31800	1076	2838	30485	1031	2719	Yes
19RCS15	21074	610	1829	21434	621	1872	20942	606	1828	
19RCS16	21575	629	1874	22031	642	1925	21480	626	1876	
19RCS17	21525	727	1906	21970	742	1957	21426	724	1907	
19RCS51	22895	717	2007	23497	736	2072	22809	714	2010	
19RCS52	21254	626	1849	21662	638	1895	21148	623	1849	
Mean (n = 6): 23.13 ka; 1σ std: 3.64 ka										
Mean (n = 5): 21.66 ka; 1σ std: 0.72 ka; 1σ internal: 1.48 ka; 1σ internal + PR%: 2.31 ka										
Bayesian age model (n = 5): **22.41** ka; 1σ std: **1.15** ka; model correction: +3.5%										
Uncertainty weighted mean (n = 5): 21.63 ka; 1σ std: 0.63 ka										
MSWD: 1.08 < *k*: 2.41 (n = 5); Peak age (n = 5): 21.37 ka										
RC V moraine boulders										
19RCS38	22650	981	2098	23142	1002	2155	22486	974	2092	
19RCS40	21936	641	1907	22349	653	1954	21767	636	1902	
19RCS41	21745	744	1929	22136	758	1975	21576	738	1924	
19RCS42	19803	562	1715	19956	566	1738	19586	556	1705	Yes
19RCS43	21747	680	1906	22143	693	1952	21582	675	1901	
19RCS44	23272	796	2065	23835	815	2127	23126	791	2063	
Mean (n = 6): 21.86 ka; 1σ std: 1.17 ka										
Mean (n = 5): 22.27 ka; 1σ std: 0.67 ka; 1σ internal: 1.74 ka; 1σ internal + PR%: 2.52 ka										
Bayesian age model (n = 5): **21.67** ka; 1σ std: **0.91** ka; model correction: -2.7%										
Uncertainty weighted mean (n = 5): 22.22 ka; 1σ std: 0.59 ka										
MSWD: 0.76 < *k*: 2.41 (n = 5); Peak age (n = 5): 21.97 ka										
RC VI moraine boulders										
19RCS30	21060	704	1862	21280	711	1892	20804	695	1849	
19RCS31	19124	620	1683	19152	621	1695	18839	611	1666	
19RCS33	20151	667	1778	20287	671	1801	19891	658	1765	
19RCS34	21451	722	1898	21740	732	1935	21221	714	1888	
19RCS32	17825	591	1573	17753	588	1575	17526	581	1554	Yes
19RCS36	21462	728	1901	21750	738	1938	21231	720	1891	
Mean (n = 6): 20.18 ka; 1σ std: 1.46 ka										
Mean (n = 5): 20.65 ka; 1σ std: 1.01 ka; 1σ internal: 1.54 ka; 1σ internal + PR%: 2.29 ka										
Bayesian age model (n = 5): **20.75** ka; 1σ std: **1.05** ka; model correction: +0.5%										
Uncertainty weighted mean (n = 5): 20.59 ka; 1σ std: 0.92 ka										
MSWD: 2.33 < *k*: 2.41 (n = 5); Peak age (n = 5): 21.18 ka										

(*continued on next page*)

Table 2 (*continued*)

Kaplan et al. (2011) production rate										
Sample ID	LSDn: Lifton et al. (2014)			St: Lal (1991) and Stone (2000)			Lm: Lal (1991) and Stone (2000)			Outlier?
	Age	Internal	External	Age	Internal	External	Age	Internal	External	
	Cal Yr BP			Cal Yr BP			Cal Yr BP			
RC VII moraine boulders										
19RCS07	17532	547	1534	17382	542	1530	17177	535	1511	
19RCS08	20443	728	1824	20526	731	1842	20111	716	1804	
19RCS09	27654	743	2386	28454	765	2470	27412	737	2378	Yes
19RCS11	19015	623	1675	18971	621	1681	18668	611	1653	
19RCS12	23192	668	2013	23600	680	2061	22914	660	2000	Yes
RC20-29	23535	704	2052	23968	717	2102	23257	695	2038	Yes
Mean (n = 6): 21.90 ka; 1σ std: 3.66 ka										
Mean (n = 3): 19.00 ka; 1σ std: 1.46 ka; 1σ internal: 1.10 ka; 1σ internal + PR%: 1.91 ka										
Bayesian age model (n = 3): **19.88** ka; 1σ std: **1.07** ka; model correction: +4.6%										
Uncertainty weighted mean (n = 3): 18.86 ka; 1σ std: 1.18 ka										
MSWD: 5.34 > *k*: 3.0 (n = 3); Peak age (n = 3): 19.19 ka										
Río Huemul 795 m palaeo-shoreline surface cobbles										
19RHS02	18790	654	1670	18660	649	1668	18381	640	1642	
19RHS03	19355	623	1701	19268	620	1703	18949	610	1674	
19RHS04	19834	672	1757	19791	671	1762	19435	659	1730	
Mean (n = 3): 19.33 ka; 1σ std: 0.52 ka; 1σ internal: 1.13 ka; 1σ internal + PR%: 1.94 ka										
Bayesian age model (n = 3): **18.99** ka; 1σ std: **0.95** ka; model correction: -1.8%										
Uncertainty weighted mean (n = 3): 19.32 ka; 1σ std: 0.42 ka										
MSWD: 0.62 < *k*: 3.0 (n = 3); Peak age (n = 3): 19.34 ka										
Río Corcovado 680 m palaeo-shoreline surface cobbles										
19RCS05	16917	650	1528	16576	637	1505	16407	630	1489	
19RCS04	16640	510	1453	16291	499	1430	16142	494	1416	
19RCS03	15416	496	1354	15009	483	1326	14930	481	1318	
Mean (n = 3): **16.32** ka; 1σ std: **0.80** ka; 1σ internal: 0.96 ka; 1σ internal + PR%: 1.65										
Uncertainty weighted mean (n = 3): 16.27 ka; 1σ std: 0.66 ka										
MSWD: 2.24 < *k*: 3.0 (n = 3); Peak age: 16.69 ka										
Río Palena valley surface bedrock samples (Atlantic/Pacific drainage reversal)										
19RPS01	16023	751	1510	15473	725	1465	15328	718	1450	
19RPS02	16474	543	1452	15925	525	1411	15749	519	1395	
Mean (n = 2): **16.25** ka; 1σ std: **0.32** ka; 1σ internal: 0.93 ka; 1σ internal + PR%: 1.62 ka										
Uncertainty weighted mean (n = 2): 16.28 ka; 1σ std: 0.22 ka										
MSWD: 0.24 < *k*: 3.83 (n = 2); Peak age (n = 2): 16.36 ka										

Ages were calculated using the online calculator formerly known as the CRONUS-Earth online calculator version 3 (Balco et al., 2008) with the Patagonian production rate (Kaplan et al., 2011) obtained from the ICE-D online database (http://calibration.ice-d.org/). Scaling schemes: St-time-independent version of Lal (1991) and Stone (2000), Lm is the time dependent version of Lal (1991) and Stone (2000), and LSDn-time-dependent scheme of Lifton et al. (2014). In the text, we report ages calculated using the LSDn scaling scheme within internal uncertainties. Ages are reported with 1σ internal and external uncertainties, the latter including production rate and scaling uncertainties. These ages assume zero erosion and no correction for shielding by snow, soil and/or vegetation. Elevation flag is std. Summary statistics were calculated for each dated landform. This includes arithmetic means with 1σ standard deviations (std), 1σ propagated (from individual ages) internal uncertainties, and propagated 1σ internal plus production rate uncertainty (PR%). It also includes uncertainty weighted mean and 1σ standard deviation, MSWD and Peak age statistics; calculated using the iceTEA tools for exposure ages online calculator (Jones et al., 2019). For the RC III − RC VII moraines and the RH_{790} palaeo-shoreline, summary statistics also display Bayesian age model outputs, which include arithmetic means, 1σ standard deviations, and model correction percentages relative to original landforms arithmetic mean. Ages in bold represent the ones used throughout the paper for discussion.

Palena/General Vintter outlet glaciers into a 100 m deep basin, now host to the modern Río Corcovado and its floodplain (Fig. 2). Preserved palaeo-shorelines indicate a maximum former lake elevation of 990 ± 5 m and a main spillway (43°50′59″S, 71°11′13″W) suggestive of southeast-directed drainage towards the contemporary Ñirihuau O Seco river. Using a DEM we estimate a maximum lake area of 139 km^2 and volume of 8.2 km^3 (Fig. 9a).

The RC III advance is coeval with a glacial expansion event documented on the western side of the Patagonian Andes at similar latitudes to this study (Isla de Chiloé; 42–43°S; García et al., 2012), and more recently dated to 26.0 ± 2.9 ka through OSL dating (García et al., 2021). Moreover, several advances at about 26 ka have been reported across the entire latitudinal extent of the former PIS (Supplementary Figure 2). For instance, moraine and glaciofluvial outwash deposits dating to 28–26 ka were discovered for the Bahía Inútil-San Sebastían glacier (53–54°S: Río Cullen drift: Kaplan et al., 2007, 2008; Darvill et al., 2015), the Magellan glacier (52°S: Primera Angostura and B limits: Kaplan et al., 2007, 2008), the Lago Cochrane/Pueyrredón glacier (47.5°S: Río Blanco I moraine: Hein et al., 2010), the Lago General Carrera/Buenos Aires glacier (46.5°S: Fenix IV, V moraines: Kaplan et al., 2004; Douglass et al., 2006), and for several outlet glaciers of the Chilean Lake District (Denton et al., 1999; Moreno et al., 2015). Moreover, numerous synchronous glacial advances were also recorded in the New

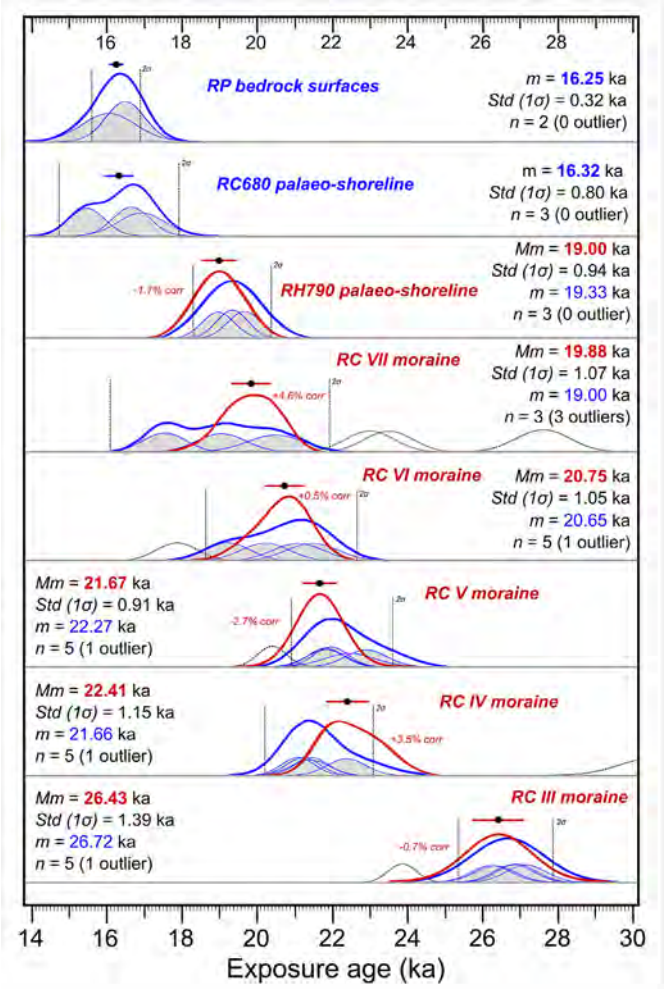

Fig. 8. Probability density diagrams for each of the landforms dated with TCN dating. Thick blue curves represent the summed probability distribution for each sampled landform, excluding outliers. Thin blue curves depict the 1 σ Gaussian curves for individual exposure ages. Black dotted curves represent outliers. Thick red curves illustrate the summed probability distribution after Bayesian age model correction (RC III – RH_{790} only). Black dots describe the arithmetic means (excluding outliers) while red/blue horizontal error bars indicate the standard deviation of the exposure ages. Vertical, black dotted lines denote the 2 σ confidence interval associated with exposure-age populations prior to Bayesian age model corrections. *Mm* stands for "Modelled mean" and indicates the Bayesian age model arithmetic mean, while *m* stands for "mean" and displays the arithmetic mean prior to Bayesian age model correction. *Std* stands for "standard deviation".

Zealand Southern Alps at around 26.5 ka (the *Otira 5* advance: Shulmeister et al., 2019). Such synchronous glacial response implies that potent cooling and/or increased precipitation occurred at 28–26 ka throughout Patagonia and across the southern mid-latitudes.

Several other Patagonian and southern hemisphere investigations reconstructing detailed glacier geochronologies have reported maximum ice extents of the last glacial cycle occurring before the global LGM, during MIS 3 (e.g. Denton et al., 1999; Darvill et al., 2015; Moreno et al., 2015; García et al., 2018, 2021), MIS 4 (Schaefer et al., 2015; De Deckker et al., 2019; Hall et al., 2020; Peltier et al., 2021; García et al., 2021), and even MIS 5 (Mendelová et al., 2020). Evidence of MIS 3 glacial activity was detected as far north as the Chilean Lake District (40°S; Denton et al., 1999), where outlet glaciers reached a similar extent at ~33 ka to that during the global LGM (MIS 2). Furthermore, a new study from Isla de Chiloé (42–43°S; García et al., 2021), located on the western side of the Andes at an equivalent latitude to our study site, suggest that local maximum glaciation occurred earlier in the last glacial cycle, at 57.8 ± 4.7 ka, and this advance was approximately 4 km more extensive than the local MIS 2 advance. In southern Patagonia, these early advances were far more extensive than during the global LGM, in some cases (Torres del Paine glacier: 51°S, Última Esperanza glacier: 51.4°S, and the Bahía Inútil–San Sebastián glacier: 53.5°S) extending twice as far as during MIS 2 (García et al., 2018; Darvill et al., 2015). The MIS 3 local maximum appears to fade out toward central Patagonia where there is evidence for MIS 3 glacial activity of similar magnitude to the global LGM at Lago Pueyrredón (47.5°S; Hein et al., 2010) and Lago Buenos Aires (46.5°S; Smedley et al., 2016). In northeastern Patagonia, however, our new TCN reconstruction reveals the first assessment of the local maximum glaciation on both sides of the former ice sheet. In contrast to the west, we find the local maximum glaciation on the eastern side occurred during the global LGM. This suggests that any MIS 3 glacial activity in the RC valley was comparatively restricted and subsequently overridden by the RC III advance (MIS 2: 26.0 ± 2.9 ka). Hence, in addition to supporting a latitudinal disparity across Patagonia, our results also suggest a West/East disparity in the relative magnitude and extent of PIS expansions during MIS 3. The precise mechanisms causing such zonal disparity remain unknown and represent an area of future research. However, one could hypothesise that the PIS was potentially less sensitive to relatively short-lived, millennial-scale stadials characteristic of MIS 3 in its central eastern and northeastern sector, due to locally-specific conditions of upward-sloping valley floors, a strong rain-shadow effect causing lower moisture availability and the widespread occurrence of large proglacial lakes amongst other environmental factors (García et al., 2021). Combined, these factors may delay ice build-up in northeastern and central eastern Patagonia, a region where PIS outlet glaciers may require more stable and long-lived stadials to advance up reversed slopes.

4.2.2. *The RC IV-RC VII advances and proglacial lake phase two (Fig. 9b–e)*

Bayesian age modelling of RC moraine boulder exposure ages indicates that the second oldest LGM advance occurred at 22.4 ± 1.15 ka (RC IV moraine, Fig. 9b). Our chronology displays a ~4 ka period between age model outputs from the RC III and RC IV sampled ridges during which time the stability and location of the RC glacier front is unknown. Indeed, the RC III moraine boulders were sampled on the outermost of five distinct, more subtle moraine ridges within this complex (Leger et al., 2020, Fig. 2). These smaller ridges are indicative of periods of ice-front stability following the deposition of the RC III moraine. Further dating on these ridges could resolve whether the ice margin terminated within this intermediate zone at this time, or whether it is more likely the glacier retreated within the basin and then readvanced to deposit the RC IV moraine. Within either scenario, topographic analyses and detailed mapping of meltwater channels and glaciofluvial deposits suggest that subsequent retreat of the RC glacier from its RC III margin caused a complex re-arrangement of local meltwater drainage pathways. By opening a lower, northeast-directed drainage pathway, meltwater from the Lago Palena/General Vintter glacier and the RC southern sub-basin shifted from draining southward towards Río Ñirihuau O Seco (and Río Senguer) to a network of channels flowing northeastwards towards Río Tecka (and Río Chubut). We suggest this event also led to the end of proglacial lake phase one (Fig. 9a and b). In both cases, meltwater drained eastward into the Atlantic but via different routes (Martínez et al., 2011).

The RC V moraine (modelled age: 21.7 ± 0.9 ka, Fig. 9c) was

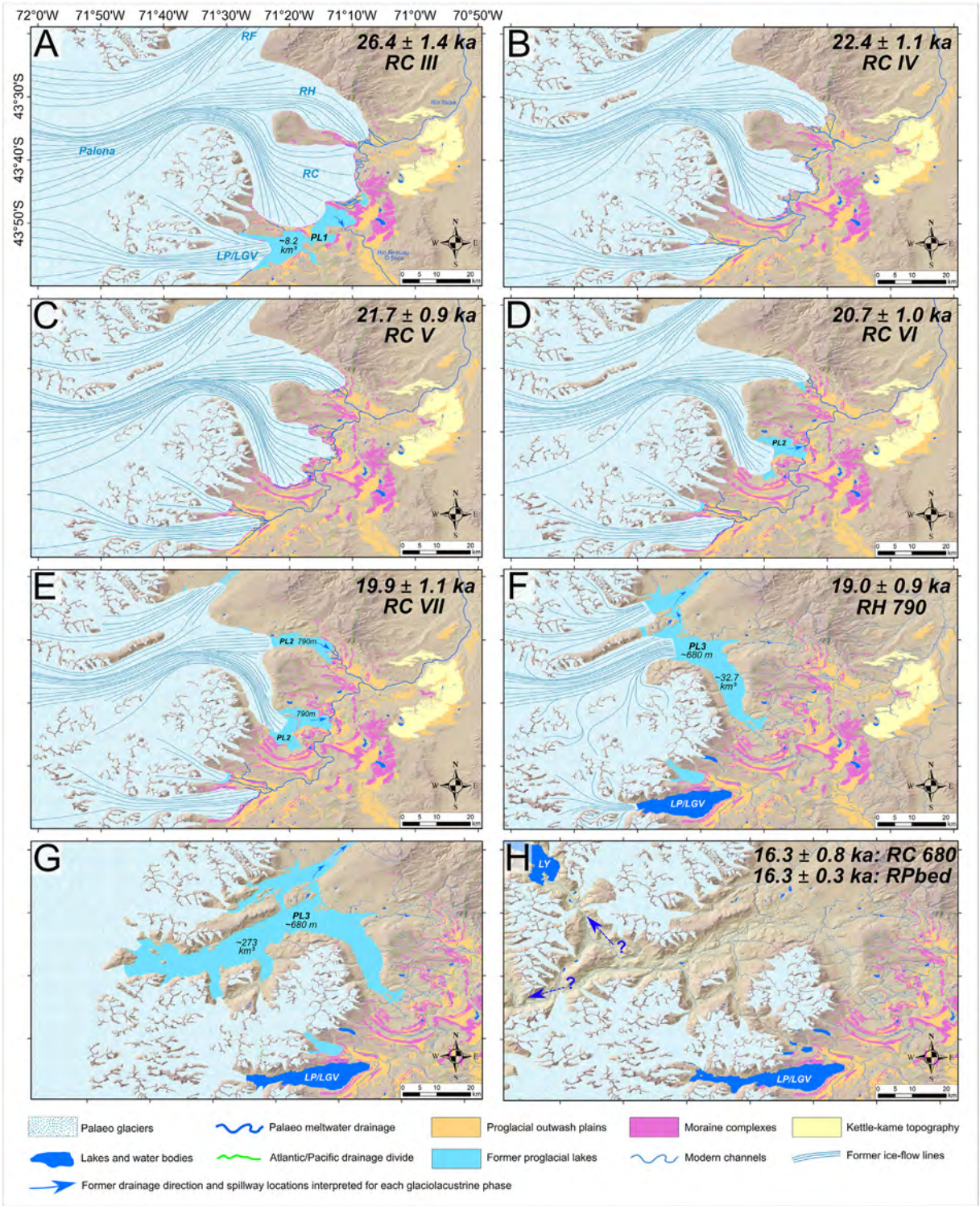

Fig. 9. Palaeoglacial and palaeolake reconstructions for the RC, RH, RF and Lago Palena/General Vintter valleys, for each LGM advances/stillstands and deglacial events interpreted in this investigation. Ice-sheet and mountain glacier models were digitised manually in ArcGIS. Apart from when delineated by confidently mapped moraine limits (e.g. the RC, RH and LP/LGV LGM moraine sequences), the position of ice margins are inferred. (**A-E**) Ice extents associated with the RC III to RC VII moraine complexes. This includes the formation of glaciolacustrine phase one and two (here termed PL1 and PL2, respectively). There are no previously published chronologies in the RH, RF and LP/LGV valleys. The relative ice extent in those neighbouring valleys is thus inferred based on our RC chronology and cross-valley comparisons of moraine numbers, preservation and morphostratigraphy. Hence, these inferences yield some uncertainties. (**F**) Reconstruction of the opening of the RF valley scenario and the subsequent RC proglacial lake lowering to 680 m (dated with surface cobbles from the RH_{790} shoreline), marking the onset of glaciolacsutrine phase 3 (here denoted: PL3), according to our geomorphic interpretation. (**G**) Reconstruction of the westward retreat of the RP outlet glacier towards the core of the Andes and the associated expansion of the 680 m proglacial lake. (**H**) Reconstruction of the onset of PIS disintegration, enabling ice-dam collapse and the Pacific-directed, final drainage of the 680 m proglacial lake (PL3). Proglacial lake volume estimates were computed from DEM data (AW3D30). Panel H question marks relate to the uncertainty regarding the former drainage pathway(s) employed during the local Atlantic/Pacific drainage reversal event. Location of ice fronts for panels F–H are hypothetical as not correlated to specific geomorphic limits, but are aimed at representing specific events/scenarios.

deposited close to the RC IV moraine, just 0.9 km inboard at the location of sampling, compared with a separation of 2.25 km between RC III and IV. Despite this proximity, we consider the RC IV and V moraine complexes to represent distinct deposits because they are interspersed by a narrow yet distinct glaciofluvial outwash plain near their terminal environment (Leger et al., 2020, Fig. 2). However, exposure ages from the two moraines overlap and display means that are reversed with their relative stratigraphic age. In other words, the mean age of the two moraines are indistinguishable within analytical uncertainties. The geographical and chronological proximity of these two moraines and the significant sediment volume they represent suggests a relatively long period of ice-front stability for the RC glacier at around 22 ka (Fig. 9b and c).

The RC VI moraine (modelled age: 20.7 ± 1.0 ka) was deposited ~2 km further inboard, ~50 m lower in elevation (at location of sampling) and approximately 1 ka after the RC V moraine (Figs. 7, 8 and 9d). Our RC VI samples come from the most prominent ridge of a 1.5 km-wide moraine complex featuring a minimum of four older and five younger distinct moraine ridges (Leger et al., 2020, Fig. 2), thus suggestive of another prolonged period of ice-front stability at around 21 ka.

Geomorphological mapping of palaeo-shorelines indicates that the western retreat of the RC ice-front from the RC V moraine complex initiated the formation of a second proglacial lake phase (surface elevation: 790 m) in the RC northern sub-basin (Fig. 9d). Indeed, remote sensing and field observations revealed the relatively widespread occurrence of palaeo-shorelines nested at the elevation of ~790–800 m in both the RC and RH valleys (Leger et al., 2020, main map). In the RC valley, the palaeo-shorelines can be discerned across the northern sub-basin, notched on the ice-proximal slopes of the RC V moraine complex (Supplementary materials). We propose a lake formation age, bracketed by the modelled RC V and RC VI formation ages, of between 20.7 ± 1.0 ka and 21.7 ± 0.9 ka. Ages from the RH_{790} shoreline were interpreted as indicating shoreline abandonment and thus lake-level drop from ~790 m to ~680 m associated with the transition from glaciolacustrine phase two to phase three. Based on a mean modelled age of 19.0 ± 0.9 ka for the RH_{790} palaeo-shoreline (Fig. 8), we suggest a total residence time for the proglacial lake at ~790 m of 1.5–2.5 ka. During this time, we argue that this proglacial lake enabled meltwater runoff from the LP/LGV, RC and RH glaciers to drain towards the Atlantic via Río Tecka. We suggest the 790 m proglacial lake's main spillway occurred at 43°42′S, 71°13′W, where the prominent shoreline bends eastwards into a 200 m-wide gorge breaching the RC V and RC IV moraine complexes.

Approximately 10 km to the northwest, in the more topographically constrained RC trough, isolated remnants of the 790 m palaeo-shoreline can be discerned on the eastern hillslope (Fig. 4a), while evidence of this shoreline disappears north of 43°37′S. This indicates that the 790 m proglacial lake expanded and persisted during the early stages of local deglaciation, when the RC calving front progressively retreated northward. This is supported by the finding of fine, sand to clay-sized sediment deposits exposed through sections of the valley's main road (RP44), at elevations of 686 m (43°42′7.2″S), 709 m (43°42′15.2″S) and 720 m (43°42′11.7″S). These exposures exhibit laminations and varves, represent the topmost unit below soil, and were interpreted as glaciolacustrine deposits. OSL samples from the exposures of rippled sands and varves at 709 m and 686 m yielded burial ages of 34.9 ± 2.9 ka and 52.1 ± 4.4 ka, respectively (Supplementary materials). We consider these ages to be older than the deposition of these sediments, despite the use of single grains to overcome the effects of incomplete bleaching. OSL dating determines the time elapsed since mineral grains were last exposed to sunlight. For these sediment-laden, turbulent glaciolacustrine sediments deposited near ice fronts where the opportunity for exposure to sunlight is minimal, the last sunlight exposure may relate to a former depositional cycle, and so caused OSL age-overestimation in this context (Wallinga, 2002; Alexanderson and Murray, 2012; Johnsen et al., 2012).

In the RH valley, field mapping revealed a prominent flat bench running over several km on the southern valley slopes, perched at an elevation of ~790 m, and notched on the ice-proximal side of the innermost preserved RH terminal moraine (Figs. 6b and 4 c,d). This landform was interpreted as a palaeo-shoreline and was sampled for TCN dating using three polished granite surface cobbles. It indicates the formation of a separate, isolated proglacial lake in the RH valley, formed as the RH glacier retreated westward. The comparable elevation of shorelines in both RC and RH valleys suggests that the two proglacial lakes could have been connected following northward/westward retreat of both ice fronts beyond Corcovado (43°32′S, 71°27′W), and thus arguably experienced final lowering and shoreline abandonment synchronously. The main spillway draining the RH palaeolake towards the Atlantic occurs at 43°31′42″S, 71°13′26″W, where a central, 130 m-wide breach through the innermost RH moraine complex displays a basal elevation of 780 m (Fig. 6b).

After depositing the RC VI moraine, the RC glacier experienced another period of retreat prior to stabilising or re-advancing around 19.9 ± 1.1 ka, thus causing the formation of the innermost preserved LGM moraine (RC VII, Fig. 9e), which is located 3.5 km inboard and ~70 m lower than the RC VI moraine at the location of sampling (Figs. 2 and 7). The sampled RC VII moraine crest is only 20–30 m above the 790 m shoreline level, and geomorphological mapping indicates no preserved matching ridges further east towards the former RC frontal-terminal environment, suggesting that while the RC glacier front was grounded above water level at its western lateral margin, it may have been calving at its frontal margin toward the centre of the RC basin.

Our ages from the RC VI and RC VII moraines coincide with a fairly widespread glacial expansion event that occurred in numerous other Patagonian valleys at around 20–21 ka. Indeed, this expansion event was for instance recorded in the Strait of Magellan (52°S; outermost C limit, Kaplan et al., 2007, 2008), the Torres del Paine valley (51°S: TDP I moraine; García et al., 2018), the Lago General Carrera/Buenos Aires valley (46.5°S: Fenix I moraine, Kaplan et al., 2004; Douglass et al., 2006), and the Río Cisnes valley (44°S: CIS IV: García et al., 2019). A coeval event, locally named the *Otira 6* advance, was also found to occur in several New Zealand Southern-Alps valleys, with a reported mean age of ~20.5 ka (e.g. Shulmeister et al., 2019).

4.2.3. The onset of local deglaciation and proglacial lake phase three (Fig. 9f)

Bayesian age modelling suggests a mean age of 19.9 ± 1.1 ka for the RC VII advance/stillstand. As we did not find evidence for younger moraine deposits related to the RC glacier, we interpret this result as a maximum-limiting age for the onset of local deglaciation. However, our confidence in moraine-age interpretation is lower for RC VII than for other RC moraines due to its significantly higher degree of boulder exposure-age scatter (MSWD: 5.34, n = 3) and high number of proposed outliers (n = 3) (Table 2, Fig. 8), suggestive of substantial inheritance and/or post-depositional disturbance signals. The ridge is similar to the RC III-VI moraines in orientation (at the location of sampling: northwest-southeast), vertical relief, width-to-height ratio (7.4), slope gradients (Ice-P: 17° and Ice-D: 14°), and surface clast lithologies and shape (GR% = 56; C_{40}: 13.3, block-dominated) (Fig. 7). These geomorphological and sedimentological similarities support our interpretation of the ridge as a moraine formed by the RC

glacier. However, the RC VII moraine is distinctively less sharp-crested, and exhibits a flatter, wider and more subdued crest surface with little variation in crest-line elevation (Fig. 7). Contrary to the RC III-VI moraines, the RC VII moraine is not part of a complex displaying numerous superimposed recessional ridges, and only exhibits one, prominent but relatively subdued ridge. Surface clast analysis (Fig. 7) also reveals a higher proportion of angular-to-very-angular clasts than for other moraines (RA: 36.7). Given these geomorphological differences, one might argue that the RC VII moraine was either former under different conditions, or experienced more post-depositional disturbance.

One possible disturbance mechanism is the presence of a proglacial lake at ~790 m in the RC valley between ~21 and ~19 ka. Indeed, glacier-front recession from the grounded RC VII margin would likely have resulted in wave pounding of the RC VII moraine. This is supported by DEM cross-moraine elevation profiles (n = 7) drawn along the preserved moraine ridge, which display a notched platform, here interpreted as a palaeo-shoreline, on the ice-proximal moraine slope at the approximate elevation of 785–795 m (Fig. 7, red arrow). Wave pounding of the ice-proximal moraine slope may have destabilised the 20–30 m protruding moraine crest, causing lateral creep, and generating crest-surface lowering and flattening. Such disturbance may have caused subsequent moraine-boulder rotation and/or exhumation and enhance the potential for under-estimating exposure ages.

However, our chronological and stratigraphical interpretation suggests that outliers (n = 3) from the RC VII exposure-age population seem to be over-estimating ages suggestive of inheritance signals (Fig. 8). A more realistic potential source of age-scatter could be the contamination of the RC VII moraine by older, more ice-distal LGM deposits. Indeed, unsorted and unconsolidated lateral till deposits mantling steep valley slopes could fall as supraglacial debris onto glacier surfaces following ice-thinning from outermost LGM margins. This hypothesis would support the observed negative correlation between LGM moraine age and boulder age-scatter, but also the slightly higher angularity of RC VII surface clasts (Fig. 7).

The RC valley displays a second, easily discernible bench cutting through the entire north-to-south extent (over 15 km) of the eastern hillside (slope 16-19°) at an elevation of ~680 m (Figs. 4a and 6c). We interpreted this as a wave-cut proglacial lake shoreline, and it was sampled for TCN dating using polished granite surface cobbles (Table 2; Fig. 6c). Twenty-seven cross-section elevation profiles were drawn across the platform from DEM in locations exhibiting a preserved terrace. They revealed a mean maximum shoreline excavation of ~6 m. This shoreline roughly matches (within ~10 m) the elevations of numerous other shorelines, raised deltas and raised outwash deposits located in the RC, RH, RF and RP valleys (Supplementary materials). Such geomorphic evidence indicates the formation of a third proglacial lake phase, diagnosed by a geographically widespread proglacial lake eventually connecting all valleys of the studied region. This is further evidenced by field observations of uppermost (below soil) units of fine, sand to clay-sized and occasionally laminated, varved sediments exposed at numerous road-cut sections across the RC, RP and RF valley floors (Supplementary materials). We sampled one of these road-cut exposures located near the RC valley floor, at an elevation of 544 m (43°41′50,3″S, 71°24′22,4″W), and composed of laminated and varved clay-to-silt sized sediments, for OSL dating. The sample yielded a burial age of 65.4 ± 7.1 ka. Following the same reasoning described above (5.2.2), we consider this age to be significantly older than the deposition of these sediments.

The third glaciolacustrine phase is inferred to have started with the abandonment of the RH_{790} shoreline at 19.0 ± 0.9 ka (Table 2, Fig. 8), when the lake-level dropped from ~790 m to ~680 m (Fig. 9f). We suggest that this ~100 m lake lowering reflects the continued retreat of the RC, RH and RF ice-fronts into the RP valley. We hypothesise that once the ice front retreated westward beyond Corcovado (Fig. 9f), such retreat enabled northward drainage of the palaeolake through the RF valley, which also contains preserved palaeo-shorelines and raised deltas at ~680 m (Supplementary materials). However, the lowest potential spillway towards the northeast today lies at approximately 750 m, about 70 m higher than the palaeolake elevation. We hypothesise that this drainage elevation mismatch can be attributed to the post-glacial accretion of a large (~5 km^2) arcuate alluvial fan into a narrow col located between the RF and Lago Rosario basins (43°17′S; 71°24′W; see supplementary materials). The RF spillway would enable waters to drain towards contemporary Lago Rosario. We thus propose, during glaciolacustrine phase three, a complex network of connected palaeolakes enabling meltwater drainage from the former RC, RH and RF-connected lake (~680 m) into the current Lago Rosario (665 m), and into a former proglacial lake occupying the Trevelin basin to the north (~650 m; Andrada de Palomera, 2002; Martínez et al., 2011), which eventually spilled eastward towards Río Tecka and the Atlantic Ocean (proposed spillway: 43°05′57″S, 71°02′48″W).

Overall, if assuming the former ice-sheet divide was located near Macizo Nevado (Fig. 1c), our reconstruction thus suggests that by ~19 ka, the RC glacier had experienced ~30 km of retreat from its innermost RC VII margin, representing a ~40 km retreat and ~40% glacier-length loss relative to its full local LGM extent (RC III). We thereby interpret the age of 19.0 ± 0.9 ka as a minimum-limiting age for the onset of significant local deglaciation.

For several other glaciated regions of Patagonia, a predominant late-LGM event of PIS expansion and/or stabilisation was reported at around 17–18 ka, towards the onset of Heinrich Stadial 1 (Hemming, 2004). Glacier advance/stillstands around this time were reported, for instance, for the Magellan outlet glacier (innermost C limit, Kaplan et al., 2007, 2008), the Río Guanaco glacier (49°S: La Sofia and San Jorge moraines: Murray et al., 2012), the Lago Belgrano glacier (47°S: Menelik innermost moraine: Mendelová et al., 2020a) and several glaciers of the Chilean lake district (Moreno et al., 2015) (Supplementary materials). Such event coincides furthermore with the widespread *Otira 7* signal of glacial advance in New Zealand (Shulmeister et al., 2019). However, our chronological reconstruction shows no evidence of advances/stillstands of the RC glacier younger than 19.9 ± 1.1 ka. A similar lack of late-LGM PIS expansion signal was reported for the Río Cisnes outlet glacier 90 km to the south of our field site (García et al., 2019). The available evidence thus argues deglaciation of main PIS outlets initiated somewhat earlier in northeastern Patagonia, as any possible readvance of the RC glacier during the late-LGM was not recorded in the geomorpholgocial record. This is further supported by new glacial geochronological TCN dating results suggesting that subsequent glacier advances/still-stands in the region were restricted to local mountain glaciers (Leger et al., 2021).

4.2.4. The timing of ice-sheet disintegration and Atlantic/Pacific drainage reversal (Fig. 9G, H)

Our TCN dating of ice-moulded bedrock surfaces from the RP valley (Fig. 5) suggests that by 16.3 ± 0.3 ka, the Palena ice-stream had retreated at least towards the foothills of Macizo Nevado (Figs. 1 and 9g,h), west of 72°W, facilitating final drainage of the ice-dammed ~680 m proglacial lake beneath or between shrinking mountain ice caps. The opening of a westward drainage route represents an Atlantic to Pacific drainage reversal (Fig. 9h) and a 70 km shift in the drainage divide, which is common to other over-deepened eastern Patagonian valleys (Glasser et al., 2016; Thorndycraft et al., 2019). Since the bedrock surfaces sampled are

elevated at 343 m and 254 m a.s.l., the >340 m deep-water overburden during proglacial lake phase three would have been sufficient to reduce ^{10}Be muonogenic and spallation production by >99.9%. We thus argue that the mean exposure age of 16.3 ± 0.3 ka is representative of the approximate timing of local Atlantic/Pacific drainage reversal, and marks the end of glaciolacustrine phase three. We thereby propose that the extensive ~680 m proglacial lake existed for 2.5 to 3 ka, between ~19 ka and ~16 ka. The former maximum lake area and volume may have been as much as ~950 km^2 and ~273 km^3 for this third phase, although these estimates yield significant uncertainties as they were computed (from DEM) using a hypothetical ice-dam location near the foothills of Macizo Nevado (Fig. 9g). The timing of lake drainage is further evidenced by the age proximity of the three surface cobbles sampled from the RC_{680} palaeo-shoreline, which suggest a mean exposure age of 16.3 ± 0.8 ka, here interpreted as the onset of the ~680 m proglacial lake drainage and lowering. Our present reconstruction does not allow us to distinguish whether the final Pacific-directed drainage was a progressive or relatively sudden event, nor whether drainage was directed towards Lago Yelcho (Northwest), or Río Palena (Southwest). To resolve this will require further geomorphological investigations.

The PIS recession associated with ice-sheet disintegration and Atlantic/Pacific drainage reversal represents ~70 km of total ice-front retreat from innermost LGM position associated with the RC VII moraine (Fig. 9). These results suggest an approximate mean retreat rate of 14 m yr^{-1} between 19.9 ± 1.1 ka and 16.3 ± 0.3 ka (1σ range: 9–36 m yr^{-1}). Such rates are comparable to deglacial retreat rates proposed for other eastern PIS outlet glaciers (e.g., Bendle et al., 2017a: 15.4–18.0 m yr^{-1}). We thus argue that by ~16–16.5 ka, the northeastern PIS (43°S) started disintegrating into separate ice caps and mountain glaciers constrained to higher topography (Fig. 9h).

4.3. Palaeoclimate

4.3.1. The timing of local LGM expansions

Our geomorphological and geochronological reconstruction suggests that the timing of PIS LGM expansion in northeastern Patagonia is broadly coeval with the expansion of northern hemispheric ice sheets, a minimum in northern hemispheric atmospheric temperatures (e.g., NGRIP Members, 2004) and a minimum in summer insolation intensity at 60° N (Berger and Loutre, 1991). On the other hand, southern hemispheric summer insolation intensity at 44° S was increasing during the global LGM, reaching a maximum at ~21.5 ka, and was thus out of phase with local glacier expansion (Berger and Loutre, 1991; Doughty et al., 2015, Fig. 10). The timing of the RC LGM advances/stillstands is however synchronous with a decrease in southern winter insolation intensity at 40° S, which reached a minimum at ~19.5 ka, causing increased seasonality and local winter duration during PIS LGM expansions (Darvill et al., 2016; Denton et al., 2021, Fig. 10).

Furthermore, we observe a good agreement between the timing of RC glacier LGM advances/stillstands and atmospheric cooling over west Antarctica, according to $\delta^{18}O$ data from the West Antarctic Ice Sheet (WAIS) Divide Ice Core (WDC; 79°S; WAIS Divide Project Members, 2013, 2015, Fig. 10). Indeed, major $\delta^{18}O$ minima diagnostic of atmospheric cooling over West Antarctica during MIS 2 occurred at ~28.5, ~27.4, ~25.7, ~22, ~21.2 and ~20.0 ka. Ages from the RC moraines broadly match those minima. The most potent of these West Antarctic cooling events seems to have occurred at ~25.7 ka, which coincides approximately with the timing of the outermost RC III advance (26.4 ± 1.4 ka) (Fig. 10). Moreover, the 3–4 ka gap separating the ages of the RC III (~26.4 ka) and RC IV (~22.4 ka) moraines coincides with a 2 ka, slight atmospheric warming signal in the WDC record evidenced by a ~2‰ increase in $\delta^{18}O$ (between 25.9 and 23.8 ka; *ibid*). Individual RC advances also match maxima in WDC sea-salt sodium concentration record, a local sea-ice expansion/contraction proxy for West Antarctica (Fig. 10).

Oceanic conditions in the southeast Pacific and near Patagonia (south of the Subtropical Front) have been inferred from the MD07-3128 (53°S; Caniupán et al., 2011) and ODP-1233 (41°S; Kaiser et al., 2007) ocean sediment core records (Fig. 10g–j). Local sea surface temperature (SST) proxy data from both records indicate sea-surface cooling of between 5 and 6 °C relative to today during the global LGM (Kaiser et al., 2005, 2007) and consistent with a minimum in northern hemispheric summer insolation intensity (Fig. 10). Furthermore, they demonstrate millennial-scale SST fluctuations broadly consistent with atmospheric temperature variations over west Antarctica and with PIS expansions during the global LGM, although the resolution of those SST LGM records is often too poor to correlate confidently millennial-scale fluctuations between records. Other investigations (e.g., Doughty et al., 2015; Shulmeister et al., 2019; Strand et al., 2019) reconstructing New Zealand LGM glacier advances and local millennial-scale climate variability further support synchronicity between local SST lowering, Antarctic atmospheric cooling, and glacier expansion at the southern middle latitudes during the global LGM, despite out-of-phase local summer insolation intensity.

Consequently, our data support the hypothesis of a synchronous southern hemispheric glacial response to major fluctuations in northern hemispheric insolation intensity, and bolster the hypothesis that a MIS 2 oceanic and atmospheric cooling signal propagated from the northern to the southern hemisphere (Broecker, 1998; Doughty et al., 2015; Buizert et al., 2018). However, we note that our data could also support the new *Zealandia Switch* hypothesis proposed by Denton et al. (2021). This hypothesis instead argues that insolation-induced variations in the position and strength of the SWW and their impact on the tropical/subtropical ocean could be the main driver for millennial-scale climate variations in the Southern Hemisphere during the last glacial cycle.

Atmospheric conditions over West Antarctica are thought to be strongly influenced by the strength and position of the ACC, which is mostly controlled by the position of the SWW (Rignot et al., 2019). It has moreover been argued that colder intervals in the southern mid-latitudes are linked to a northward migration and strength reduction of the SWW, which would increase precipitation delivery over northern Patagonia, promote local glacier expansion, and lead to a weakening of the ACC through the Drake Passage (Lamy et al., 2015; Lamy et al., 2004). In turn, this would cause the Subtropical Frontal zone to migrate northward and promote Antarctic sea-ice build-up, generating colder conditions over West Antarctica (Pedro et al., 2018). The near-synchronicity of West Antarctic sea ice build-up with minima in WDC atmospheric palaeo-temperatures, and thus with northeastern Patagonian glacier advances, as revealed by the WDC sea-salt sodium record (WAIS Divide Project Members, 2013, 2015, Fig. 10), supports this mechanism.

$\delta^{13}C$ data from Hollywood Cave (42.5°S), South Island, New Zealand, are used as a local proxy record of palaeo-precipitation and SWW intensity (Whittaker et al., 2011, Fig. 10). During the global LGM, this dataset demonstrates significant levels of precipitation variability, with wetter episodes between 30.3 and 27.1 ka, but also around ~24.6 ka and ~22.3 ka (Fig. 10). This data does not demonstrate a systematic positive correlation between precipitation over New Zealand at 42.5°S and LGM advances of the RC glacier, although some precipitation maxima overlap with RC moraine ages (e.g. RC IV, V, and VII). Palaeo-ecological reconstructions from the Chilean Lake District (41°S; Moreno et al., 2015, 2018) also suggest an increased SWW influence and wetter

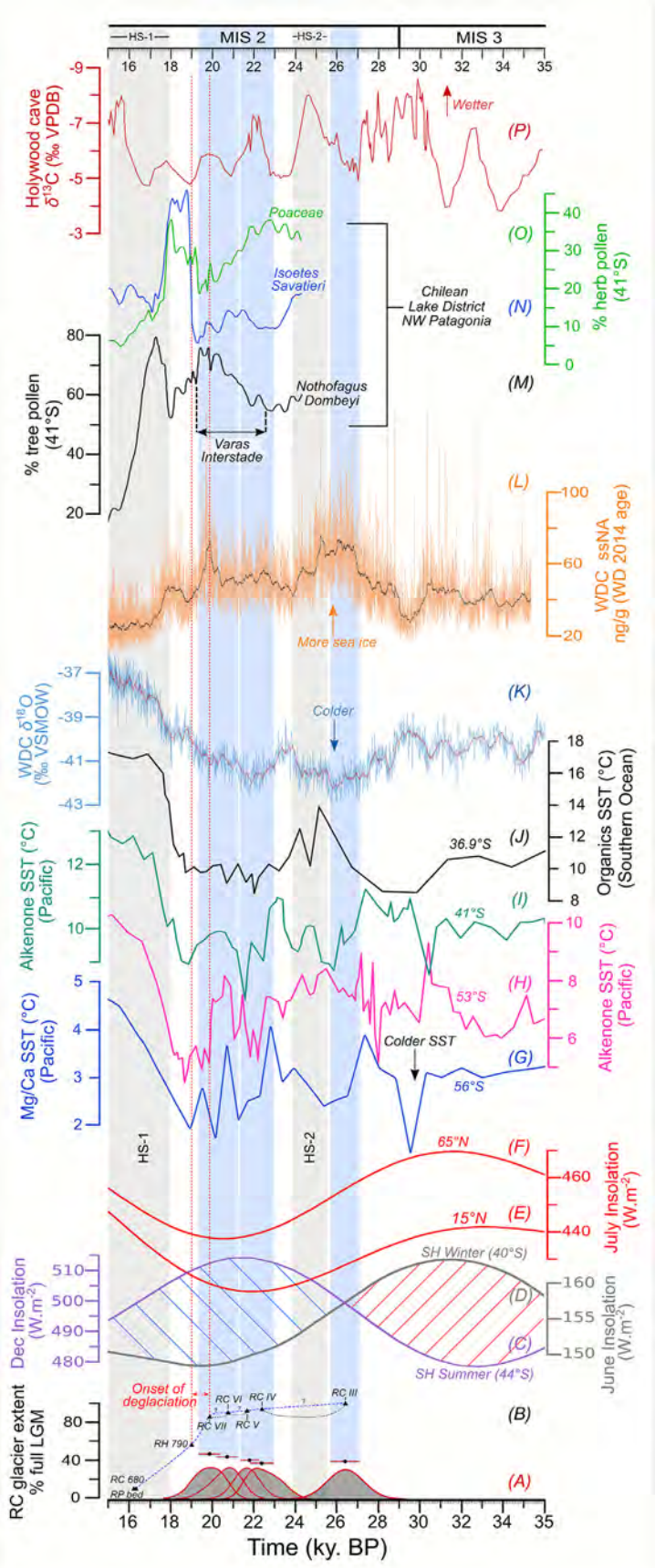
HS-1
MIS 2
HS-2
MIS 3
Holywood cave δ13C (‰ VPDB)
Wetter
(P)
Poaceae
Isoetes Savatieri
(O)
(N)
Chilean Lake District NW Patagonia
% herb pollen (41°S)
% tree pollen (41°S)
Nothofagus Dombeyi
Varas Interstade
(M)
(L)
WDC ssNA ng/g (WD 2014 age)
More sea ice
WDC δ18O (‰ VSMOW)
Colder
(K)
Organics SST (°C) (Southern Ocean)
36.9°S
(J)
Alkenone SST (°C) (Pacific)
41°S
(I)
53°S
(H)
Colder SST
56°S
(G)
Mg/Ca SST (°C) (Pacific)
HS-1
HS-2
65°N
(F)
15°N
(E)
July Insolation (W.m-2)
SH Winter (40°S)
Dec Insolation (W.m-2)
(D)
(C)
SH Summer (44°S)
June Insolation (W.m-2)
Onset of deglaciation
RC VI
RC IV
RC III
RC VII
RC V
RH 790
RC 680
RP bed
(B)
(A)
RC glacier extent % full LGM
Time (ky. BP)

conditions in northwestern Patagonia between 25 ka and 17.8 ka BP, with a slight warming and drying during the Varas interstade (22–19.2 ka BP). These data also suggest a precipitation decline along with rapid warming between 17.8 and 14.8 ka BP, likely associated with a poleward shift in the SWW belt (Moreno et al., 2018). These data thus support the proposed equatorward migration of the SWW belt during the LGM. Since northeastern PIS outlet glaciers were located toward the northern edge of the wind belt, one could argue that they would have been sensitive to fluctuations in precipitation delivery forced by latitudinal migrations of the SWW (Davies et al., 2020). Therefore, along with decreasing atmospheric temperatures, periodic northward migrations of the SWW may have also played a role in controlling the timing of individual LGM advances of northeastern PIS outlet glaciers.

However, there is a dearth of MIS 2 palaeo-precipitation records from northeastern Patagonia and records from the Chilean Lake District (Moreno et al., 2015, 2018) may not necessarily be representative of LGM precipitation east of the Patagonian Andes. Recent climate modelling studies (Fogwill et al., 2015; Berman et al., 2016) and empirical data (Van Daele et al., 2016) have instead been used to argue that despite a northward migration of the SWW belt, the enhanced orographic effect of the PIS-covered Andes may have caused up to 50% drier-than-present conditions to the east of the former ice divide throughout the global LGM. Therefore, assessing the former role of precipitation in promoting PIS outlet glacier expansion during the global LGM in northeastern Patagonia remains a challenge.

4.3.2. The onset of local deglaciation

Patagonian palaeoglacial records seem to indicate an asynchronous deglacial response of major PIS outlet glaciers during the Last Glacial Termination (e.g., Kaplan et al., 2008; Hein et al., 2010; Moreno et al., 2015; Bendle et al., 2017a; García et al., 2019). With the onset of ice recession from LGM margins appearing to be glacier-specific, and to vary between 19 and 20 ka in northeastern Patagonia and 17–18 ka in northwestern, central and southern Patagonia (Supplementary Figure 2). However, most records seem to agree on a rapid, extensive retreat of outlet glaciers towards the mountain front occurring prior to ~16 ka, leading to the establishment of warm, near-Holocene conditions by ~15 ka (e.g., Hein et al., 2010; Boex et al., 2013; García et al., 2019; Davies et al., 2020).

The Patagonian asynchronous deglacial response has been addressed by several studies (e.g. Bendle et al., 2017a; García et al., 2019). García et al. (2019) highlight an early atmospheric and oceanic warming signal arguably widespread throughout the southern mid-to-high latitudes and beginning at around 20–22 ka. The occurrence of this warming is supported by numerous local palaeoclimate records including pollen records from the Chilean Lake District; which indicate a sharp increase in *Nothofagus Dombeyi* arboreal pollen percentage values from ~21.8 ka and peaking at ~19.5 ka (Denton et al., 1999; Moreno et al., 2015, 2018, Fig. 10m). This increase in glacial arboreal populations was interpreted as a shift in the regional treeline resulting from increasing air temperatures (Moreno et al., 2018). This relatively warm and drier late-LGM interval, termed the Varas interstade in northwestern Patagonia (Denton et al., 1999; Mercer, 1972), is argued to have started at around 22.6 kcal yrs BP and peaked at 19.3 kcal yrs BP. This event preceded a return to colder, wetter conditions between 19.3 and 17.8 kcal yrs BP, as demonstrated by sharp positive anomalies in *Poaceae* and *Isoetes savatieri* pollen concentrations at Lago Pichilaguna (41°15′S; 73°3′W; Moreno et al., 2018, Fig. 10o,p). Southeast Pacific Sea Surface Temperature (SST) records from 56°S (Mashiotta et al., 1999), 53°S (Caniupán et al., 2011) and 41°S (Kaiser et al., 2007) all indicate a 2–3 °C SST warming signal starting between 21.5 and 22 ka and reaching a maximum at ~20.5 ka prior to renewed cooling, thus indicating a local SST increase approximately coeval with the Varas interstade. A similar pattern of SST increase was recorded in the southern Atlantic (41.1°S; Barker et al., 2009). In West-Antarctica, $\delta^{18}O$ data from the WDC ice core (79°S) suggest local air temperatures reached a minimum at ~21.8 ka, and demonstrate a ~2.5 °C warming until ~18.6 ka, marking the onset of a slight renewed cooling until 17.9 ka, a time of local deglacial warming (WAIS Divide Project Members, 2015, Fig. 10). Antarctic sea-ice extent proxy data from the southeast Pacific (WAIS Divide Project Members, 2015) and the Scotia Sea (Collins et al., 2012) both suggest a coinciding sea-ice decline starting at 20 ka and 22 ka, respectively, prior to a brief period of build-up between 18.7 and 17.9 ka. Allen et al. (2011) provide further evidence that while winter sea-ice extent did not recede until ~19 ka in the Scotia Sea, summer sea ice retreated to south of 61°S by ~22 ka, which suggests a local pattern of seasonally ice-free waters during the Varas interstade. Therefore, as previously argued by García et al. (2019), we propose that local coupled atmospheric and oceanic warming between ~22.5 and ~19.5 ka might have caused some sensitive Patagonian glaciers to experience early destabilisation and recession (19–20 ka; e.g. RC glacier, Río Cisnes glacier, Lago Cochrane/Pueyrredón glacier). The RC moraine record presented here thus provides further evidence that PIS outlet glaciers in northeastern Patagonia experienced relatively early recession from their LGM margins. However, subsequent cooling and northward migration of the SWW leading to wetter conditions between ~19.5 and ~18 ka (Moreno et al., 2018) caused certain PIS outlets to stabilise and/or re-advance towards LGM margins, such as observed in the Chilean Lake District (e.g. Llanquihue glacier; Denton et al., 1999; Moreno et al., 2015). Similarly to the Río Cisnes glacier (García et al., 2019), our investigation provides no evidence of a pronounced re-advance of the RC glacier between ~19.5 and ~18 ka. Our chronology suggests instead that the RC glacier had experienced significant retreat (at least ~40% glacier-length loss relative to its full LGM extent) by ~19 ka. This could indicate a local east/west asymmetry whereby northeastern PIS outlets glaciers were more sensitive to warming during the Varas interstade than glaciers of the wetter, western side of the Andes, and thus experienced a more negative mass balance. Conversely, western PIS outlets in northern Patagonia were perhaps more sensitive and responsive to a late-LGM cooling and wetting between ~19.5 and ~18 ka. The

Fig. 10. Vertical plot comparing our RC III - RC VII ^{10}Be chronology with other palaeoclimate proxy records. (**A**): 1σ probability density distributions, arithmetic means (black dots) and standard deviation (error bars) from Bayesian age model outputs for the RC III – RC VII moraines. (**B**): Reconstructed, approximate percentage extent of the RC glacier relative to full LGM extent (RC III) for each glacial and deglacial event dated in this study. Blue dashed lines represent a scenario of linear ice-front retreat and stillstands while black dashed lines represent potential scenarios of RC ice-front retreat and re-advance (**C**–**F**): Insolation intensity for (**C**) 44°S, December; (**D**) 40°S, June; (**E**) 15°N, July; and (**F**) 65°N, July (Berger and Loutre, 1991). Hatching in between the southern summer and winter insolation curves highlights periods of high (blue) and low (red) seasonality (**G**): Sub-antarctic SST (*Mg/Ca*) record from the southern Pacific Ocean, 56°S (core E11-2; Mashiotta et al., 1999). (**H**): Alkenone SST record from the Southeast Pacific (Chilean coast), 53°S (core MD07-3128; Canupian et al., 2011). (**I**) Alkenone SST record from the Southeast Pacific (Chilean coast), 41°S (core ODP-1233; Kaiser et al., 2007). (**J**) Organics SST (TEXH 86) from the Southern Ocean (southern Australian coast), 36.9°S (core MD03-2607; Lopes dos Santos et al., 2013). (**K**): $\delta^{18}O$ record (‰ Vienna Standard Mean Ocean Water scale) from the WDC Antarctic ice core (WAIS Divide Project Members, 2013, 2015) displayed with a 12-point moving average. (**L**) Sea-salt sodium data (ss*Na*; ng/g) from the WDC Antarctic ice core, interpreted as a proxy for regional sea-ice production (*ibid*). (**M-O**): Weighted moving average of (**M**) *Nothofagus Dombeyi*, (**N**) *Isoetes Savatieri*, and (**O**) *Poaceae* pollen-type concentration (%) from the Lago Pichilaguna record (41°S; Moreno et al., 2018). (**P**) $\delta^{13}C$ data from a speleothem record located at Hollywood Cave (42.5°S; Whittaker et al., 2011), South Island, New Zealand interpreted as a local palaeo-precipitation and SWW intensity record.

proposed increase in west-to-east precipitation starvation over the Patagonian Andes during the LGM (Berman et al., 2016; Van Daele et al., 2016) could help to explain the higher sensitivity of drier, northeastern Patagonian glaciers to such atmospheric warming, as well as a lack of outlet glacier response to increased moisture delivery between ~19.5 and ~18 ka. Moreover, the formation of large ice-dammed proglacial lakes during PIS recession is much more common to the east than to the west of the Patagonian Andes, due to the westward−sloping glacially over-deepened nature of the region's main valley troughs. Recent glaciological observations (Jackson et al., 2020) and modelling work conducted on temperate mid-latitude mountain glaciers has shown that under identical climate forcing, glaciers calving into proglacial lakes were likely to experience up to four times more extensive and up to eight times faster ice-front retreat than a land-terminating glacier (Sutherland et al., 2020). In the RC valley, the formation of glaciolacustrine phase two (between ~20.7 and ~21.7), added to slightly warmer and drier conditions during the Varas interstade (22.6−19.3), may have caused enhanced ablation and extensive, rapid retreat of the ice-front and a lower sensitivity to subsequent cooling and wetting between ~19.5 and ~18 ka. Such glaciolacustrine climate-decoupling mechanism of major eastern PIS outlets has been proposed for several valleys of central Patagonia (e.g. Mendelová et al., 2017).

On the other hand, ocean sediment cores from the southern coasts of New Zealand and Australia exhibit little evidence of SST increases prior to 18−19 ka (Pahnke et al., 2003; Barrows et al., 2007; Lopes dos Santos et al., 2013). Similarly, $\delta^{18}O$ data from the EPICA Dome C and Dronning Maud Land (EPICA Community Members, 2006), Dome Fuji (Kawamura et al., 2007) and Talos Dome (Stenni et al., 2011) ice cores do not display clear evidence of sustained atmospheric warming over East-Antarctica between 22 and 18 ka. In the New Zealand Alps, the onset of glacial termination causing rapid ice-front retreat is agued to have occurred around the early stages of Heinrich Stadial 1, shortly after ~18 ka (Shulmeister et al., 2010; Putnam et al., 2013; Kelley et al., 2014; Doughty et al., 2015), while little to no evidence of prior late-LGM warming and significant glacier retreat was found. These data suggest that the early oceanic and atmospheric warming signal beginning at 20−22 ka was perhaps not widespread throughout the southern mid-to-high latitudes, but was possibly more confined to West Antarctica, Patagonia, and local ocean basins.

5. Conclusions

- The Río Corcovado Last Glacial Maximum (LGM) moraine record displays at least five (RC III-VII) distinct advances/stillstands of the Río Corcovado glacier. Our results from ^{10}Be terrestrial cosmogenic nuclide dating of moraine boulders suggest that these major advances/stillstands occurred over a 6−7 ka period, at 26.4 ± 1.4 ka, 22.4 ± 1.15 ka, 21.7 ± 0.9 ka, 20.7 ± 1.0 ka and 19.9 ± 1.1 ka, thereby during the global LGM. These glacial expansion events are coeval with a decline and minimum in northern hemispheric insolation intensity, atmospheric cooling over Antarctica, and lowering of sea-surface temperatures in mid-latitude southern ocean basins, thus supporting the hypothesis of a Marine Isotope Stage 2 oceanic and atmospheric cooling signal propagated from the northern to the southern hemisphere.
- Our geochronological reconstruction of the Río Corcovado glacier advances/stillstands provides no evidence for Marine Isotope Stage 3 advances more extensive than those that occurred during the global LGM in this area. Therefore, our results support the idea of large latitudinal and longitudinal disparities across Patagonia in the timing and magnitude of maximum glaciation during the last glacial cycle.
- The oldest LGM advance recorded in the Río Corcovado valley is associated with the formation of the first of three glaciolacustrine phases, dated to 26.4 ± 1.4 ka, and characterised by a surface lake level of ~990 m a.s.l. Gradual glacier retreat from late-LGM margins led to the formation of a second glaciolacustrine phase, formed between ~20.5 and ~22 ka, with the proglacial-lake surface at an elevation of ~790 m a.s.l. for 1.5 to 2.5 ka.
- The onset of local deglaciation and Río Corcovado glacier retreat from LGM margins occurred between 19 and 20 ka. Our chronology thus supports an early deglaciation scenario for outlet glaciers of northeastern Patagonia relative to northwestern and southern Patagonia, which may indicate a high local glacier sensitivity to atmospheric warming and drying during the Varas interstade (~19.5−22.5 ka), and/or to the enhanced ablation effect of large proglacial lake formation.
- At around 19.0 ± 0.9 ka, further ice-front retreat into the Río Palena valley precipitated a third and last glaciolacustrine phase associated with a new proglacial-lake spillway opened into the north Río Frio valley, causing a lake-level drop from ~790 a.s.l. m to ~680 m a.s.l. We propose that this extensive ~680 m a.s.l. proglacial lake existed for 2.5 to 3 ka, between ~16 and ~19 ka.
- By ~16 ka, the Palena ice front had retreated westwards by at least ~70 km, towards the mountain front interior, leading to local Patagonian Ice Sheet disintegration and the final westward, Pacific-directed drainage of glaciolacustrine phase three, dated to 16.3 ± 0.3 ka. We interpret this age as the approximate timing of local Atlantic/Pacific drainage reversal, which caused an estimated ~270 km^3 of freshwater to drain, either progressively or suddenly, into the Pacific Ocean and the Golfo Corcovado.

Funding

This investigation is part of a University of Edinburgh E^3 Doctoral Training Partnership Ph.D. studentship (award code: NE/L002558/1) awarded by the National Environment Research Council (NERC) to TPML. Our second field expedition (01/02 2020) was supported by a crowd-funding campaign through the Crowd. Science fundraising platform (https://crowd.science) and a British Society for Geomorphology Postgraduate Research Grant award (BSG-2019-04) awarded to TPML. TCN dating laboratory analysis and AMS measurements were funded by a NERC Cosmogenic Isotope Analysis Facility (CIAF) grant (9196−0419) awarded to ASH and TPML in June 2019.

Declaration of competing interest

The authors declare that they have no known competing financial interests or personal relationships that could have appeared to influence the work reported in this paper.

Acknowledgments

We wish to express our sincere gratitude towards all individuals who contributed to the https://crowd.science/crowdfunding campaign enabling a 2020 field trip to our study site. We also thank the local landowners who authorized access and work on their property, in particular, the Estancia Tecka (Chubut, Argentina) for enabling access to their land and private roads. Moreover, we are grateful to Dr. Robert McCulloch, Dr. Juan Luis García, Pablo Tapia

Gonzalez, Dr. Oscar Martínez, María Paz Lira-Bahamonde and Dr. Rodrigo Soteres for help and logistical support with the overall project and in the field. We also wish to thank Dr Mateo A. Martini for his insightful discussions in the field and precious comments on the final manuscript, as well as Mr. Allan Davidson for his precious work and supervision on sample quartz isolation and purification at SUERC. Finally, we thank the two anonymous reviewers for their thoughtful comments allowing us to improve the quality of the manuscript.

Credit author statement

Tancrède P. M. Leger: Conceptualization, Data curation, Formal analysis, Funding acquisition, Investigation, Methodology, Project administration, Software, Visualization, Writing (original draft and review & editing). Andrew S. Hein: Conceptualization, Data curation, Funding acquisition, Methodology, Project administration, Supervision, Validation, Writing (original draft and review & editing). Robert M. Bingham: Data curation, Supervision, Writing (original draft and review & editing). Ángel Rodés: Data curation, Methodology, Writing (original draft). Derek Fabel: Data curation, Writing (original draft), Rachel K. Smedley: Data curation, Writing (original draft)

Appendix A. Supplementary data

Supplementary data to this article can be found online at https://doi.org/10.1016/j.quascirev.2021.107194.

References

Alexanderson, H., Murray, A.S., 2012. Problems and potential of OSL dating Weichselian and Holocene sediments in Sweden. Quat. Sci. Rev. 44, 37–50. https://doi.org/10.1016/j.quascirev.2009.09.020.

Allen, C.S., Pike, J., Pudsey, C.J., 2011. Last glacial–interglacial sea-ice cover in the SW Atlantic and its potential role in global deglaciation. Quat. Sci. Rev. 30 (19–20), 2446–2458. https://doi.org/10.1016/j.quascirev.2011.04.002.

Andrada de Palomera, R.P., 2002. Geomorfología del valle de Esquel y alrededores de las lagunas Willimanco, Zeta y Carao, noroeste del Chubut. Actas del XV Congreso Geológico Argentino El Calafate. CD-ROM. Artículo No. 052, 6pp.

Applegate, P.J., Urban, N.M., Laabs, B.J.C., Keller, K., Alley, R.B., 2010. Modelling the statistical distributions of cosmogenic exposure dates from moraines. Geosci. Model Dev. (GMD) 3 (1), 293. https://doi.org/10.5194/gmd-3-293-2010.

Aravena, J.C., Luckman, B.H., 2009. Spatio-temporal rainfall patterns in southern South America. Int. J. Climatol.: A Journal of the Royal Meteorological Society 29 (14), 2106–2120. https://doi.org/10.1002/joc.1761.

Balco, G., Stone, J.O., Lifton, N.A., Dunai, T.J., 2008. A complete and easily accessible means of calculating surface exposure ages or erosion rates from 10Be and 26Al measurements. Quat. Geochronol. 3 (3), 174–195. https://doi.org/10.1016/j.quageo.2007.12.001.

Barker, S., Diz, P., Vautravers, M.J., Pike, J., Knorr, G., Hall, I.R., Broecker, W.S., 2009. Interhemispheric Atlantic seesaw response during the last deglaciation. Nature 457 (7233), 1097–1102. https://doi.org/10.1038/nature07770.

Barrows, T.T., Juggins, S., De Deckker, P., Calvo, E., Pelejero, C., 2007. Long-term sea surface temperature and climate change in the Australian–New Zealand region. Paleoceanography 22 (2). https://doi.org/10.1029/2006PA001328.

Bell, C.M., 2008. Punctuated drainage of an ice-dammed Quaternary lake in southern South America. Geogr. Ann. Phys. Geogr. 90 (1), 1–17. https://doi.org/10.1111/j.1468-0459.2008.00330.x.

Bendle, J.M., Palmer, A.P., Thorndycraft, V.R., Matthews, I.P., 2017 A. High-resolution chronology for deglaciation of the patagonian ice sheet at Lago Buenos Aires (46.5 S) revealed through varve chronology and Bayesian age modelling. Quat. Sci. Rev. 177, 314–339. https://doi.org/10.1016/j.quascirev.2017.10.013.

Bendle, J.M., Thorndycraft, V.R., Palmer, A.P., 2017 B. The glacial geomorphology of the Lago Buenos Aires and Lago Pueyrredón ice lobes of central patagonia. J. Maps 13 (2), 654–673. https://doi.org/10.1080/17445647.2017.1351908.

Benn, D.I., Ballantyne, C.K., 1993. The description and representation of particle shape. Earth Surf. Process. Landforms 18 (7), 665–672. https://doi.org/10.1093/oxfordjournals.humrep.a137463.

Berger, A., Loutre, M.F., 1991. Insolation values for the climate of the last 10 million years. Quat. Sci. Rev. 10 (4), 297–317.

Berman, A.L., Silvestri, G.E., Tonello, M.S., 2016. Differences between last glacial maximum and present-day temperature and precipitation in southern South America. Quat. Sci. Rev. 150, 221–233. https://doi.org/10.1016/j.quascirev.2016.08.025.

Boex, J., Fogwill, C., Harrison, S., Glasser, N.F., Hein, A., Schnabel, C., Xu, S., 2013. Rapid thinning of the late pleistocene patagonian ice sheet followed migration of the southern westerlies. Sci. Rep. 3, 2118. https://doi.org/10.1038/srep02118.

Borchers, B., Marrero, S., Balco, G., Caffee, M., Goehring, B., Lifton, N., Nishiizumi, K., Phillips, F., Schaefer, J., Stone, J., 2016. Geological calibration of spallation production rates in the CRONUS-Earth project. Quat. Geochronol. 31, 188–198. https://doi.org/10.1016/j.quageo.2015.01.009.

Broecker, W.S., 1998. Paleocean circulation during the last deglaciation: a bipolar seesaw? Paleoceanography 13 (2), 119–121. https://doi.org/10.1029/97PA03707.

Bronk Ramsey, C., 2008. Deposition models for chronological records. Quat. Sci. Rev. 27 (1–2), 42–60. https://doi.org/10.1016/j.quascirev.2007.01.019.

Bronk Ramsey, C., 2017. OxCal 4.3. https://c14.arch.ox.ac.uk/oxcal/OxCal.html.

Buizert, C., Sigl, M., Severi, M., Markle, B.R., Wettstein, J.J., McConnell, J.R., Pedro, J.B., Sodemann, H., Goto-Azuma, K., Kawamura, K., Fujita, S., Motoyama, H., Hirabayashi, M., Uemura, R., Stenni, B., Parrenin, F., Ha, F., Fudge, T.J., Steig, E.J., 2018. Abrupt ice-age shifts in southern westerly winds and Antarctic climate forced from the north. Nature 563 (7733), 681–685. https://doi.org/10.1130/G36477.1.

Caldenius, C.C.Z., 1932. Las glaciaciones cuaternarias en la patagonia y tierra del fuego. Geogr. Ann. 14, 1–164. https://doi.org/10.1080/20014422.1932.11880545.

Caniupán, M., Lamy, F., Lange, C.B., Kaiser, J., Arz, H., Kilian, R., Baeza Urrea, O., Aracena, C., Hebbeln, D., Kissel, C., Laj, C., Mollenhauer, G., Tiedemann, R., 2011. Millennial-scale sea surface temperature and Patagonian Ice Sheet changes off southernmost Chile (53 S) over the past~ 60 kyr. Paleoceanography 26 (3). https://doi.org/10.1029/2010PA002049.

Carter, L., McCave, I.N., Williams, M.J.M., 2008. Circulation and water masses of the Southern Ocean: a review. In: Fabio, F., Martin, S. (Eds.), Developments in Earth and Environmental Sciences, vol. 8, pp. 85–114. https://doi.org/10.1016/S1571-9197(08)00004-9.

Chiverrell, R.C., Thrasher, I.M., Thomas, G.S., Lang, A., Scourse, J.D., Van Landeghem, K.J.J., McCarroll, D., Clark, C.D., Cofaigh, C.Ó., Evans, D.J.A., Ballantyne, C.K., 2013. Bayesian modelling the retreat of the Irish sea ice stream. J. Quat. Sci. 28 (2), 200–209. https://doi.org/10.1002/jqs.2616.

Clapperton, C.M., 1993. Quaternary Geology and Geomorphology of South America, vol. 25. Elsevier, Amsterdam etc.

Clark, P.U., Dyke, A.S., Shakun, J.D., Carlson, A.E., Clark, J., Wohlfarth, B., Mitrovica, J.X., Hostetler, S.W., McCabe, A.M., 2009. The last glacial maximum. Science 325 (5941), 710–714. https://doi.org/10.1126/science.1172873.

Collins, L.G., Pike, J., Allen, C.S., Hodgson, D.A., 2012. High-resolution reconstruction of southwest Atlantic sea-ice and its role in the carbon cycle during marine isotope stages 3 and 2. Paleoceanography 27 (3), 1–17. https://doi.org/10.1029/2011PA002264.

Darvill, C.M., Bentley, M.J., Stokes, C.R., Hein, A.S., Rodés, Á., 2015. Extensive MIS 3 glaciation in southernmost Patagonia revealed by cosmogenic nuclide dating of outwash sediments. Earth Planet Sci. Lett. 429, 157–169. https://doi.org/10.1016/j.epsl.2015.07.030.

Darvill, C.M., Bentley, M.J., Stokes, C.R., Shulmeister, J., 2016. The timing and cause of glacial advances in the southern mid-latitudes during the last glacial cycle based on a synthesis of exposure ages from Patagonia and New Zealand. Quat. Sci. Rev. 149, 200–214. https://doi.org/10.1016/j.quascirev.2016.07.024.

Davies, B.J., Darvill, C.M., Lovell, H., Bendle, J.M., Dowdeswell, J.A., Fabel, D., Garcia, J.-L., Geiger, A., Glasser, N.F., Gheorghiu, D.M., Harrison, S., Hein, A.S., Kaplan, M.R., Martin, J.R.V., Mendelova, M., Palmer, A., Pelto, M., Rodes, A., Sagredo, E.A., Smedley, R., Smellie, J.L., Thorndycraft, V.R., 2020. The evolution of the patagonian ice sheet from 35 ka to the present day (PATICE). Earth Sci. Rev. 103152. https://doi.org/10.1016/j.earscirev.2020.103152.

De Deckker, P., Arnold, L.J., van der Kaars, S., Bayon, G., Stuut, J.B.W., Perner, K., Lopes dos Santos, R., Uemura, R., Demuro, M., 2019. Marine Isotope Stage 4 in Australasia: a full glacial culminating 65,000 years ago – global connections and implications for human dispersal. Quat. Sci. Rev. 204, 187–207. https://doi.org/10.1016/j.quascirev.2018.11.017.

Denton, G.H., Lowell, T.V., Heusser, C.J., Schlüchter, C., Andersen, B.G., Heusser, L.E., Moreno, P.I., Marchant, D.R., 1999. Geomorphology, stratigraphy, and radiocarbon chronology of llanquihue drift in the area of the southern lake district, Seno reloncaví, and Isla grande de Chiloé, Chile. Geogr. Ann. Phys. Geogr. 81 (2), 167–229. https://doi.org/10.1111/j.0435-3676.1999.00057.x.

Denton, G.H., Putnam, A.E., Russell, J.L., Barrell, D.J., Schaefer, J.M., Kaplan, M.R., Strand, P.D., 2021. The Zealandia Switch: ice age climate shifts viewed from Southern Hemisphere moraines. Quat. Sci. Rev. 257, 106771. https://doi.org/10.1016/j.quascirev.2020.106771.

Doughty, A.M., Schaefer, J.M., Putnam, A.E., Denton, G.H., Kaplan, M.R., Barrell, D.J., Andersen, B.G., Kelley, S.E., Finkel, R.C., Schwartz, R., 2015. Mismatch of glacier extent and summer insolation in Southern Hemisphere mid-latitudes. Geology 43 (5), 407–410. https://doi.org/10.1130/G36477.1.

Douglass, D.C., Singer, B.S., Kaplan, M.R., Mickelson, D.M., Caffee, M.W., 2006. Cosmogenic nuclide surface exposure dating of boulders on last-glacial and late-glacial moraines, Lago Buenos Aires, Argentina: interpretive strategies and paleoclimate implications. Quat. Geochronol. 1 (1), 43–58. https://doi.org/10.1016/j.quageo.2006.06.001.

Douglass, D.C., Singer, B., Ackert, R.P., Kaplan, M.R., Caffee, M.W., 2007. Constraining boulder erosion rates and ages of mid-pleistocene moraines in Lago Buenos Aires, Argentina. GSA Abstracts and Programs Northeastern Section, 42nd Annual Meeting.

EPICA Community Members, 2006. One-to-one coupling of glacial climate variability in Greenland and Antarctica. Nature 444 (7116), 195.

Evans, D.J.A., Benn, D.I. (Eds.), 2004. A Practical Guide to the Study of Glacial Sediments. Arnold, London, p. 266.
Fabel, D., Small, D., Miguens-Rodriguez, M., Freeman, S.P., 2010. Cosmogenic nuclide exposure ages from the 'parallel roads' of glen roy, Scotland. J. Quat. Sci.: Published for the Quaternary Research Association 25 (4), 597–603. https://doi.org/10.1002/jqs.1318.
Fick, S.E., Hijmans, R.J., 2017. WorldClim 2: new 1-km spatial resolution climate surfaces for global land areas. Int. J. Climatol. 37 (12), 4302–4315. https://doi.org/10.1002/joc.5086.
Fogwill, C.J., Turney, C.S.M., Hutchinson, D.K., Taschetto, A.S., England, M.H., 2015. Obliquity control on southern hemisphere climate during the last glacial. Sci. Rep. 5 (1), 1–10. https://doi.org/10.1038/srep11673.
García, J.L., 2012. Late Pleistocene ice fluctuations and glacial geomorphology of the Archipiélago de Chiloé, southern Chile. Geogr. Ann. Phys. Geogr. 94 (4), 459–479. https://doi.org/10.1111/j.1468-0459.2012.00471.x.
García, J.L., Hein, A.S., Binnie, S.A., Gómez, G.A., González, M.A., Dunai, T.J., 2018. The MIS 3 maximum of the Torres del Paine and Última Esperanza ice lobes in Patagonia and the pacing of southern mountain glaciation. Quat. Sci. Rev. 185, 9–26. https://doi.org/10.1016/j.quascirev.2018.01.013.
García, J.L., Maldonado, A., de Porras, M.E., Delaunay, A.N., Reyes, O., Ebensperger, C.A., Binnie, S.A., Lüthgens, C., Méndez, C., 2019. Early deglaciation and paleolake history of Río Cisnes glacier, Patagonian ice sheet (44° S). Quat. Res. 91 (1), 194–217. https://doi.org/10.1017/qua.2018.93.
García, J.L., Lüthgens, C., Vega, R.M., Rodés, Á., Hein, A.S., Binnie, S., 2021. A composite ^{10}Be, IR-50 and ^{14}C chronology of the pre-LGM full ice extent of the western Patagonian Ice Sheet in the Isla de Chiloé, south Chile (42°S). E&G Quaternary Science Journal 70, 105–128. https://doi.org/10.5194/egqsj-70-105-2021.
Garreaud, R., Lopez, P., Minvielle, M., Rojas, M., 2013. Large-scale control on the Patagonian climate. J. Clim. 26 (1), 215–230. https://doi.org/10.1175/JCLI-D-12-00001.1.
Glasser, N.F., Jansson, K.N., Harrison, S., Kleman, J., 2008. The glacial geomorphology and Pleistocene history of South America between 38°S and 56°S. Quat. Sci. Rev. 27 (3–4), 365–390. https://doi.org/10.1016/j.quascirev.2007.11.011.
Glasser, N., Jansson, K., 2008. The glacial map of southern South America. J. Maps 4 (1), 175–196. https://doi.org/10.4113/jom.2008.1020.
Glasser, N.F., Jansson, K.N., Duller, G.A., Singarayer, J., Holloway, M., Harrison, S., 2016. Glacial lake drainage in Patagonia (13-8 kyr) and response of the adjacent Pacific Ocean. Sci. Rep. 6, 21064. https://doi.org/10.1038/srep21064.
Gosse, J.C., Phillips, F.M., 2001. Terrestrial in situ cosmogenic nuclides: theory and application. Quat. Sci. Rev. 20 (14), 1475–1560. https://doi.org/10.1016/S0277-3791(00)00171-2.
Hall, B.L., Lowell, T.V., Brickle, P., 2020. Multiple glacial maxima of similar extent at~ 20–45 ka on Mt. Usborne, East Falkland, South Atlantic region. Quat. Sci. Rev. 250, 106677. https://doi.org/10.1016/j.quascirev.2020.106677.
Haller, M., Lech, R.R., Martinez, O.A., Meister, C.M., Page, S.M., 2003. Hoja Geologica 4373IV/III, Trevelin, Provincia del Chubut. Programa Nacional de Cartas Geologicas de la Republica Argentina, 1:250.000. Servicio Geologico Nacional, Buenos Aires.
Hein, A.S., Hulton, N.R., Dunai, T.J., Schnabel, C., Kaplan, M.R., Naylor, M., Xu, S., 2009. Middle Pleistocene glaciation in Patagonia dated by cosmogenic-nuclide measurements on outwash gravels. Earth Planet Sci. Lett. 286 (1–2), 184–197. https://doi.org/10.1016/j.epsl.2009.06.026.
Hein, A.S., Hulton, N.R., Dunai, T.J., Sugden, D.E., Kaplan, M.R., Xu, S., 2010. The chronology of the Last Glacial Maximum and deglacial events in central Argentine Patagonia. Quat. Sci. Rev. 29 (9–10), 1212–1227. https://doi.org/10.1016/j.quascirev.2010.01.020.
Hein, A.S., Dunai, T.J., Hulton, N.R., Xu, S., 2011. Exposure dating outwash gravels to determine the age of the greatest Patagonian glaciations. Geology 39 (2), 103–106. https://doi.org/10.1130/G31215.1.
Hein, A.S., Cogez, A., Darvill, C.M., Mendelová, M., Kaplan, M.R., Herman, F., Dunai, T.J., Norton, K., Xu, S., Christl, M., Rodés, Á., 2017. Regional mid-Pleistocene glaciation in central Patagonia. Quat. Sci. Rev. 164, 77–94. https://doi.org/10.1016/j.quascirev.2017.03.023.
Hemming, S.R., 2004. Heinrich events: massive late Pleistocene detritus layers of the North Atlantic and their global climate imprint. Rev. Geophys. 42 (1). https://doi.org/10.1029/2003RG000128.
Hervé, F., Fuentes, F., Calderón, M., Fanning, M., Quezada, P., Pankhurst, R., Rapela, C., 2017. Ultramafic rocks in the north patagonian Andes: is their emplacement associated with the neogene tectonics of the Liquiñe-Ofqui Fault zone? Andean Geol. 44 (1), 1–16. https://doi.org/10.5027/andgeoV44n1-a01.
Heyman, J., Stroeven, A.P., Harbor, J.M., Caffee, M.W., 2011. Too young or too old: evaluating cosmogenic exposure dating based on an analysis of compiled boulder exposure ages. Earth Planet Sci. Lett. 302 (1–2), 71–80. https://doi.org/10.1016/j.epsl.2010.11.040.
Heyman, J., Applegate, P.J., Blomdin, R., Gribenski, N., Harbor, J.M., Stroeven, A.P., 2016. Boulder height–exposure age relationships from a global glacial ^{10}Be compilation. Quat. Geochronol. 34, 1–11. https://doi.org/10.1016/j.quageo.2016.03.002.
Hubbard, A., Hein, A.S., Kaplan, M.R., Hulton, N.R., Glasser, N., 2005. A modelling reconstruction of the last glacial maximum ice sheet and its deglaciation in the vicinity of the Northern Patagonian Icefield, South America. Geogr. Ann. Phys. Geogr. 87 (2), 375–391. https://doi.org/10.1111/j.0435-3676.2005.00264.x.
Hulton, N.R., Purves, R.S., McCulloch, R.D., Sugden, D.E., Bentley, M.J., 2002. The last glacial maximum and deglaciation in southern South America. Quat. Sci. Rev. 21 (1–3), 233–241. https://doi.org/10.1016/S0277-3791(01)00103-2.
Jackson, R.H., Nash, J.D., Kienholz, C., Sutherland, D.A., Amundson, J.M., Motyka, R.J., Skyllingstad, E., Pettit, E.C., 2020. Meltwater intrusions reveal mechanisms for rapid submarine melt at a tidewater glacier. Geophys. Res. Lett. 47 (2), e2019GL085335. https://doi.org/10.1029/2019GL085335.
Johnsen, T.F., Olsen, L., Murray, A., 2012. OSL ages in central Norway support a MIS 2 interstadial (25–20 ka) and a dynamic Scandinavian ice sheet. Quat. Sci. Rev. 44, 96–111. https://doi.org/10.1016/j.quascirev.2010.10.007.
Jones, R.S., Small, D., Cahill, N., Bentley, M.J., Whitehouse, P.L., 2019. iceTEA: tools for plotting and analysing cosmogenic-nuclide surface-exposure data from former ice margins. Quat. Geochronol. 51, 72–86. https://doi.org/10.1016/j.quageo.2019.01.001.
Kaiser, J., Lamy, F., Hebbeln, D., 2005. A 70-kyr sea surface temperature record off southern Chile (Ocean Drilling Program Site 1233). Paleoceanography 20 (4). https://doi.org/10.1029/2005PA001146.
Kaiser, J., Lamy, F., Arz, H.W., Hebbeln, D., 2007. Dynamics of the millennial-scale sea surface temperature and Patagonian Ice Sheet fluctuations in southern Chile during the last 70 kyr (ODP Site 1233). Quat. Int. 161 (1), 77–89. https://doi.org/10.1016/j.quaint.2006.10.024.
Kaplan, M.R., Ackert, R.P., Singer, B.S., Douglass, D.C., Kurz, M.D., 2004. Cosmogenic nuclide chronology of millennial-scale glacial advances during O-isotope stage 2 in Patagonia. GSA Bulletin 116 (3–4), 308–321. https://doi.org/10.1130/B25178.1.
Kaplan, M.R., Douglass, D.C., Singer, B.S., Ackert, R.P., Caffee, M.W., 2005. Cosmogenic nuclide chronology of pre-last glacial maximum moraines at Lago Buenos Aires, 46°S, Argentina. Quat. Res. 63 (3), 301–315. https://doi.org/10.1016/j.yqres.2004.12.003.
Kaplan, M.R., Coronato, A., Hulton, N.R.J., Rabassa, J.O., Kubik, P.W., Freeman, S.P.H.T., 2007. Cosmogenic nuclide measurements in southernmost South America and implications for landscape change. Geomorphology 87 (4), 284–301. https://doi.org/10.1016/j.geomorph.2006.10.005.
Kaplan, M.R., Fogwill, C.J., Sugden, D.E., Hulton, N.R.J., Kubik, P.W., Freeman, S.P.H.T., 2008. Southern patagonian glacial chronology for the last glacial period and implications for southern ocean climate. Quat. Sci. Rev. 27 (3–4), 284–294. https://doi.org/10.1016/j.quascirev.2007.09.013.
Kaplan, M.R., Hein, A.S., Hubbard, A., Lax, S.M., 2009. Can glacial erosion limit the extent of glaciation? Geomorphology 103 (2), 172–179. https://doi.org/10.1016/j.geomorph.2008.04.020.
Kaplan, M.R., Strelin, J.A., Schaefer, J.M., Denton, G.H., Finkel, R.C., Schwartz, R., Putnam, A.E., Vandergoes, M.J., Goehring, B.M., Travis, S.G., 2011. In-situ cosmogenic 10Be production rate at Lago Argentino, Patagonia: implications for late-glacial climate chronology. Earth Planet Sci. Lett. 309 (1–2), 21–32. https://doi.org/10.1016/j.epsl.2011.06.018.
Kawamura, K., Parrenin, F., Lisiecki, L., Uemura, R., Vimeux, F., Severinghaus, J.P., Hutterli, M.A., Nakazawa, T., Aoki, S., Jouzel, J., Raymo, M.E., Matsumoto, K., Nakata, H., Motoyama, H., Fujita, S., Goto-Azuma, K., Fujii, Y., Watanabe, O., 2007. Northern Hemisphere forcing of climatic cycles in Antarctica over the past 360,000 years. Nature 448 (7156), 912–916. https://doi.org/10.1038/nature06015.
Kelley, S.E., Kaplan, M.R., Schaefer, J.M., Andersen, B.G., Barrell, D.J., Putnam, A.E., Denton, G.H., Schwartz, R., Finkel, R.C., Doughty, A.M., 2014. High-precision 10Be chronology of moraines in the Southern Alps indicates synchronous cooling in Antarctica and New Zealand 42,000 years ago. Earth Planet Sci. Lett. 405, 194–206. https://doi.org/10.1016/j.epsl.2014.07.031.
Lal, D., 1991. Cosmic ray labeling of erosion surfaces: *in situ* nuclide production. Earth Planet Sci. Lett. 104, 424–439. https://doi.org/10.1016/0012-821X(91)90220-C.
Lambeck, K., Rouby, H., Purcell, A., Sun, Y., Sambridge, M., et al., 2014. Sea level and global ice volumes from the Last Glacial Maximum to the Holocene. Proc. Natl. Acad. Sci. 111 (43), 15296–15303. https://doi.org/10.1073/pnas.1411762111.
Lamy, F., Arz, H.W., Kilian, R., Lange, C.B., Lembke-Jene, L., Wengler, M., Kaiser, J., Baeza-Urrea, O., Hall, I.R., Harada, N., Tiedemann, R., 2015. Glacial reduction and millennial-scale variations in Drake Passage throughflow. Proc. Natl. Acad. Sci. Unit. States Am. 112 (44), 13496–13501. https://doi.org/10.1073/pnas.1509203112.
Lamy, F., Kaiser, J., Ninnemann, U., Hebbeln, D., Arz, H.W., Stoner, J., 2004. Antarctic timing of surface water changes off Chile and Patagonian ice sheet response. Science 304 (5679), 1959–1962. https://doi.org/10.1126/science.1097863.
Lange, D., Cembrano, J., Rietbrock, A., Haberland, C., Dahm, T., Bataille, K., 2008. First seismic record for intra-arc strike-slip tectonics along the Liquiñe-Ofqui fault zone at the obliquely convergent plate margin of the southern Andes. Tectonophysics 455 (1–4), 14–24. https://doi.org/10.1016/j.tecto.2008.04.014.
Lapido, O., 1990. Glacial deposits on the patagonian cordillera at latitude 43°30′ south. Quat. S. Am. Antarct. Peninsula 6, 257–266.
Leger, T.P.M., Hein, A.S., Bingham, R.G., Martini, M.A., Rodrigo, L.S., Sagredo, E.A., Martínez, O.A., 2020. The glacial geomorphology of the Río Corcovado, Río Huemul and Lago palena/general vintter valleys, northeastern patagonia (43°S, 71°W). J. Maps 16 (2), 651–668. https://doi.org/10.1080/17445647.2020.1794990.
Leger, T.P.M., Hein, A.S., Goldberg, D., Schimmelpfennig, I., Van Wyk de Vries, M.S., Bingham, R.G., 2021. Northeastern Patagonian glacier advances (43°S) reflect northward migration of the Southern Westerlies towards the end of the last glaciation. Front. Earth Sci. https://doi.org/10.3389/feart.2021.751987 (in press).
Lenaerts, J.T., Van Den Broeke, M.R., van Wessem, J.M., van de Berg, W.J., van Meijgaard, E., van Ulft, L.H., Schaefer, M., 2014. Extreme precipitation and

climate gradients in Patagonia revealed by high-resolution regional atmospheric climate modeling. J. Clim. 27 (12), 4607–4621. https://doi.org/10.1175/JCLI-D-14-00660.1.
Lifton, N.A., Jull, A.T., Quade, J., 2001. A new extraction technique and production rate estimate for in situ cosmogenic 14C in quartz. Geochem. Cosmochim. Acta 65 (12), 1953–1969. https://doi.org/10.1016/S0016-7037(01)00566-X.
Lifton, N., Sato, T., Dunai, T.J., 2014. Scaling in situ cosmogenic nuclide production rates using analytical approximations to atmospheric cosmic-ray fluxes. Earth Planet Sci. Lett. 386, 149–160. https://doi.org/10.1016/j.epsl.2013.10.052.
Lifton, N., Caffee, M., Finkel, R., Marrero, S., Nishiizumi, K., Phillips, F.M., Goehring, B., Gosse, J., Stone, J., Schaefer, J., Theriault, B., Timothy Jull, A.J., Fifield, K., 2015. In situ cosmogenic nuclide production rate calibration for the CRONUS-Earth project from Lake Bonneville, Utah, shoreline features. Quat. Geochronol. 26, 56–69. https://doi.org/10.1016/j.quageo.2014.11.002.
Lopes dos Santos, R.A., Spooner, M.I., Barrows, T.T., De Deckker, P., Sinninghe Damsté, J.S., Schouten, S., 2013. Comparison of organic (UK'37, TEXH86, LDI) and faunal proxies (foraminiferal assemblages) for reconstruction of late Quaternary sea surface temperature variability from offshore southeastern Australia. Paleoceanography 28 (3), 377–387. https://doi.org/10.1002/palo.20035.
Mashiotta, T.A., Lea, D.W., Spero, H.J., 1999. Glacial–interglacial changes in Subantarctic sea surface temperature and δ18O-water using foraminiferal Mg. Earth Planet Sci. Lett. 170 (4), 417–432. https://doi.org/10.1016/S0012-821X(99)00116-8.
Martin, J.R., Davies, B.J., Thorndycraft, V.R., 2019. Glacier dynamics during a phase of Late Quaternary warming in Patagonia reconstructed from sediment landform associations. Geomorphology 337, 111–133. https://doi.org/10.1016/j.geomorph.2019.03.007.
Martínez, O., 2002. Geomorfología y geología de los depositós glaciarios y periglaciarios de la región comprendida entre los 43° y 44° lat. Sur y 70°30' y 72° long. Oeste, Chubut, República Argentina. Universidad Nacional de la Patagonia-San Juan Bosco, unpublished doctoral thesis, Comodoro Rivadavia and Esquel.
Martínez, O., Coronato, A., Rabassa, J., 2011. Pleistocene glaciations in northern Patagonia, Argentina: an updated review. In: Developments in Quaternary Sciences, vol. 15. Elsevier, pp. 729–734. https://doi.org/10.1016/j.quaint.2009.06.019.
McCulloch, R.D., Fogwill, C.J., Sugden, D.E., Bentley, M.J., Kubik, P.W., 2005. Chronology of the last glaciation in central Strait of magellan and Bahía Inútil, southernmost south America. Geogr. Ann. Phys. Geogr. 87 (2), 289–312. https://doi.org/10.1111/j.0435-3676.2005.00260.x.
Mendelová, M., Hein, A.S., McCulloch, R., Davies, B., 2017. The last glacial maximum and deglaciation in central Patagonia, 44° S–49° S. Cuadernos de Investigación Geográfica 43 (2), 719–750. https://doi.org/10.18172/cig.3263.
Mendelová, M., Hein, A.S., Rodés, Á., Xu, S., 2020a. Extensive mountain glaciation in central patagonia during marine isotope stage 5. Quat. Sci. Rev. 227, 105996. https://doi.org/10.1016/j.quascirev.2019.105996.
Mendelová, M., Hein, A.S., Rodés, Á., Smedley, R.K., Xu, S., 2020b. glacier expansion in central patagonia during the antarctic cold reversal followed by retreat and stabilisation during the younger dryas. Quat. Sci. Rev. 227, 106047. https://doi.org/10.1016/j.quascirev.2019.106047.
Mercer, J.H., 1972. Chilean glacial chronology 20,000 to 11,000 carbon-14 years ago: some global comparisons. Science 176 (4039), 1118–1120. https://doi.org/10.1210/jcem-10-10-1361.
Mercer, J.H., 1976. Glacial history of southernmost south America. Quat. Res. 6 (2), 125–166. https://doi.org/10.1016/0033-5894(76)90047-8.
Moreno, P.I., Denton, G.H., Moreno, H., Lowell, T.V., Putnam, A.E., Kaplan, M.R., 2015. Radiocarbon chronology of the last glacial maximum and its termination in northwestern Patagonia. Quat. Sci. Rev. 122, 233–249. https://doi.org/10.1016/j.quascirev.2015.05.027.
Moreno, P.I., Videla, J., Valero-Garcés, B., Alloway, B.V., Heusser, L.E., 2018. A continuous record of vegetation, fire-regime and climatic changes in northwestern Patagonia spanning the last 25,000 years. Quat. Sci. Rev. 198, 15–36. https://doi.org/10.1016/j.quascirev.2018.08.013.
Murray, D.S., Carlson, A.E., Singer, B.S., Anslow, F.S., He, F., Caffee, M., Marcott, S.A., Liu, Z., Otto-Bliesner, B.L., 2012. Northern Hemisphere forcing of the last deglaciation in southern Patagonia. Geology 40 (7), 631–634. https://doi.org/10.1130/G32836.1.
Members, N.G.R.I.P., 2004. High-resolution record of the Northern Hemisphere climate extending into the last interglacial period. Nature 431, 147–151. https://doi.org/10.1038/nature02805.
Nishiizumi, K., Imamura, M., Caffee, M.W., Southon, J.R., Finkel, R.C., McAninch, J., 2007. Absolute calibration of 10Be AMS standards. Nucl. Instrum. Methods Phys. Res. Sect. B Beam Interact. Mater. Atoms 258 (2), 403–413. https://doi.org/10.1016/j.nimb.2007.01.297.
Orsi, A.H., Whitworth III, T., Nowlin Jr., W.D., 1995. On the meridional extent and fronts of the Antarctic Circumpolar Current. Deep Sea Res. Oceanogr. Res. Pap. 42 (5), 641–673. https://doi.org/10.1016/0967-0637(95)00021-W.
Pahnke, K., Zahn, R., Elderfield, H., Schulz, M., 2003. 340,000-year centennial-scale marine record of Southern Hemisphere climatic oscillation. Science 301 (5635), 948–952. https://doi.org/10.1126/science.1084451.
Pankhurst, R.J., Hervé, F., Rojas, L., Cembrano, J., 1992. Magmatism and tectonics in continental Chiloé, Chile (42–42 30′ S). Tectonophysics 205 (1–3), 283–294. https://doi.org/10.1016/0040-1951(92)90431-5.
Pedro, J.B., Jochum, M., Buizert, C., He, F., Barker, S., Rasmussen, S.O., 2018. Beyond the bipolar seesaw: toward a process understanding of interhemispheric coupling. Quat. Sci. Rev. 192, 27–46. https://doi.org/10.1016/j.quascirev.2018.05.005.
Peltier, C., Kaplan, M.R., Birkel, S.D., Soteres, R.L., Sagredo, E.A., Aravena, J.C., Araos, J., Moreno, P.I., Schwartz, R., Schaefer, J.M., 2021. A large MIS 4 and long MIS 2 glacier maximum on the southern tip of South America. Quat. Sci. Rev. 262, 106858. https://doi.org/10.1016/j.quascirev.2021.106858.
Putkonen, J., Swanson, T., 2003. Accuracy of cosmogenic ages for moraines. Quat. Res. 59 (2), 255–261. https://doi.org/10.1016/S0033-5894(03)00006-1.
Putnam, A.E., Schaefer, J.M., Barrell, D.J.A., Vandergoes, M., Denton, G.H., Kaplan, M.R., Finkel, R.C., Schwartz, R., Goehring, B.M., Kelley, S.E., 2010. In situ cosmogenic 10Be production-rate calibration from the Southern Alps, New Zealand. Quat. Geochronol. 5 (4), 392–409. https://doi.org/10.1016/j.quageo.2009.12.001.
Putnam, A.E., Schaefer, J.M., Denton, G.H., Barrell, D.J., Andersen, B.G., Koffman, T.N., Rowan, A.V., Finkel, R.C., Rood, D.H., Schwartz, R., Vandergoes, M.J., Plummer, M.A., Brocklehurst, S.H., Kelley, S.E., Ladig, K.L., 2013. Warming and glacier recession in the rakaia valley, southern Alps of New Zealand, during Heinrich stadial 1. Earth Planet Sci. Lett. 382, 98–110. https://doi.org/10.1016/j.epsl.2013.09.005.
Rignot, E., Mouginot, J., Scheuchl, B., van den Broeke, M., van Wessem, M.J., Morlighem, M., 2019. Four decades of antarctic ice sheet mass balance from 1979–2017. Proc. Natl. Acad. Sci. Unit. States Am. 116 (4), 1095–1103. https://doi.org/10.1073/pnas.1812883116.
Rosenau, M., Melnick, D., Echtler, H., 2006. Kinematic constraints on intra-arc shear and strain partitioning in the southern Andes between 38°S and 42°S latitude. Tectonics 25 (4). https://doi.org/10.1029/2005TC001943.
Schaefer, J.M., Putnam, A.E., Denton, G.H., Kaplan, M.R., Birkel, S., Doughty, A.M., Kelley, S.E., Barrell, D.J.A., Finkel, R.C., Winckler, G., Anderson, R.F., Ninneman, U.S., Barker, S., Schwartz, R., Andersen, B.J., Schluechter, C., 2015. The southern glacial maximum 65,000 years ago and its unfinished termination. Quat. Sci. Rev. 114, 52–60. https://doi.org/10.1016/j.quascirev.2015.02.009.
Shulmeister, J., Fink, D., Hyatt, O.M., Thackray, G.D., Rother, H., 2010. Cosmogenic ^{10}Be and ^{26}Al exposure ages of moraines in the Rakaia Valley, New Zealand and the nature of the last termination in New Zealand glacial systems. Earth Planet Sci. Lett. 297 (3–4), 558–566. https://doi.org/10.1016/j.epsl.2010.07.007.
Shulmeister, J., Thackray, G.D., Rittenour, T.M., Fink, D., Patton, N.R., 2019. The timing and nature of the last glacial cycle in New Zealand. Quat. Sci. Rev. 206, 1–20. https://doi.org/10.1016/j.quascirev.2018.12.020.
Singer, B.S., Laurie, L.B., Rabassa, J.O., Guillou, H., 2004. ^{40}Ar/^{39}Ar chronology of late pliocene and early pleistocene geomagnetic and glacial events in southern Argentina. Geophys. Monogr. 145, 175–190. https://doi.org/10.1029/145GM13.
Sime, L.C., Kohfeld, K.E., Le Quéré, C., Wolff, E.W., de Boer, A.M., Graham, R.M., Bopp, L., 2013. Southern Hemisphere westerly wind changes during the Last Glacial Maximum: model-data comparison. Quat. Sci. Rev. 64, 104–120. https://doi.org/10.1016/j.quascirev.2012.12.008.
Sissons, J.B., 1978. The parallel roads of Glen Roy and adjacent glens, Scotland. Boreas 7 (4), 229–244. https://doi.org/10.1111/j.1502-3885.1978.tb00281.x.
Small, D., Bentley, M.J., Jones, R.S., Pittard, M.L., Whitehouse, P.L., 2019. Antarctic ice sheet palaeo-thinning rates from vertical transects of cosmogenic exposure ages. Quat. Sci. Rev. 206, 65–80. https://doi.org/10.1016/j.quascirev.2018.12.024.
Smedley, R.K., Glasser, N.F., Duller, G.A.T., 2016. Luminescence dating of glacial advances at Lago Buenos Aires (~46°S), patagonia. Quat. Sci. Rev. 134, 59–73. https://doi.org/10.1016/j.quascirev.2015.12.010.
Sneed, E.D., Folk, R.L., 1958. Pebbles in the lower Colorado River, Texas a study in particle morphogenesis. J. Geol. 66 (2), 114–150. https://doi.org/10.1086/626490.
Soteres, R.L., Peltier, C., Kaplan, M.R., Sagredo, E.A., 2020. Glacial geomorphology of the Strait of magellan ice lobe, southernmost patagonia, south America. J. Maps 16 (2), 299–312. https://doi.org/10.1080/17445647.2020.1736197.
Spencer, C.J., Yakymchuk, C., Ghaznavi, M., 2017. Visualising data distributions with kernel density estimation and reduced chi-squared statistic. Geoscience Frontiers 8 (6), 1247–1252. https://doi.org/10.1016/j.gsf.2017.05.002.
Stenni, B., Buiron, D., Frezzotti, M., Albani, S., Barbante, C., Bard, E., Barnola, J.M., Baroni, M., Baumgartner, M., Bonazza, M., Capron, E., Castellano, E., Chappellaz, J., Delmonte, B., Falourd, S., Genoni, L., Iacumin, P., Jouzel, J., Kipfstuhl, S., Landais, A., Lemieux-Dudon, B., Maggi, V., Masson-Delmotte, V., Mazzola, C., Minster, B., Montagnat, M., Mulvaney, R., Narcisi, B., Oerter, H., Parrenin, F., Petit, J.R., Ritz, C., Scarchilli, C., Schilt, A., Schüpbach, S., Schwander, J., Selmo, E., Severi, M., Stocker, T.F., Udisti, R., 2011. Expression of the bipolar see-saw in Antarctic climate records during the last deglaciation. Nat. Geosci. 4 (1), 46–49. https://doi.org/10.1038/ngeo1026.
Stern, C.R., de Porras, M.E., Maldonado, A., 2015. Tephrochronology of the upper Río Cisnes valley (44°S), southern Chile. Andean Geol. 42 (2), 173–189. https://doi.org/10.5027/andgeoV42n2-a02.
Stone, J.O., 2000. Air pressure and cosmogenic isotope production. J. Geophys. Res.: Solid Earth 105 (B10), 23753–23759. https://doi.org/10.1029/2000jb900181.
Strand, P.D., Schaefer, J.M., Putnam, A.E., Denton, G.H., Barrell, D.J., Koffman, T.N., Schwartz, R., 2019. Millennial-scale pulsebeat of glaciation in the southern Alps of New Zealand. Quat. Sci. Rev. 220, 165–177. https://doi.org/10.1016/j.quascirev.2019.07.022.
Sutherland, J.L., Carrivick, J.L., Gandy, N., Shulmeister, J., Quincey, D.J., Cornford, S.L., 2020. Proglacial lakes control glacier geometry and behavior during recession. Geophys. Res. Lett. 47, e2020GL088865. https://doi.org/10.1029/2020gl088865.
Thomson, S.N., Herve, F., 2002. New time constraints for the age of metamorphism at the ancestral Pacific Gondwana margin of southern Chile (42-52 S). Rev. Geol. Chile 29 (2), 255–271. https://doi.org/10.4067/S0716-02082002000200007.

Thorndycraft, V.R., Bendle, J.M., Benito, G., Davies, B.J., Sancho, C., Palmer, A.P., Fabel, D., Medialdea, A., Martin, J.R., 2019. Glacial lake evolution and Atlantic-Pacific drainage reversals during deglaciation of the Patagonian Ice Sheet. Quat. Sci. Rev. 203, 102–127. https://doi.org/10.1016/J.QUASCIREV.2018.10.036.

Turner, K.J., Fogwill, C.J., McCulloch, R.D., Sugden, D.E., 2005. Deglaciation of the eastern flank of the North Patagonian Icefield and associated continental-scale lake diversions. Geogr. Ann. Phys. Geogr. 87 (2), 363–374. https://doi.org/10.1111/j.0435-3676.2005.00263.x.

Van Daele, M., Bertrand, S., Meyer, I., Moernaut, J., Vandoorne, W., Siani, G., Tanghe, N., Ghazoui, Z., Pino, M., Urrutia, R., De Batist, M., 2016. Late Quaternary evolution of Lago Castor (Chile, 45.6°S): timing of the deglaciation in northern Patagonia and evolution of the southern westerlies during the last 17 kyr. Quat. Sci. Rev. 133, 130–146. https://doi.org/10.1016/j.quascirev.2015.12.021.

Ward, G.K., Wilson, S.R., 1978. Procedures for comparing and combining radiocarbon age determinations: a critique. Archaeometry 20 (1), 19–31. https://doi.org/10.1111/j.1475-4754.1978.tb00208.x.

WAIS Divide Project Members, 2013. Onset of deglacial warming in West Antarctica driven by local orbital forcing. Nature 500 (7463), 440–444. https://doi.org/10.1038/nature12376.

WAIS Divide Project Members, 2015. Precise interpolar phasing of abrupt climate change during the last ice age. Nature 520 (7549), 661. https://doi.org/10.1038/nature14401.

Wallinga, J., 2002. On the detection of OSL age overestimation using single-aliquot techniques. Geochronometria: Journal on Methods & Applications of Absolute Chronology 21.

Wendt, I., Carl, C., 1991. The statistical distribution of the mean squared weighted deviation. Chem. Geol. Isot. Geosci. 86 (4), 275–285. https://doi.org/10.1016/0168-9622(91)90010-T.

Whittaker, T.E., Hendy, C.H., Hellstrom, J.C., 2011. Abrupt millennial-scale changes in intensity of Southern Hemisphere westerly winds during marine isotope stages 2–4. Geology 39 (5), 455–458. https://doi.org/10.1130/G31827.1.

Geomorphology and ^{10}Be chronology of the Last Glacial Maximum and deglaciation in northeastern Patagonia, 43°S-71°W - Supplementary materials

Tancrède P. M. Leger, Andrew S. Hein, Robert G. Bingham, Ángel Rodés, Derek Fabel, Rachel K. Smedley

1. Study site former glaciolacustrine phases: additional geomorphological evidence and interpretation

1.1. Glaciolacustrine phase one

Handheld GPS elevation transects revealed the preservation of at least five notched terraces running parallel to each other over tens of kilometres on the northeastern, eastern and southern slopes of the palaeolake basin. These features range in elevation from 910 ± 5 m to 990 ± 5 m, where the most prominent platform lies, and were interpreted as wave-cut palaeo-shorelines (SM Table 1). On the southwestern edge of the palaeolake basin, a well-preserved, low-gradient (mean slope: 0.8°) outwash plain deposit progrades from both arcuate terminal moraines of the RC III complex to the north and Lago Palena/General Vintter terminal moraines to the west (43°51'S, 71°16'W). This outwash plain lies at elevations of between ~980 and ~965 m, and appears to be raised ~100 m above the modern valley floor (880 m). It was thus interpreted as a raised outwash deposit formed by glaciofluvial sediment aggradation during proglacial lake residence. On the palaeolake basin's southern slopes, at 43°50'59"S, 71°11'13"W, the palaeo-shorelines bend southward into a 230 m-wide gorge, which acts as a breach through RC II glaciogenic deposits. This breach reaches a maximum basal elevation of 980 m, leads southward to a 100 m-wide palaeo meltwater channel incised into RC II-related outwash deposits, and is indicative of southeast-directed palaeolake drainage towards the contemporary Río Ñirihuau O Seco. It was interpreted as the main proglacial lake spillway. At this location, the RC II deposits mark the local Atlantic-Pacific drainage divide, and thus represent the southeastern limit of the RC valley over-deepening.

1.2. Glaciolacustrine phase two

The second glaciolacustrine phase identified is associated with the retreat of the RC and RH outlet glaciers from intermediate LGM margins into their respective over-deepened, westward-dipping valleys. Remote sensing and field observations uncovered the relatively widespread occurrence of preserved palaeo-shorelines nested at the elevation of ~790-800 m in both the RC and RH valleys (Leger *et al*., 2020, main map). In the RC valley, the palaeo-shoreline can be discerned across the RC eastern sub-basin, notched on the ice-proximal slopes of the RC V moraine complex (SM Table 1). Such evidence suggests that initial lake formation for this second phase occurred following ice-front retreat from the RC VI and RC V moraines. Remote sensing analysis reveals that this basin is characterised by a low gradient bed (~0.5° average slope), and the noticeable occurrence of incised, white to light grey deposits interpreted and mapped as glaciolacustrine sediment accumulations (Leger *et al*., 2020; nearby 43°42'S, 71°16'W). We propose that the 790 m proglacial lake's main spillway occurred at 43°42'S, 71°13'W, where the prominent shoreline bends eastwards into a 200 m-wide gorge breaching RC V and RC IV moraine complexes, leading to the Atlantic/Pacific drainage divide and a large, 215 m-wide palaeo-channel heading northward, towards Río Tecka (SM Table 1).

~10 km to the northwest, in the more topographically-constrained RC trough, isolated patches of the 790 m palaeo-shoreline can be discerned on the eastern hillslope (Figure 5a), while evidence of this shoreline disappears north of 43°37'S. This suggests that this proglacial lake might have expanded and persisted during the early stages of local deglaciation, when the RC calving front progressively retreated northward. This is supported by the finding of fine, sand to clay-sized sediment deposits exposed through sections of the valley's main road (RP44), at elevations of 686 m (43°42'7.2"S), 709 m (43°42'15.2"S) and 720 m (43°42'11.7"S). In each cases, these exposures exhibit laminations and varves, represent the topmost unit below soil, and were interpreted as glaciolacustrine deposits. Rippled sands from the 709 m exposure and varves from the 686 m exposure were sampled for OSL dating (see main text).

In the RH valley, field mapping revealed the instance of a prominent bench running over tens of kilometres on the southern valley slopes, perched at an elevation of ~790 m, and nested on the ice-proximal side of the innermost preserved terminal RH moraine, forming a clear step 15 m below the moraine crest (Figure 2, 4c, d). This landform was interpreted as a former proglacial lake shoreline and was sampled for TCN dating using polished granite surface cobbles (Figure 4d, e). DEM elevation profiles and approximate palaeo-surface reconstructions based on hillside and backing cliff slope angles revealed, on average, a maximum shoreline excavation of ~4 m around the location of sampling. Risk of shoreline post-formation burial is regarded as minimal due to the limited height (<15m) and slope gradient (7°) of overlying moraine (Figure 4d). This landform thus indicates the formation of a separate, isolated proglacial lake in the RH valley, formed as the RH glacier retreated westward. However, the comparable elevation of shorelines in both the RC and RH valleys suggests that both RC and RH proglacial lakes could have been connected during phase two, following northward/westward retreat of both ice-fronts beyond Corcovado (43°32'S, 71°27'W). The main spillway draining the RH palaeolake towards the Atlantic occurs at 43°31'42.S,

71°13’26.W, where a central, 130 m-wide breach through the innermost RH moraine complex reaches a maximum basal elevation of 780 m (Figure 6b). The breach leads to a 250 m-wide southward-directed palaeo-channel, which reaches the Atlantic/Pacific drainage divide 2.5 km to the southeast and heads towards Río Tecka.

1.3. Glaciolacustrine phase three

The eastern, windier hillslope of the RC valley displays a second, easily discernible platform cutting through the entire north-to-south extent (over 15 km) of the 16-19° sloped hillside, at the elevation of ~680 m (Figure 4a, 6c). It was studied in the field, interpreted as a wave-cut proglacial lake shoreline, and was sampled for TCN dating using polished granite surface cobbles (Figure 4b, 6c). Twenty-seven terrace cross-section elevation profiles were drawn from DEM in locations exhibiting a preserved platform. They revealed, on average, a maximum shoreline excavation of ~6 m. At the location of sampling, maximum excavation appears to be closer to 7 m. This shoreline roughly matches the elevations of numerous other shorelines, raised deltas and raised outwash deposits located in the RC, RH, RF and RP valleys (SM Table 1). Such geomorphic evidences suggest the formation of a geographically widespread proglacial lake connecting all valleys of the studied region during the last glacial termination (Figure 9g). This is further evidenced by field observations of uppermost (below soil) units of fine, sand to clay-sized and occasionally laminated, varved sediments exposed along several road-cut sections across the RC, RP and RF valley floors (SM Table 1). However, observed elevations of different landforms associated with glaciolacustrine phase three fluctuate between 675 and 695 m. We attribute this variation to a combination of 1) DEM and GPS vertical measurement error, and 2) asymmetrical local isostatic rebound and tectonic activity since landform stabilization. Subsequently, we interpret this third glaciolacustrine phase to have started with the ~100 m lake level drop from 790 m (phase two) to ~680 m (Figure 9f).

We argue that this proglacial lake lowering to phase three is likely due to the continued northward, westward and southward retreats of the RC, RH and RF ice fronts into the RP valley during the last glacial termination. In doing so, the northern RF ice-dam was breached, and proglacial lake waters from both RC and RH valleys were able to flow northward into the narrow, low-gradient (average slope: 0.5°) and over-deepened RF valley. By modelling a hypothetical ice front of maximum eastward extent while enabling proglacial lake connection of all three RC, RH and RF valleys, the reconstructed 680 m lake approximates 266 km^2 in surface area and 32.7 km^3 in volume (computed from DEM; Figure 9f).

In the RF valley, the lowest potential spillway towards the northeast lies at approximately 750 m. Such spillway would enable waters to drain towards contemporary Lago Rosario (aerial cover; 9.6 km^2), which in turn drains towards the Trevelin basin to the north, and the Pacific

Ocean via Río Futaleufú. Work by Andrada de Palomera (2002) and Martínez *et al*. (2011) suggest the former occurrence of yet another large proglacial lake in the Trevelin and Esquel over-deepened valleys following local glacier recession, with a lowest possible spillway nested at ~650 m through terminal moraines located east of Laguna Suñica (43°05'57"S, 71°02'48"W). We thus propose, during glaciolacustrine phase three, a complex hypothetical network of connected, extensive palaeolakes enabling meltwater drainage from the former RC, RH and RF-connected lake (~680 m) into the current Lago Rosario (665m), and into a former Trevelin basin proglacial lake (~650m), which eventually spilled eastward towards Río Tecka and the Atlantic Ocean. The RF palaeolake-connection hypothesis is further evidenced by the ~680 m elevation of raised deltas and palaeo-shorelines observed in the RF valley, and the lack of raised landforms above this elevation (SM Table 1). However, in modern times, such lake connection would be impossible due to 60-70 m of localised excess land surface in the RF valley impeding a ~680 m lake connection towards Lago Rosario. We here hypothesise that this land-elevation mismatch can be attributed to the accretion of a large (~5 km^2) arcuate alluvial fan into a narrow col located between the RF and Lago Rosario basins (43°17"S; 71°24"W).

The alluvial fan is formed at the bottom of the steep RF upland catchment, where the RF channel discharges water and sediment from the mountain front to the main, lower-gradient valley. It exhibits an average radial slope gradient of 1.95°, and a maximum radial length of 4.5 km towards the south-west. The upper mountain catchment displays 900 m of vertical relief, a maximum elevation of ~1800 m, and some geomorphological evidence of slope instabilities. Our geomorphological mapping reveals small, empty cirques around the catchment summit indicating the former occurrence of topographically constrained mountain glaciers. No sedimentological analyses were conducted due to a lack of access to fan sediment exposures. Using 70 m of material aggradation and bracketing ages of 16.3 ± 0.8 ka (minimum age for phase three lake lowering, Figure 8) and 19.9 ka ± 1.1 ka (RC VII age, onset of glacial retreat in RC valley, Figure 8) as the potential onsets of alluvial fan accretion, we obtain sedimentation rates ranging between 3.4 and 4.5 mm $.yr^{-1}$. Such high sedimentation rates suggest a dominating contribution of infrequent, high-magnitude flood and/or mass-wasting events to fan aggradation (Blair & McPherson, 2009). Possible events of sporadic high-material/water discharge include rapid spring snow/glacial melt and non-cohesive sediment-gravity flows caused by 1) moraine and/or ice dam failure or 2) large-scale slope failure such as rock-slope failures, rotational slumps and other landslides, sometimes triggered during earthquakes. The latter hypothesis could possibly be supported by the observation (from DEM) of a large and heavily incised oversteepening resembling a series of steep scarps running for ~4 km across the RF upper catchment, with upper break-in-slopes nested between 1350 m and 1500 m. Such slope failure events are not unusual on tectonically active and formerly glaciated, steep mountain slopes with substantial volumes of poorly sorted till and lateral moraine deposits mantling the catchments (Blair, 2009).

For the ~680 m proglacial lake to exploit a lower spillway col and drain further, the western Palena ice dam had to retreat 45 km west of Corcovado, towards the eastern foothills of Macizo Nevado (Figure 9g). We expect such extensive retreat to cause the disintegration of the local

PIS into smaller, separate mountain ice caps, causing ice-free conditions in low-lying (100-150 m) local valley floors, and enabling the ~680 m proglacial lake to drain westward between or beneath shrinking ice-masses (Figure 9h). Such event would have caused proglacial lake drainage reversal from the Atlantic to the Pacific Ocean (Figure 9h), similarly to other over-deepened eastern Patagonian valleys (Thorndycraft *et al.*, 2019). Depending on the configuration and extent of local glaciers at the time of ice-dam breach, glaciolacustrine waters could have either drained westward using; 1) a northwest-directed pathway towards the modern Lago Yelcho (115 km^2), elevated at ~40 m, or 2) a valley narrowing (~2 km-wide) located to the south of Macizo Nevado (43°43'S; 72°13'W) and exploited by the modern Río Palena. The latter drainage route heads south using the prominent LOFZ valley to eventually drain into Golfo Corcovado at Puerto Rául Marín Balmaceda (43°46'S; 72°57'W). Resolving the former pathways of final lake drainage would require more detailed sedimentological and geomorphological investigations in these regions. Such work could also reveal whether the Atlantic/Pacific drainage reversal was a progressive or catastrophic event in this region. In both cases, the ~680 m proglacial lake would have drained into the Golfo Corcovado. Using an approximate PIS configuration associated with a maximum proglacial lake extent prior to western ice-dam breach, the reconstructed 680 m proglacial lake approximates 950 km^2 in area and 273 km^3 in volume (Figure 9g, computed from DEM). These estimates yield significant uncertainties, however, as they were computed using a hypothetical ice-dam location near the foothills of Macizo Nevado (Figure 9g), under the assumption that any further westward retreat of the ice front would likely cause ice-dam breach.

SM Table 1: Summary of geomorphological and sedimentological field-based evidence for former glaciolacustrine activity across the study site

Feature type	Latitude (DD)	Longitude (DD)	Valley / basin	Elevation (m a.s.l)	Feature geomorphological / sedimentological description	Interpretation & hypothesised geomorphological significance	Glaciolacustrine phase-association	Suggested formation / deposition age
Landform	-43.793199	-71.234376	RC valley		Two raised terraces nested on ice-distal slope of RC III moraine.	Interpreted as raised outwash deposits associated with RC III meltwater drainage into proglacial lake, representing two distinc lake levels.	Phase 1	≥26.4 ± 1.4 ka
Landform	-43.930778	-71.166394	RC valley	~910	Prominent terrace protruding from surrounding terrain, with surface clasts dominated by sands and rounded to subrounded pebbles.	Interpreted as beach deposit drapping a wave-cut platform associated with former proglacial lake surface.	Phase 1	>22.4 ± 1.2 ka and < 26.6 ka
Landform	-43.794059	-71.234099	RC valley	~960	Prominent terrace running across the ice-distal slope of the RC3 moraine at a single elevation.	Interpreted as palaeo-shoreline, suggests stabilisation of former proglacial lake at ~960 m.	Phase 1	≥26.4 ± 1.4 ka
Landform	-43.823247	-71.163322	RC valley	~960	Prominent terrace feature nested on the eastern slopes of the RC western sub-basin at single evelation.	Interpreted as palaeo-shoreline, suggests a former proglacial lake stabilized at ~960 m.	Phase 1	≥26.4 ± 1.4 ka
Landform	-43.824091	-71.154785	RC valley	~990	Prominent terrace feature nested on the northeastern slopes of the RC western sub-basin at single evelation.	Interpreted as palaeo-shoreline, suggests a former proglacial lake stabilized at ~990 m.	Phase 1	≥26.4 ± 1.4 ka
Landform	-43.618186	-71.381267	RC valley	~790	Terrace feature running at single elevation across the eastern mountain slope of the RC trough.	Interpreted as palaeo-shoreline, suggests a former proglacial lake stabilised at ~790 m.	Phase 2	> 19.0 ± 0.9 ka < 21.7 ± 0.9 ka
Landform	-43.731778	-71.258657	RC, northern sub-basin	~790	Series of terraces running across the northern slopes of the mid-valley 300 m-high bedrock step separating the northern and southern RC sub-basins.	Interpreted as palaeo-shorelines, suggests a former proglacial lake stabilised at ~790 m.	Phase 2	> 19.0 ± 0.9 ka < 21.7 ± 0.9 ka
Landform	-43.704880	-71.225869	RC, northern sub-basin	~790	200 m-wide and 20 m-deep gorge cutting through RC V and RC IV moraine complexes, with a maximum basal elevation of ~795 m, and associated with a northward bending and confluence of mapped palaeo-shorelines.	Interpreted as former proglacial lake spillway opening, indicating the location, elevation, and downflow direction of proglacial lacustrine water drainage.	Phase 2	> 19.0 ± 0.9 ka < 21.7 ± 0.9 ka
Lanform	-43.746482	-71.395796	RC valley	~790-800	Low-gradient fan-shaped terrace prograding from the mouth of the Río Comisario tributary river, "raised" as further incised by modern river located ~30 m below terrace.	Elevation of raised terrace matches former elevation of RC proglacial lake during phase two (~790 m). This landform was thus possibly formed as a fan deposit when the Río Comisario flowed into the proglacial lake and could be interpreted as a raised delta. Alternatively, the matching elevation could be a coincidence and this landform could simply relate to fluvial and/or glaciofluvial terrace aggradation.	Phase 2	> 19.0 ± 0.9 ka < 21.7 ± 0.9 ka

Landform	-43.73818	-71.223582	RC, northern sub-basin	~790	Series of large terraces with clear incision scarps nested on the northern slopes of the RC mid-valley bedrock step: where the Río Corcovado flows out of narrow gorge to reach the low-gradient eastern sub-basin. The teraces are raised by ~50 m above modern river and located on both sides of the channel.	Those fluvial terraces match the elevation of former RC proglacial lake during phase 2 (790-800 m) and are raised by up to 50 m. These landforms were thus possibly formed as fan deposits when the Río Corcovado flowed into the 790m proglacial lake located in the eastern sub-basin. They could potentially be interpreted as raised deltas.	Phase 2	> 19.0 ± 0.9 ka < 21.7 ± 0.9 ka
Landform	-43.697673	-71.216309	RC, northern sub-basin	~800	Low-gradient, 200 m wide palaeo-channel located directly to the northeast of spillway opening associated with proglacial lake phase 2, with a basal elevation of ~800 m and gently prograding towards the north: and Río Tecka.	This palaeo-channel can be linked to the location and elevation of the proglaical lake phase 2 spillway opening: and represents a substantially larger discharge regime than modern runoff can enable (by several orders of magnitude). We thus interpret this landform as the location of glaciolactustrine water drainage during proglacial lake phase 2.	Phase 2	> 19.0 ± 0.9 ka < 21.7 ± 0.9 ka
Landform	-43.728158	-71.397497	RC valley	~790	Terrace feature running at single elevation across the northern, ice-proximal slope of the RCVII moraine. The notched platform was revealed through DEM cross-moraine elevation profiles and demonstrates an average excavation height of ~7 m.	Interpreted as palaeo-shoreline, sugests stabilisation of former proglacial lake at ~790 m in the RC valley	Phase 2	> 19.0 ± 0.9 ka < 21.7 ± 0.9 ka
Sediment exposure	-43.703130	-71.41177	RC valley	709	Section with top-most (below soil) unit of undistrubed and homogeneous sands with cross-beddings and asymmetrical ripples. 1 m below surface, sands make place for homogeneous laminated and alternating silt and clay sediment layers (varves)	We interpret these sediments as glaciolacustrine varve deposits overlaid by shallow lake beach deposits.	Phase 2	> 19.0 ± 0.9 ka < 21.7 ± 0.9 ka OSL age: 34.9 ± 2.9 ka
Sediment exposure	-43.702222	-71.411556	RC valley	690	Road-cut section with top-most (below soil) unit (2 m tall exposure) of undisturbed, homogeneous laminated and alternating silt and clay sediment layers (varves).	We interpret these sediments as glaciolacustrine varve deposits.	Phase 2	> 19.0 ± 0.9 ka < 21.7 ± 0.9 ka OSL age: 52.1 ± 4.4 ka
Sediment exposure	-43.704190	-71.411740	RC valley	720	Road-cut section with top-most (below soil) unit (1 m tall exposure) of compacted and laminated sands and clay sediment layers	We interpret these sediments as shallow-water glaciolacustrine deposits.	Phase 2	> 19.0 ± 0.9 ka < 21.7 ± 0.9 ka
Landform	-43.519162	-71.219524	RH valley	~790	Very prominent terrace running at single elevation across the ice-proximal slope of the innermost preserved moraine complex of the RH valley. The terrace is preserved and continuous for over five km	Interpreted as palaeo-shoreline, suggests stabilisation of former proglacial lake at ~790 m in the RH valley	Phase 2: RH and RC connected proglacial lake?	> 19.0 ± 0.9 ka < 21.7 ± 0.9 ka
Landform	-43.514188	-71.305366	RH valley	~790	Very prominent terrace running at single elevation across the southern slopes of the RH valley. The terrace is preserved and continuous for over eight km	Interpreted as palaeo-shoreline, suggests stabilisation of former proglacial lake at ~790 m in the RH valley	Phase 2: RH and RC connected proglacial lake?	> 19.0 ± 0.9 ka < 21.7 ± 0.9 ka

Landform / deposit	-43.679770	-71.428771	RC valley	~740 - 690	Fan shaped, 1.1 km2 platform prograding eastward (average slope: 3°) from the mouth of the Río Poncho Moro western tributary and towards the RC valley centre. The plain deposit displays well-preserved surface braided channels visible from imagery and is located on the southern side of the modern tributary river. The plain is raised ~230 m above the modern RC valley floor and its lower, eastern margin matches the phase three proglacial lake elevation of ~680 m.	We interpret this fan-shaped platform as a "raised delta" formed by fluvial depostion related to the Río Poncho Moro tributary drainage into the former ~680 m proglacial lake residing in the RC trough.	Phase 3: RC, RP and RF connected proglacial lake	> 16.3 ± 0.3 ka < 19.0 ± 0.9 ka
Landform	-43.572829	-71.412454	RC valley	~680	The most prominent terrace feature observed at the field site. The well-preserved, easily discernable terrace is nested at the single elevation of ~680 m on the eastern slope of the RC valley trough, and runs along the valley side discontinuously for ~15 km. Cross-platform DEM elevation profiles reveal an average excavation height of ~6 m.	Interpreted as palaeo-shoreline, suggests stabilisation of former proglacial lake at ~680 m and causing significant wave erosion and platform notching on its former, wind-exposed eastern shore	Phase 3: RC, RP and RF connected proglacial lake	> 16.3 ± 0.3 ka < 19.0 ± 0.9 ka
Landform / deposit	-43.653278	-71.437611	RC valley	~685	Terrace feature runing along the western slope of the RC valley at the maximum elevation of proglacial lake phase three (~680 m). Less prominent than the eastern palaeo-shoreline, this platform was observed on the field at one particular location. The platform is there characterized by a low relief (1-2 m), gently curving ridge with sand- and gravel-sized surface sediments resembling a beach deposit.	Interpreted as palaeo-shoreline, indicating stabilisation of former proglacial lake at ~680 m and causing beach deposition on its former western shore	Phase 3: RC, RP and RF connected proglacial lake	> 16.3 ± 0.3 ka < 19.0 ± 0.9 ka
Sediment exposure	-43.525710	-71.510960	RC valley	393	Road-cut section with top-most (below soil) unit of homogeneous laminated and alternating silt and clay sediment layers (varves).	We interpret these sediments as glaciolacustrine varve deposits.	Phase 3: RC, RP and RF connected proglacial lake	> 16.3 ± 0.3 ka < 19.0 ± 0.9 ka
Sediment exposure	-43.697306	-71.406222	RC valley	544	Quarried section with top-most (below soil) unit (3.5 m of exposure) of homogeneous laminated and alternating silt and clay sediment layers (varves).	We interpret these sediments as glaciolacustrine varve deposits.	Phase 3: RC, RP and RF connected proglacial lake	> 16.3 ± 0.3 ka < 19.0 ± 0.9 ka OSL age: 65.4 ± 7.1 ka
Sediment exposure	-43.534590	-71.486460	RC valley	414	Quarried section with top-most (below soil) 1.7 m thick unit of matrix-supported silt and clay sediments with occasional alternating laminations (varves). The unit also features some embedded larger sub-angular and unsorted gravel, cobbles and boulders of varied lithologies.	We interpret these sediments as glaciolacustrine varve deposits interspersed with ice-rafted debris	Phase 3: RC, RP and RF connected proglacial lake	> 16.3 ± 0.3 ka < 19.0 ± 0.9 ka

Landform / deposit	-43.687121	-71.704755	Río Tigre valley	~710 - 690	Fan-shaped, flat outwash plain with evidence of glaciofluvial deposition (sands and gravel with large polished rounded cobbles, well sorted sediments) located at the mouth of the Río Tigre tributary valley, to the south of the RP valley, and raised 50 m above the modern river elevation. The plain elevation is approximately 10-15 m above the reconstructed maximum elevation of proglacial lake phase three. The plain's northern margin leads to steep, heavily incised slopes displaying a grey/white coloration on imagery suggestive of softer, perhaps glaciolacustrine sediments.	Interpreted as a raised outwash surface/raised delta deposited by glacial meltwater from the Río Tigre flowing northward towards the RP valley during residence of the ~680 m proglacial lake.	Phase 3: RC, RP and RF connected proglacial lake	> 16.3 ± 0.3 ka < 19.0 ± 0.9 ka
Landform	-43.333880	-71.488080	RF valley	~680 - 700	Two raised terraces notched on northwestern slope of RF valley.	Interpreted as palaeo-shorelines, suggests stabilisation of former proglacial lake at ~700-680 m in the narrow RF valley.	Phase 3: RC, RP and RF connected proglacial lake	> 16.3 ± 0.3 ka < 19.0 ± 0.9 ka
Landform	-43.353210	-71.503900	RF valley	~690 - 700	Prominent, well preserved terrace running across the southeastern slope of the RF valley at single elevation for approximately 1 km. Approximate feature elevation was measured using a Laser Range Finder.	Interpreted as palaeo-shoreline, suggests stabilisation of former proglacial lake at ~700-680 m in the narrow RF valley.	Phase 3: RC, RP and RF connected proglacial lake	> 16.3 ± 0.3 ka < 19.0 ± 0.9 ka
Landform / deposit	-43.326520	-71.479690	RF valley	~680 - 700	Two prominent, well preserved, fan-shaped terraces prograding from the mouth of a southern tributary channel of the Río Frío (name unknown) and towards the RF valley. The two terraces are raised 15-20 m above the modern tributary.	We interpret these fan-shaped terraces as "raised deltas" formed by fluvial depostion related to a southern tributary of the RF while draining into the former ~680 m proglacial lake residing in the narrow and shallow RF trough.	Phase 3: RC, RP and RF connected proglacial lake	> 16.3 ± 0.3 ka < 19.0 ± 0.9 ka
Landform	-43.369300	-71.512290	RF valley	683	Prominent, well preserved terrace running across the southeastern slope of the RF valley at single elevation. Lanform proximity to road enabled platform elevation GPS measurement. Landform displays a well-preserved convex lower break-in slope and is raised above modern RF valley floor at this location by ~8 m.	Interpreted as palaeo-shoreline, indicating stabilization of former proglacial lake at ~700-680 m in the narrow RF valley.	Phase 3: RC, RP and RF connected proglacial lake	> 16.3 ± 0.3 ka < 19.0 ± 0.9 ka
Sediment exposure	-43.315990	-71.458250	RF valley	683	Road-cut section with top-most (below soil) unit of homogeneous clay with occasional evidence of lamination.	We interpret these sediments as lacustrine clay deposits suggesting a former lake system in the narrow RF valley	Phase 3: RC, RP and RF connected proglacial lake	> 16.3 ± 0.3 ka < 19.0 ± 0.9 ka
Sediment exposure	-43.52413	-71.57738	RP valley	337	Road-cut section with top-most (below soil) unit of undisturbed, homogeneous laminated and alternating silt and clay sediment layers (varves).	We interpret these sediments as glaciolacustrine varve deposits.	Phase 3: RC, RP and RF connected proglacial lake	> 16.3 ± 0.3 ka < 19.0 ± 0.9 ka

Sediment exposure	-43.531810	-71.571400	RP valley	371	Road-cut section with top-most (below soil) unit of undisturbed, homogeneous laminated and alternating silt and clay sediment layers (varves).	We interpret these sediments as glaciolacustrine varve deposits.	Phase 3: RC, RP and RF connected proglacial lake	> 16.3 ± 0.3 ka < 19.0 ± 0.9 ka
Sediment exposure	-43.53614	-71.61917	RP valley	436	Road-cut section with top-most (below soil) unit of undisturbed, homogeneous laminated clay sediment layers.	We interpret these sediments as lacustrine clay deposits.	Phase 3: RC, RP and RF connected proglacial lake	> 16.3 ± 0.3 ka < 19.0 ± 0.9 ka
Sediment exposure	-43.56483	-71.73346	RP valley	329	Road-cut section with top-most (below soil) unit of undisturbed, homogeneous laminated clay sediment layers.	We interpret these sediments as lacustrine clay deposits.	Phase 3: RC, RP and RF connected proglacial lake	> 16.3 ± 0.3 ka < 19.0 ± 0.9 ka
Sediment exposure	-43.58182	-71.70596	RP valley	404	Road-cut section with top-most (below soil) unit of undisturbed, homogeneous laminated and alternating silt and clay sediment layers (varves).	We interpret these sediments as glaciolacustrine varve deposits.	Phase 3: RC, RP and RF connected proglacial lake	> 16.3 ± 0.3 ka < 19.0 ± 0.9 ka
Sediment exposure	-43.59210	-71.70546	RP valley	375	Quarried section with top-most (below soil) unit (3.5 m of exposure) of laminated sand and silt sediment layers and some occasional clay sediment layers. The unit also displays well dispersed, sub-angular, cobble- and boulder-sized embedded clasts of varied lithologies.	We interpret these sediments as glaciolacustrine deposits with some occasional embedded dropstones.	Phase 3: RC, RP and RF connected proglacial lake	> 16.3 ± 0.3 ka < 19.0 ± 0.9 ka

2. OSL dating samples details and lab methodology

Samples for luminescence dating were collected in opaque tubes and prepared for analysis under subdued lighting conditions. To calculate the environmental dose-rate throughout burial for each sample, U, Th and K concentrations were measured for ca. 80 g of the bulk sediment sample using high-resolution gamma spectrometry. Water contents of 5 ± 2 % were estimated considering the field and saturated water contents, and the environmental history for each sample. Cosmic dose-rates were calculated after Prescott and Hutton (1994). Environmental dose-rates determined for all samples are shown in SM Table 2.

To determine equivalent doses (D_e), grains of K-feldspar were used to determine equivalent doses (D_e). Samples were first treated with a 10 % v/v dilution of 37 % HCl and with 20 % v/v of H_2O_2 to remove carbonates and organics, respectively. Dry sieving then isolated the grainsize used for analysis, which was then subject to density separation using sodium polytungstate (< 2.58 g cm^{-3} K-feldspar dominated) and not etched using hydrofluoric acid. Finally, grains of K-feldspar were mounted on a 9.8 mm diameter aluminium single-grain disc for analysis, which contained a 10 by 10 grid of 200 μm (150 - 180 μm grainsize) or 300 μm (180 – 250 μm grainsize) diameter holes to ensure each hole contained only one grain.

All luminescence measurements were performed using a Risø TL/OSL DA-15 automated single-grain system equipped with a $^{90}Sr/^{90}Y$ beta source (Bøtter-Jensen et al. 2003) fitted with a blue filter pack (BG39, Coring 7-59) in front of the photomultiplier tube. Single aliquot regenerative dose (SAR) protocols (Murray and Wintle, 2000) were used for the post-IR IRSL analyses performed at 225 °C (Thomsen et al. 2008), termed the $pIRIR_{225}$ signal. A preheat temperature of 250 °C for 60 s was used prior to stimulations of 2 s using the infra-red laser at 225 °C. The IRSL signal measured performed at 50 °C prior to the $pIRIR^{225}$ measurement and the elevated temperature bleach of 330 °C for 200 s at the end of each L_x/T_x cycle were performed using the IR LEDs. The location of the single-grain discs was performed at room temperature, rather than elevated temperatures to prevent thermal annealing of the IRSL signal (after Smedley and Duller, 2013). The first 0.3 s and final 0.6 s of stimulation were summed to calculate the initial and background IRSL signals, respectively. The grains were accepted after applying the following screening criteria and accounting for the associated uncertainties: (1) whether the test dose response was greater than three sigma above the background, (2) whether the test dose uncertainty was less than 10 %, (3) whether the recycling and OSL-IR depletion ratios were within the range of ratios 0.9 to 1.1, and (4) whether recuperation was less than 5 % of the response from the largest regenerative dose.

Grains from sample RC19S03 were used for dose-recovery experiments and successfully recovered a given dose within 10 % using the $pIRIR_{225}$ signal. Fading rates (g-values, Aitken 1985) were determined for three aliquots of each sample and normalised to a t_c of two days (Huntley and Lamothe 2001; Fig. 6). The large uncertainties on the individual g-values measured were derived from the uncertainty in the fit of the data, which is typical of fading measurements for the pIRIR signal (e.g. Smedley et al. 2016). To derive a more reliable estimate of the fading rate, the weighted mean and standard error for all the samples was

calculated for $pIRIR_{225}$ signals (-0.9 ± 0.8 %/decade). Given that the $pIRIR_{225}$ fading rate is low with large uncertainties for each sample (SM Table 2) and in line with previous $pIRIR_{225}$ studies (e.g. Roberts, 2012; Trauerstein *et al*. 2014; Kolb and Fuchs 2018), we did not correct the $pIRIR_{225}$ ages for fading.

D_e values were calculated from all grains passing all the screening criteria. The minimum age model (MAM; Galbraith and Laslett, 1993; Galbraith et al. 1999) was applied to determine an age for the samples as the asymmetrical D_e distributions suggested the samples were partially bleached prior to burial (Fig. 1). The scatter in the D_e distribution arising from intrinsic and extrinsic sources were combined in quadrature to determine σ_b for the MAM (SM Table 2). The overdispersion values arising from intrinsic sources for sample RC19S03 (13 ± 1 %) were derived from the dose-recovery experiments, while the over-dispersion arising from variability in the internal dose-rates of K-feldspar grains for both samples was assumed to be 10 % (after Smedley and Pearce, 2016). Additional over-dispersion (20 %) was incorporated to account for the variability in single-grain D_e distributions caused by external microdosimetry (after Smedley *et al*. 2020). The D_e values were then divided by the environmental dose-rates to determine an age for each sample (SM Table 2).

SM Table 2. Luminescence dating results for samples RC19S01, RC19S02 (180-250 µm) and RC19S03 (150-180 µm) from Río Corcovado. Environmental dose-rates were determined using high-resolution gamma spectrometry. The dose-rates were calculated using the conversion factors of Guerin *et al*. (2011) and alpha (Bell, 1980) and beta (Guerin *et al*. 2012) dose-rate attenuation factors. Water contents (5 ± 5 %) were estimated considering the field water contents, and the environmental history for each sample; these values are expressed as a percentage of the mass of dry sediment. An internal K-content of 10 ± 2 % (Smedley *et al*. 2012) were used to determine the internal dose-rates. An a-value of 0.10 ± 0.02 (Balescu & Lamothe, 1993) was used to calculate the alpha dose-rates. Cosmic dose-rates were determined after Prescott & Hutton (1994). Dose-rates were calculated using the Dose Rate and Age Calculator (DRAC; Durcan *et al*. 2015). The *g*-values (%/decade) were measured using the pIRIR225 signal for three aliquots of K-feldspar for each sample, normalised to 2 days and are presented as weighted means and standard errors. The number of grains that were used to determine a *De* value (n) are shown as a proportion of the total grains measured (N). The MAM was used to determine the *De* for age calculating, applying a σb value of 0.25 for all samples.

Sample	U (ppm)	Th (ppm)	K (%)	Internal dose-rate (Gy/ka)	External alpha dose-rate (Gy/ka)	External beta dose-rate (Gy/ka)	External gamma dose-rate (Gy/ka)	Cosmic dose-rate (Gy/ka)	Total dose-rate (Gy/ka)	*g*-value (%/dec.)	n/N	OD (%)	D_e (Gy)	Age (ka)
RC19S01	1.98±0.22	8.25±0.22	1.09±0.22	0.72±0.16	0.12±0.02	1.16±0.16	0.84±0.06	0.27±0.03	3.11±0.24	1.5±4.8	141/4400	53	203.3±15.8	65.4±7.1
RC19S02	2.24±0.25	8.53±0.24	1.20±0.24	0.72±0.16	0.13±0.03	1.28±0.17	0.91±0.07	0.29±0.03	3.31±0.25	0.5±1.5	523/1900	46	172.7±6.4	52.1±4.4
RC19S03	1.69±0.19	6.46±0.25	1.54±0.26	0.56±0.10	0.13±0.02	1.44±0.19	0.83±0.07	0.23±0.02	3.18±0.23	-1.5±0.9	569/2100	47	111.1±4.8	34.9±2.9

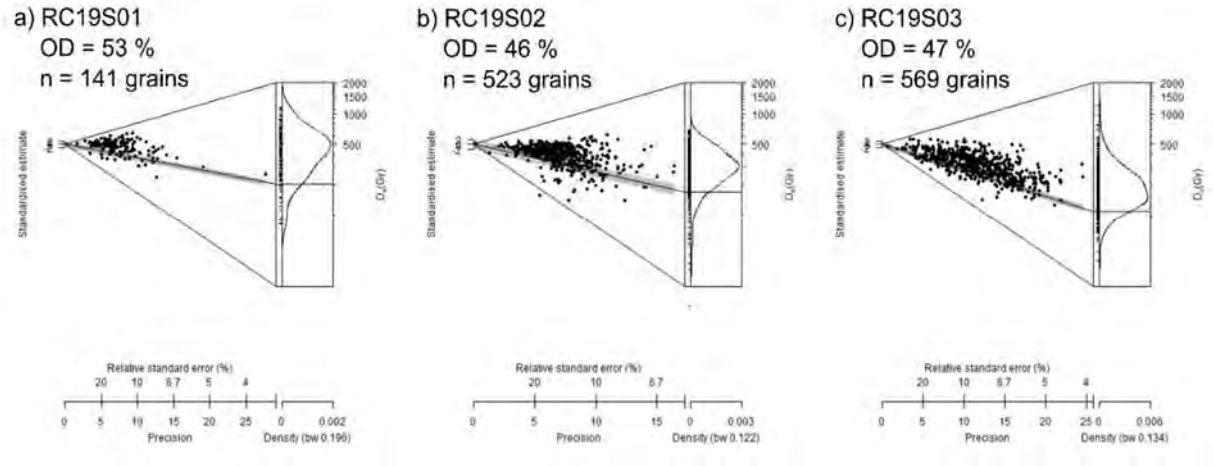

SM Figure. 1. Abanico plots of the D_e values determined for OSL dating, where the grey shading shows the MAM D_e for each distribution.

3. ^{10}Be TCN dating wet chemistry lab methodology

The 125-250 μm and 250-500 μm grain fractions were cleaned and oven-dried to remove non-mineralic grains, prior to being magnetically separated. Non-magnetic fractions were recovered. To remove feldspar and mica minerals, the samples were treated with eucalyptus oil and a carbonated surfactant solution of water and dodecylamine to enable froth floatation (Herber, 1969). Non-floating quartz grains were recovered while floating minerals were stored. The samples were then etched a minimum of three times (24 h each) in 1000 ml of pure water, 40% *HF* and 68% HNO_3 (150:2:1) to isolate the quartz grain cores, thus removing meteoric ^{10}Be. An aliquot of the final quartz sample was dissolved and its purity tested for *Al*; *Be*; *Fe*; *Ca* and *Ti* by ICP-OES. Samples containing *Al* concentration higher than 300 ppm were re-etched. The samples were dissolved in 40% *HF* and each sample and processed blank (n =3) were spiked with between 0.23 and 0.25 mg of ^{9}Be, using an in-house carrier solution obtained from phenakite. After dissolution, the *HF* was evaporated and replaced by *HCl*. The solutions were first passed through anion exchange chromatography columns to remove *Fe*. The *Fe*-free fractions were then evaporated and the *HCl* was replaced by dilute H_2SO_4. The sulphate solutions were then passed through cation exchange chromatography columns to remove *Ti* and *B*, and to isolate *Be* and *Al* fractions, eluted using *HCl* solutions. The *Be* fractions were precipitated as hydroxides and oxidised at ~900 °C. Resulting *BeO* samples were mixed with *Nb* (1:6) and pressed into copper cathodes for AMS measurements. $^{10}Be/^{9}Be$ ratios were determined with a 5MV Tandem Pelletron (NEC Model 15SDH-2). All $^{10}Be/^{9}Be$ ratios were normalised to NIST SRM4325 with a nominal $^{10}Be/^{9}Be$ ratio of $2.79 .10^{-11}$ (Nishiizumi *et al*., 2007), corresponding to a ^{10}Be half-life of 1.36 Ma. Processed blank corrections ranged between 1.4% and 4.5% of the sample $^{10}Be/^{9}Be$ ratios.

4. Vertical plot of published LGM TCN exposure ages from glacial deposits in Patagonia

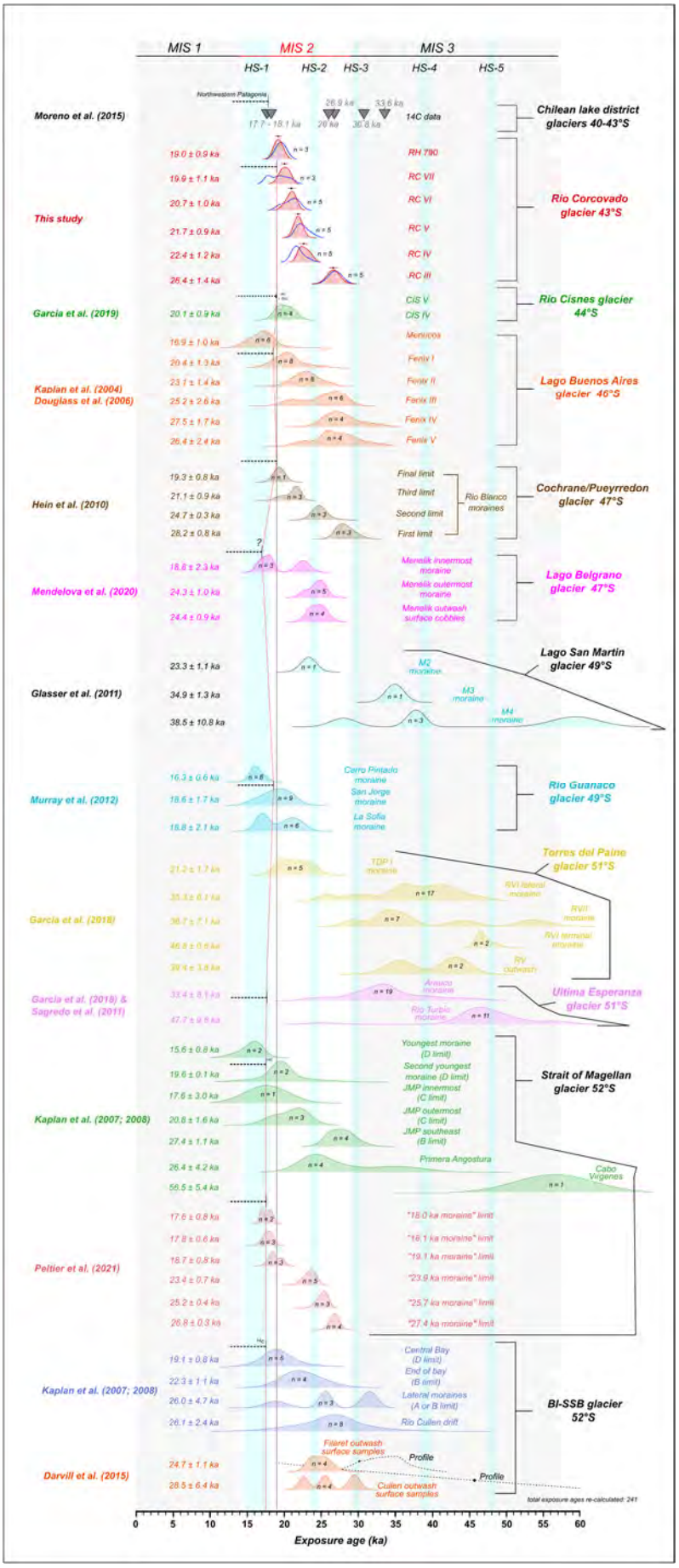

SM Figure 2. Vertical plot of published exposure ages dating local LGM advances of the PIS over the last 60 ka, from north to south, including the RC III – RC VII record (this study). MIS intervals are illustrated by light grey bars (from Lisiecki & Raymo, 2005) while the Heinrich Stadial (HS) 1-5 events are designated by a light blue bars (from Hemming, 2004). Apart from the Chilean Lake District record (^{14}C dates), ^{10}*Be* exposure ages (n = 241) are displayed as cumulative kernel density plots (adapted from iceTEA tools for exposure dating plots; Jones *et al*., 2019) using 1σ ranges and internal analytical uncertainties from individual ages. All exposure ages (n=241) have been re-calculated using the Patagonian production rate (Kaplan *et al*., 2011) obtained from the ICE-D online database (http://calibration.ice-d.org/) and the LSDn-time-dependent scaling scheme of Lifton *et al*. (2014). All ages assume no surface erosion and no correction for shielding by snow, soil and/or vegetation. Outliers identified as such by original publications were manually removed. Dashed horizontal black bars with vertical bars on right-hand extremities indicate the possible onset of local deglaciation proposed by the original publications, after taking into account landform-age re-calculation. Note that the number of samples per landform varies significantly between study-sites / publications. Subsequently, not all records displayed here present comparable levels of dating robustness.

5. ^{10}Be TCN dating kernel density plots per landform

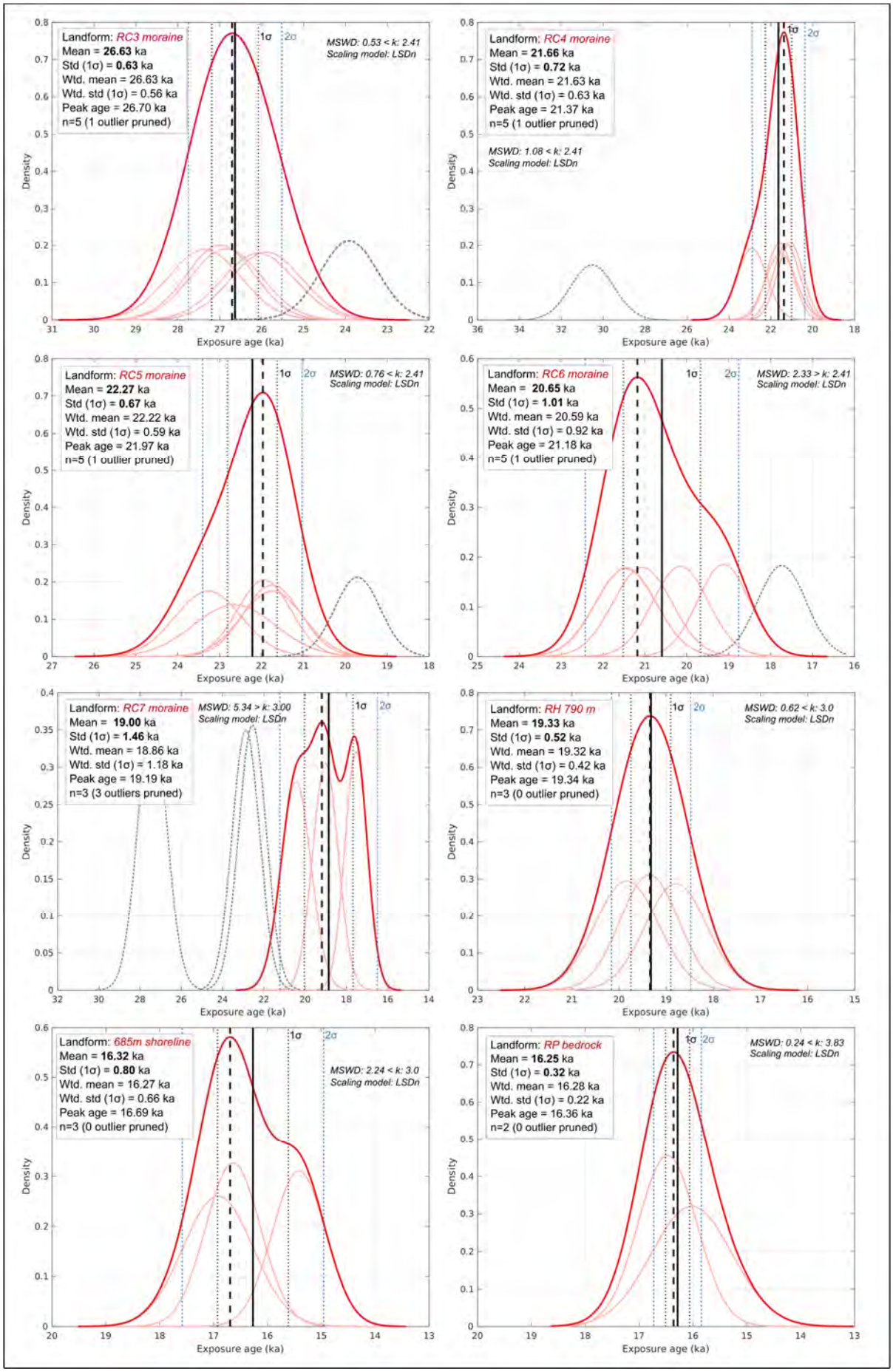

SM Figure 3. Kernel density plots, adapted from plots produced using the IceTEA tools for exposure dating (Jones *et al*., 2019; http://ice-tea.org/en/) and TCN dating summary statistics for the RC III-VII, RH_{790}, RC_{680} and RPbed dated landforms. Thick red curve represent the summed probability distribution for the age population, excluding outliers, while thin red curves depict Gaussian curves for individual samples. Outliers are denoted by grey dashed curves. Vertical black lines denote the arithmetic mean, while thin black and blue vertical dashed lines denote the 1 σ and 2 σ confidence intervals of the mean, respectively. Thick black and dashed vertical line highlights the peak age associated with the summed probability distribution. Std: standard deviation, Wtd. mean: uncertainty-weighted mean, Wtd. std: uncertainty-weighted standard deviation.

6. Cosmo-Ages Sequence Calculator (CASC)

This programme was employed to produce age probability distributions for each dated landform using a Bayesian statistical approach that takes into account the relative stratigraphic order of events.

Programmer: Dr. Ángel Rodés (Scottish Universities Environmental Research Centre, Scottish Enterprise Technology Park, East Kilbride, G75 OQF, Glasgow, Scotland, United Kingdom of Great Britain and Northern Ireland)

Coding language: MATLAB

Code URL: https://github.com/angelrodes/CASC

Input file: data.csv

Input data: Column A (Sample) = Sample ID
Column B (Age) = Sample exposure age (ka)
Column C (Uncert.) = Internal analytical uncertainty (ka)
Column D (Moraine) = Landform name
Column E (Sequence) = Stratigraphic order of sequences: with "1" being the oldest event, "2" the second oldest etc… (see example below).

Sample	Age	Uncert.	Moraine	Sequence
19RCS21	26.075	0.877	RC3	1
19RCS23	XXXXX	YYYY	RC3	1
19RCS25	XXXXX	YYYY	RC3	1
19RCS27	XXXXX	YYYY	RC3	1
19RCS28	XXXXX	YYYY	RC3	1
19RCS15	XXXXX	YYYY	RC4	2
19RCS16	XXXXX	YYYY	RC4	2
19RCS17	XXXXX	YYYY	RC4	2
19RCS51	XXXXX	YYYY	RC4	2
19RCS52	XXXXX	YYYY	RC4	2

7. References (supplementary materials-specific, otherwise refer to main text)

Aitken, M. J. (1985). Thermoluminescence dating.

Balescu, S., Lamothe, M., 1993. Thermoluminescence dating of the Holsteinian marine formation of Herzeele, northern France. *Journal of Quaternary Science*, 8(2), 117-124. Doi: https://doi.org/10.1002/jqs.3390080204

Bell, W.T. 1980. Alpha dose attenuation in quartz grains for thermoluminescence dating. Ancient TL, 12, 4 – 8.

Blair, T. C. (2002). Alluvial-fan sedimentation from a glacial-outburst flood, Lone Pine, California, and contrasts with meteorological flood deposits. *Flood and Megaflood Processes and Deposits: Recent and Ancient Examples*, 111-140. Doi: https://doi.org/10.1002/9781444304299.ch8

Blair, T. C., & McPherson, J. G. (2009). Processes and forms of alluvial fans. In Geomorphology of desert environments (pp. 413-467). Springer, Dordrecht. Doi: https://doi.org/10.1007/978-1-4020-5719-9

Bøtter-Jensen, L., Andersen, C.E., Duller, G.A.T., Murray, A.S. (2003). Developments in radiation, stimulation and observation facilities in luminescence measurements. Radiation Measurements, 37(4-5), 535-541. Doi : https://doi.org/10.1016/S1350-4487(03)00020-9

Durcan, J. A., King, G.E., Duller, G.A.T. (2015). DRAC: Dose Rate and Age Calculator for trapped charge dating. *Quaternary Geochronology*, 28, 54 – 61. Doi : https://doi.org/10.1016/j.quageo.2015.03.012

Galbraith, R.F. and Laslett, G.M. (1993). Statistical models for mixed fission track ages. International Journal of Radiation Applications and Instrumentation. Part D. *Nuclear Tracks and Radiation Measurements*, 21, 459-470. Doi : https://doi.org/10.1016/1359-0189(93)90185-C

Galbraith, R.F., Roberts, R. G., Laslett, G.M., Yoshida, H. and Olley, J.M. (1999). Optical dating of single and multiple grains of quartz from Jinmium rock shelter, northern Austrailia: part I, experimental design and statistical models. *Archaeometry*, 41, 339 – 364. Doi : https://doi.org/10.1111/j.1475-4754.1999.tb00987.x

Glasser, N. F., Jansson, K. N., Goodfellow, B. W., De Angelis, H., Rodnight, H., & Rood, D. H. (2011). Cosmogenic nuclide exposure ages for moraines in the Lago San Martin Valley, Argentina. Quaternary Research, 75(3), 636-646. Doi: https://doi.org/10.1016/j.yqres.2010.11.005

Guerin, G., Mercier, N., Adamiec, G. (2011). Dose-rate conversion factors: update. *Ancient TL* 29, 5-8.

Herber, L. J. (1969). Separation of feldspar from quartz by flotation. American Mineralogist: Journal of Earth and Planetary Materials, 54(7-8), 1212-1215.

Huntley, D.J., Lamothe, M. (2001). Ubiquity of anomalous fading in K-feldspars and the measurement and correction for it in optical dating. *Canadian Journal of Earth Sciences*, 38(7), 1093-1106. Doi : https://doi.org/10.1139/e01-013

Kolb, T., Fuchs, M. (2018). Luminescence dating of pre-Eemian (pre-MIS 5e) fluvial terraces in Northern Bavaria (Germany) – Benefits and limitations of applying a pIRIR225-approach. *Geomorphology*, 321, 16-32. Doi : https://doi.org/10.1016/j.geomorph.2018.08.009

Murray, A.S., Thomsen, K.J., Masuda, N., Buylaert, J.P., Jain, M. (2012). Identifying well-bleached quartz using the different bleaching rates of quartz and feldspar luminescence signals. *Radiation Measurements*, 47(9), 688-695. Doi : https://doi.org/10.1016/j.radmeas.2012.05.006

Prescott, J.R., Hutton, J.T., 1994. Cosmic ray and gamma ray dosimetry for TL and ESR. *International Journal of Radiation Applications and Instrumentation. Part D. Nuclear Tracks and Radiation Measurements,* 14(1-2), 223-227. Doi : https://doi.org/10.1016/1359-0189(88)90069-6

Roberts, H.M. (2012). Testing post-IR IRSL protocols for minimising fading in feldspars, using Alaskan loess with independent chronological control. *Radiation Measurements*, 47(9), 716-724. Doi : https://doi.org/10.1016/j.radmeas.2012.03.022

Sagredo, E. A., Moreno, P. I., Villa-Martínez, R., Kaplan, M. R., Kubik, P. W., & Stern, C. R. (2011). Fluctuations of the Última Esperanza ice lobe (52 S), Chilean Patagonia, during the last glacial maximum and termination 1. Geomorphology, 125(1), 92-108. Doi: https://doi.org/10.1016/j.geomorph.2010.09.007

Smedley, R.K., Duller, G.A.T., Pearce, N.J.G., Roberts, H.M. (2012). Determining the K- content of single-grains of feldspar for luminescence dating. *Radiation Measurements*, 47(9), 790-796. Doi : https://doi.org/10.1016/j.radmeas.2012.01.014

Smedley, R.K., Duller, G.A.T. (2013). Optimising the reproducibility of measurements of the post-IR IRSL signal from single-grains of feldspar for dating. *Ancient TL*, 31(2), 49-58. URL : hdl.handle.net/2160/28754

Smedley, R.K., Pearce, N.J. G. (2016). Internal U and Th concentrations of K-feldspar grains: implications for luminescence dating. *Quaternary Geochronology*, 35, 16 – 25.

Smedley, R. K., & Skirrow, G. K. (2020). Luminescence dating in fluvial settings: overcoming the challenge of partial bleaching. In *Palaeohydrology* (pp. 155-168). Springer, Cham.

Thomsen, K.J., Murray, A.S., Jain, M., Bøtter-Jensen, L. (2008). Laboratory fading rates of various luminescence signals from feldspar-rich sediment extracts. *Radiation measurements*, 43(9-10), 1474-1486. Doi : https://doi.org/10.1016/j.radmeas.2008.06.002

Trauerstein, M., Lowick, S.E., Preusser, F., Schlunegger, F. (2014). Small aliquot and single-grain IRSL and post-IR IRSL dating of fluvial and alluvial sediments from the Pativilca valley, Peru. *Quaternary Geochronology*, 22, 163-174. Doi : https://doi.org/10.1016/j.quageo.2013.12.004